PEPTIDE NANOSTRUCTURE TEMPLATED GROWTH OF IRON PHOSPHATE NANOSTRUCTURES FOR ENERGY STORAGE APPLICATIONS

A THESIS SUBMITTED TO
THE GRADUATE SCHOOL OF ENGINEERING AND SCIENCE
OF BILKENT UNIVERSITY
IN PARTIAL FULFILLMENT OF THE REQUIREMENTS FOR
THE DEGREE OF
MASTER OF SCIENCE
IN
MATERIALS SCIENCE AND NANOTECHNOLOGY

By
Hepi Hari Susapto
December, 2015

PEPTIDE NANOSTRUCTURE TEMPLATED GROWTH OF IRON PHOSPHATE NANOSTRUCTURES FOR ENERGY STORAGE APPLICATIONS

By Hepi Hari Susapto

December, 2015

We certify that we have read this thesis and that in our opinion it is fully adequate, in scope and in quality, as a thesis for the degree of Master of Science.

Assoc. Prof. Dr. Mustafa Özgür Güler (Advisor)

Asst. Prof. Dr. Tarık Baytekin

Assoc. Prof. Dr. İlknur Tunç (THK Univ.)

Approved for the Graduate School of Engineering and Science:

Prof. Dr. Levent Onural

Director of the Graduate School

ABSTRACT

PEPTIDE NANOSTRUCTURE TEMPLATED GROWTH OF IRON PHOSPHATE NANOSTRUCTURES FOR ENERGY STORAGE APPLICATIONS

Hepi Hari Susapto

M.S. in Materials Science and Nanotechnology

Advisor: Assoc. Prof. Dr. Mustafa Özgür Güler

December, 2015

The use of primary cells has been replaced with rechargeable batteries due to environmental concerns. Li-ion batteries are examples of the rechargeable batteries that have replaced other types of rechargeable batteries from market due to high capacity, high electrochemical potential, superior energy density, durability, as well as the flexibility in design. Compared to other cathode materials used in Li-ion batteries, the iron oxide ($FePO_4$) is less toxic, environmentally friendly, and less expensive.

Inorganic materials can be fabricated by template-directed mineralization to enable control over size and morphology. One-Dimensional (1-D) nanostructures can be used for template directed mineralization method. The nanostructures are particularly interesting as electrode materials due to their high surface area, large surface-to-volume ratio, and favorable structural stability. They provide fast ion/electron transfer by sufficient contact between the active materials and electrolyte.

In this thesis, 1-D nanostructures of $FePO_4$ materials with high surface area were synthesized to enhance the efficiency of Li-ion batteries. The synthesis of iron phosphate nanostructures was performed by using peptide amphiphile nanostructures. Iron (III) chloride ($FeCl_3$) was used to trigger the self-assembly of the peptide amphiphile molecules forming nanostructures, which can nucleate $FePO_4$ formation. The electrochemical performance of

these nanostructures for Li-ion battery was analyzed. In conclusion, the template directed electrode materials revealed fast ion/electron transfer and sufficient contact between materials and electrolyte. They also exhibited enhanced flexibility leading to higher capacity than the electrode material synthesized without the template.

Keywords: Peptide amphiphile, Self-assembly, Hydrogel, One-dimensional Nanostructure, Nanofiber, Nanobelt, Template-directed materials, Iron phosphate, Lithium-ion batteries

ÖZET

PEPTİT NANOYAPI ŞABLONUYLA ENERJİ DEPOLAMA UYGULAMALARI İÇİN DEMİR FOSFAT NANOYAPILARIN GELİŞTİRİLMESİ

Hepi Hari Susapto

Malzeme Bilimleri ve Nanoteknoloji, Yüksek Lisans

Tez Danışmanı: Doç. Dr. Mustafa Özgür Güler

Aralık, 2015

Şarj edilebilir piller, çevre dostu kullanımları sebebiyle birincil hücrelerin kulanımının yerine geçmişlerdir. Lityum-iyon piller, yüksek elektrokimyasal potansiyelleri, yüksek enerji yoğunluğu, dayanıklılığı ve esnek tasarlanabilirlikleri sayesinde piyasadaki diğer şarj edilebilir bataryaların yerini alan pil örneklerinden birisidir. Diğer katot malzemelere kıyasla, Li-iyon piller kullanılan demir oksit ($FePO_4$) daha az toksik, çevre dostu ve daha ucuzdur.

Anorganik malzeme üretiminin yollarından biri, malzeme boyutu ve yapısı üzerinde kontrol sağlamayı kolaylaştıran, şablon-yönelimli mineralizasyon yöntemi kullanmaktır. Tek boyutlu (1-D) nanoyapıların üretilmesi, kullanınlan şablonun özelliği gözönünde bulundurularak mümkündür. Nanoyapılar özellikle, aktif madde ve elektrolit arasında yeterli teması sağlayarak hızlı iyon/elektron transferini destekleyen geniş yüzey ve hacim oranları ve yapısal kararlılıkları sayesinde ilgi çekmektedirler.

Bu bağlamda, lityum iyon pil verimliliğini artırmak için, geniş yüzey alanına sahip tek boyutlu demir fosfat ($FePO_4$) nanomalzemeler, sentezlenmiştir. Demir fosfat nanoyapılarının sentezi, iki farklı peptit amfifil kullanılarak yapılmıştır. Demir (III) klorür ($FeCl_3$), peptit amfifil moleküllerinin kendiliğinden biraraya gelmesini başlatmak için kullanılmış ve sonrasında kendiliğinden biraraya gelen bu nanoyapı, $FePO_4$'ın nükleasyon bölgesini oluşturmuştur. Beta yaprağı ikincil yapı oluşturan bu peptitler, organik-anorganik çekirdek kabuk (core-

shell) malzemeleri için esas teşkil eden nanoyapıların oluşumunu sağlamaktadır. Kalsinasyon, peptidi uzaklaştırılmak için yapılmıştır. Li-iyon pilleri için kullanılan katot film, tek boyutlu demir fosfat şsblon ile çok-duvarlı karbon nanotüplerinin (MWNT) karışımı ile hazırlanmıştır. Sonuç olarak, bu şablon-yönelimli elektrot malzemesi, hızlı iyon/electron transferi, malzeme ve elektrolit arasında yeterli temas ve geliştirilmiş esnekliğin yardımıyla şablon olmadan üretilen elektrot materyalinden daha yüksek toplam kapasite sunmaktadır.

Anahtar sözcükler: Peptit amfifil, Kendiliğinden düzenlenme, Hidrojel, Tek-boyutlu nanoyapılar, Nanofiber, Nanobelt, Şablon-yönelimli malzemeler, Demir fosfat, Lityum iyon piller.

ACKNOWLEDGEMENT

I would like to express my gratitude to my advisor, Assoc. Prof. Dr. Mustafa Özgür Güler, for his utmost support, patience, motivation, and immense knowledge. His guidance helped me in all the time of research and writing this thesis. I am really fortunate to have worked in his research group.

I acknowledge Dr. Ruslan Garifullin, Dr. Ashif Shaikh, Ulaş Kudu, Dr. Özlem Erol, and Dr. Eda Yılmaz for their team work and hardship to make this research project successful. I would like also to express my special gratitude to Assoc. Prof. Dr. Ayşe Begüm Tekinay for her ideas and advices that help me understand more about research. I want to express my thanks to Assoc. Prof. Dr. İlknur Tunç for letting me work with her. I learned many things from her during our collaboration. I would like to express my thanks to Asst. Prof. Dr. Tarık Baytekin for the insightful discussions. It was a great pleasure to have him in the jury of my thesis.

I would like to express my thanks to Aygül Zengin, Meryem Hatip, Arif Khalily, Gülcihan Gülseren, Melis Şardan, Göksu Çınar, Alper Devrim Özkan, Ahmet Emin Topal, Gülistan Tansık, and other members of the Biomimetic Materials and Nanobiotechnology groups for sharing knowledge and giving excellent support. This thesis could not be written without the excellent support I have had from them.

I would acknowledge TÜBİTAK (Grant No. 113M900) and the 2215-TÜBİTAK Graduate Scholarship for International Students for the research funds.

I would like to express my heart-felt gratitude to my beloved family: my father, my mother, and my brothers. None of this would have been possible without the love and patience of my family. Their endless support and pray for me has strengthened me the most.

I am very grateful to all people I have met along the way and have contributed to the development of my research. In particular, I would like to show my gratitude to Nenden Octavarulia Shanty for her advice and assistance.

Finally, I would like to express my thanks to Amdya Mashfufah Hisyam for her unflagging love and unconditional support throughout my life and my studies.

TABLE OF CONTENTS

TABLE OF FIGURES

LIST OF ABBREVIATIONS

$LiFePO_4$	: Lithium iron phosphate
$FePO_4$	: Iron phosphate
1-D	: One-dimensional
3-D	: Three-dimensional
MWCT	: Multi-walled carbon nanotube
PA	: Peptide amphiphile
E-PA	: Lauryl-VVAGE peptide amphiphile
Phos-PA	: Phosphonoacetic acid peptide amphiphile
SPSS	: Solid phase peptide synthesis
TFA	: Trifluoroacetic acid
Fmoc	: 9-Fluorenylmethoxycarbonyl
tBoc	: tert-Butoxycarbonyl
HBTU	: 2-(1H-Benzotriazol-1-yl)-1,1,3,3-tetramethyluronium hexafluorophosphate
DIEA	: N, N-Diisopropylethylamine
DMF	: Dimethylformamide
DCM	: Dichloromethane
$FeCl_3$	: Iron (III) chloride
LiH_2PO_4	: Lithium phosphate monobasic
NaH_2PO_4	: Sodium phosphate monobasic
LiTFSI	: Lithium bis(trifluoromethanesulfonyl) imide
EC	: Ethylene carbonate
DMC	: Dimethyl carbonate
LC-MS	: Liquid chromatography-mass spectrometry
Prep-HPLC	: Preparative high performance liquid chromatography
CPD	: Critical point dryer
CD	: Circular dichroism
E-SEM	: Environmental scanning electron microscopy
TEM	: Transmission electron microscopy

STEM	: Scanning transmission electron microscopy
XPS	: X-ray photoelectron spectroscopy
XRD	: X-ray diffractometer
FT-IR	: Fourier transform infrared spectroscopy
TGA	: Thermal gravimetric analysis
ICP-MS	: Inductively coupled plasma – mass spectrometry

CHAPTER 1

INTRODUCTION

1. INTRODUCTION

Lithium, which is known as the lightest metal can deliver high energy density per electron. It was first used as negative electrode material of primary lithium ion (Li-ion) cells in the 1970s [1]. The research on rechargeable Li-ion batteries itself, was started after the development of a series of intercalation compounds that can react reversibly with lithium [2]. These Li-ion batteries are preferred to other secondary batteries, such as lead-acid or nickel-cadmium batteries, due to long cycle life, high specific energy, and no memory effect leading to the most used of rechargeable power source in the wide variety of electronic devices [3].

1.1. Rechargeable Lithium-Ion Batteries

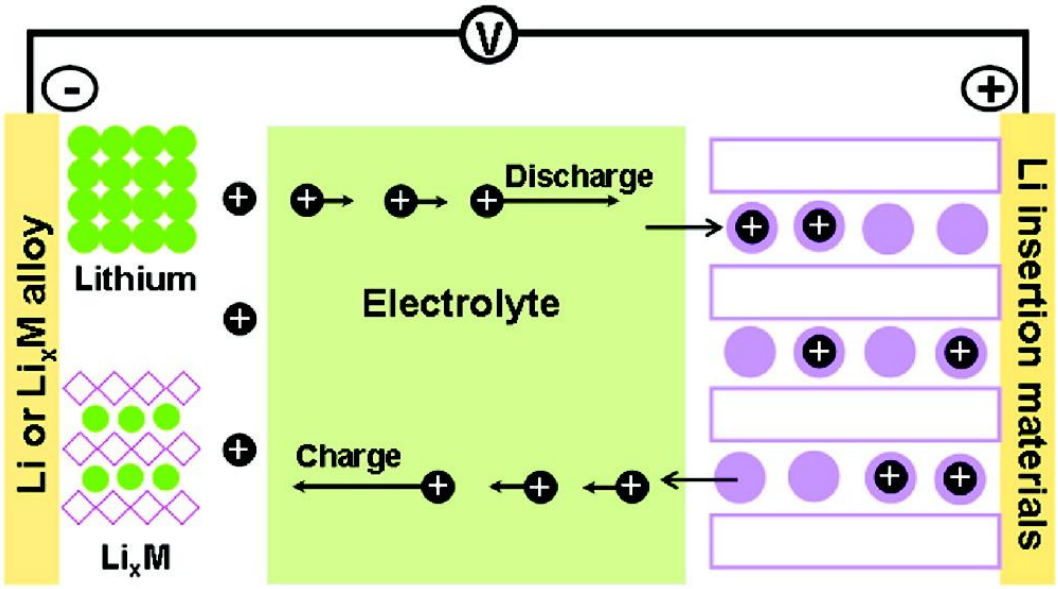

Figure 1.1. A schematic illustration of rechargeable Li-ion batteries (Reproduced with permission from Reference [4]. Copyright 2008 American Chemical Society).

Discharge and charge in Li-ion batteries are two basic principles that exhibit the process of conversing and storing of electrochemical energy (Figure 1.1). For research purposes, the anode of Li-ion batteries usually consists of lithium-insertion/conversion compounds or lithium metal, while the cathode consists of Li^+ host material that has more positive redox potential [5]. During discharging process,

the Li^+ cations leave the anode through the electrolyte to intercalate the cathode providing the electrons to flow from anode to cathode. When the cell is charged, the electrons are provided to the anode allowing the Li^+ cations to deintercalate in reverse from the cathode to anode. These conversion and storage of electrochemical energy depend on the diffusion of Li-ion between the cathode and the anode during the cycling process. Therefore, electrode materials that can accommodate a large amount of lithium and fast ionic/electronic transfer in the cell are required to obtain high specific capacity of the batteries [4].

Some works have been done to design new active materials with high reversible capacity, structural flexibility and stability, fast Li^+ diffusion at high rate, low cost, less toxic, and environmentally friendly [3]. For example, lithium iron phosphate with olivine phases has been intensively studied as the cathode material due to high stability and conductivity that would be promising for rechargeable batteries [6, 7].

1.1.1. $LiFePO_4$

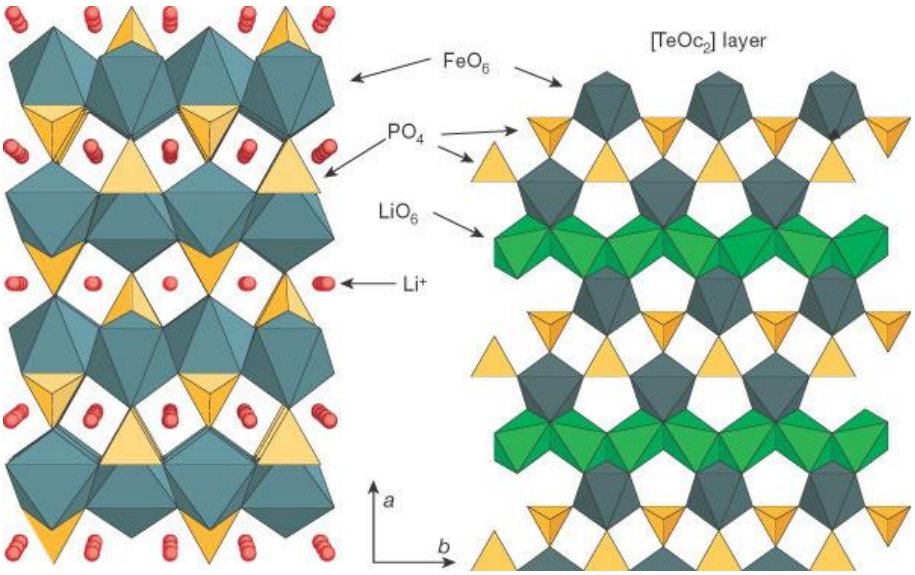

Figure 1.2. The crystal structure of olivine phases $LiFePO_4$ in projection along [001] (Reprinted with permission from Macmillan Publisher Ltd: [2], copyright 2008).

The high capacity (170 $mAhg^{-1}$), material abundance of iron, stability at high temperature, and high rate of charging are the advantages of using lithium iron phosphate ($LiFePO_4$) with olivine structure as the cathode material for Li-ion battery [8]. The olivine structure enables the lithium to be extracted and inserted into $LiFePO_4$ at low current density [9]. The high-rate charging of lithium iron phosphate comes from the large margin of voltage between working potential (E_w) of 3.45 V and charging voltage of 4.3 V. However, due to this low working potential, $LiFePO_4$ exhibits low energy density (QE_w) during discharge process. In addition, pure $LiFePO_4$ behaves as insulator due to low ionic and electronic conductivities of lithium iron phosphate around 10^{-5} and 10^{-9} Scm^{-1}, respectively. These low conductivities prevent the lithium iron phosphate to reach the theoretical capacity even at low discharge rates leading to poor rate capability [10, 11]. To overcome these problems, decreasing the particle size [12, 13], coating or making composites with conductive phases [14, 15], and doping with cationic or anionic ions can be employed [7].

1.1.2. $FePO_4$

The intercalation and deintercalation mechanisms of $LiFePO_4$ can be illustrated as the two-phase behavior of the $LiFePO_4/FePO_4$ system. By giving out 1 equivalence of lithium ion, lithium iron phosphate transform its phase into iron phosphate phase in which the structure is still same [16]. Thus, $FePO_4$ is also available to be used as the cathode materials. There are also some advantages of using iron phosphate, such as inexpensive material, simple to be synthesized, environmentally friendly, and higher theoretical capacity (178 mA h g^{-1}) [17]. However, the problems of $LiFePO_4$ are still encountered also in $FePO_4$, such as low electronic and ionic conductivities [18]. Amorphous structure of $FePO_4$ is preferred to be used as cathode of Li-ion batteries than crystalline $FePO_4$ that depends on the guest ion intercalate/deintercalate during charge/discharge process. The amorphous $FePO_4$ maintains short-range structural ordering, improved kinetics, high surface area, and free volume which accommodate lattice distortions without producing macroscopic phase transition. These benefits increase specific capacities and provide stable electrochemical cycling over a wide potential window [19, 20].

1.2. Modification to enhance cell performances

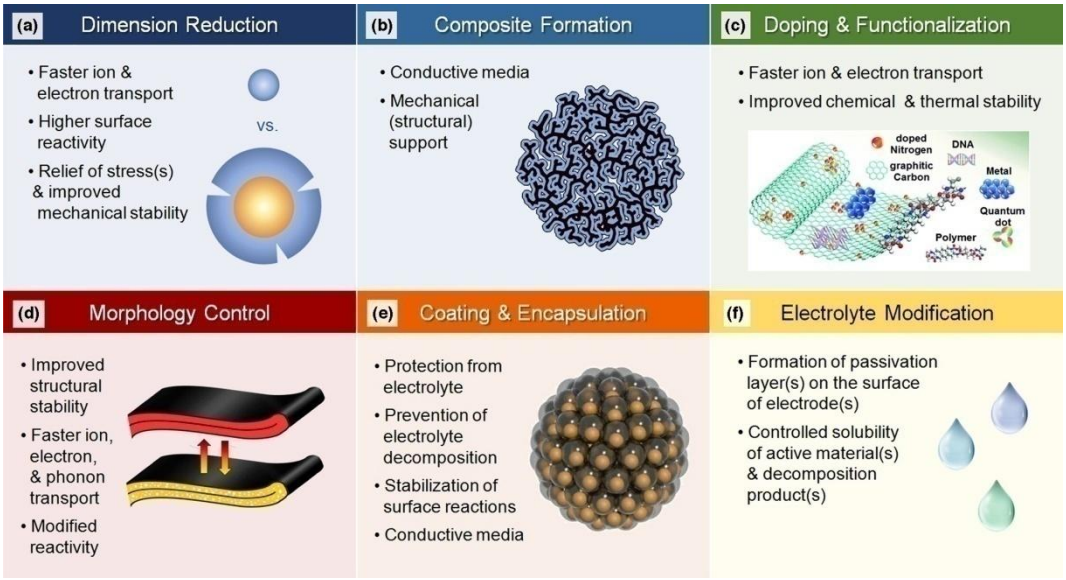

Figure 1.3. The modification methods to enhance the cell performances of Li-ion battery (Reprinted from [21] with permission from Elsevier).

During the charging process of $LiFePO_4$, a Li-ion diffuses out of the cathode (ionic conductivity) allowing the Fe^{2+} ion to be oxidized into Fe^{3+} (electronic conductivity) [22]. These ionic and electronic conductivities affect the capacity and cell life of the cathode material, therefore it is important to enhance these values in order to improve the battery performances [10, 23]. Due to low ionic and electronic conductivities in $LiFePO_4$ and $FePO_4$, some methods have been developed in order to enhance these values (Figure 1.3).

Electrodes based on nanomaterials grant some advantages leading to the improvement of the battery performances [24, 25]. As the size of the electrode decreases to nanoscale, the length of the electronic and ionic transports becomes shorter leading to the enhancement in rate capabilities based on fast kinetics [13, 26]. Therefore, the charging time could be reduced allowing the batteries to be used longer even at higher power situations that make it beneficial for electric vehicles [8]. The electrode nanomaterials can also effectively accommodate the strain that come from the volume changes during lithium intercalation/deintercalation extending the cycle life of cells [27, 28].

Although the higher surface to volume ratio of nanomaterials provides more reaction sites for lithium intercalation/deintercalation, undesirable electrode/electrolyte reactions can be observed on the surface reducing the benefits of using electrode nanomaterials. A coating layer which is permeable to the lithium ion only can be adjusted on the surface to reduce the unwanted side reactions [29]. In addition, the nanomaterials also have disadvantage over the lower volumetric energy density due to the lower particle packing density [30]. To solve this problem, a composite electrode consisting of both nanotubes and nanoparticles can be prepared to obtain higher particle packing density [8].

By introducing the conductive carbon materials to electrode materials either by coating or preparing composite material, the electronic conductivity can be increased significantly from 10^{-8} to 10^{-5} Scm^{-1} (Figure 1.4). Compared to carbon black which has been popularly being used as conductive agents in Li-ion batteries, carbon nanotube attributes its tubular shape and smaller surface area with higher electronic conductivity that has been applied in field emission and energy storage.

One-dimensional (1-D) nanostructures (nanowires, nanorods, nanotubes, and nanobelts) have become important for applications of energy conversion and storage such as in solar cells and Li-ion batteries [8]. They have larger surface area compared to their equivalent three dimensional structures [31]. Compared to a rod structure also, 1-D nanostructure containing tubular or hollow has more effective electrolyte contact area due to double-sided electrolyte diffusion leading to a better performance [8].

In Li-ion batteries, by adding multi-walled carbon nanotubes (MWCTs) to $LiFePO_4$, the electronic conductivity can be improved [32]. MWCTs provide more facile electronic transport channels and also thermal and mechanical stabilities [33]. They construct strong webs with $LiFePO_4$ particles making the composite electrode to be stable during the charge and discharge processes (Figure 1.5) [34].

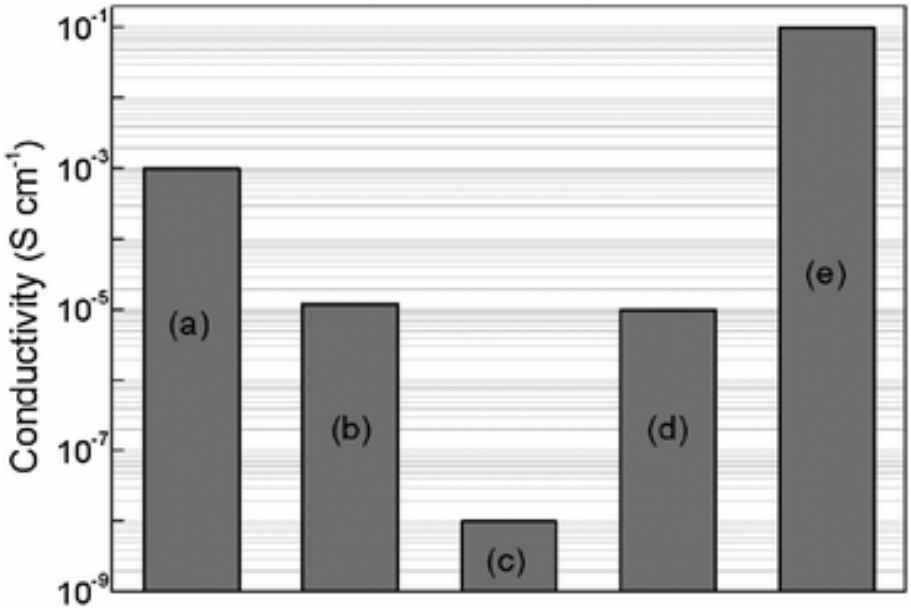

Figure 1.4. Electronic conductivities of cathode materials of Li-ion batteries. (a) $LiCoO_2$, (b) $LiMnO_4$, (c) $LiFePO_4$, (d) nanocomposite of $LiFePO_4$ and carbon black, and (e) nanocomposite of $LiFePO_4$ and MWCTs (Reproduced from [8] with permission of The Royal Society of Chemistry).

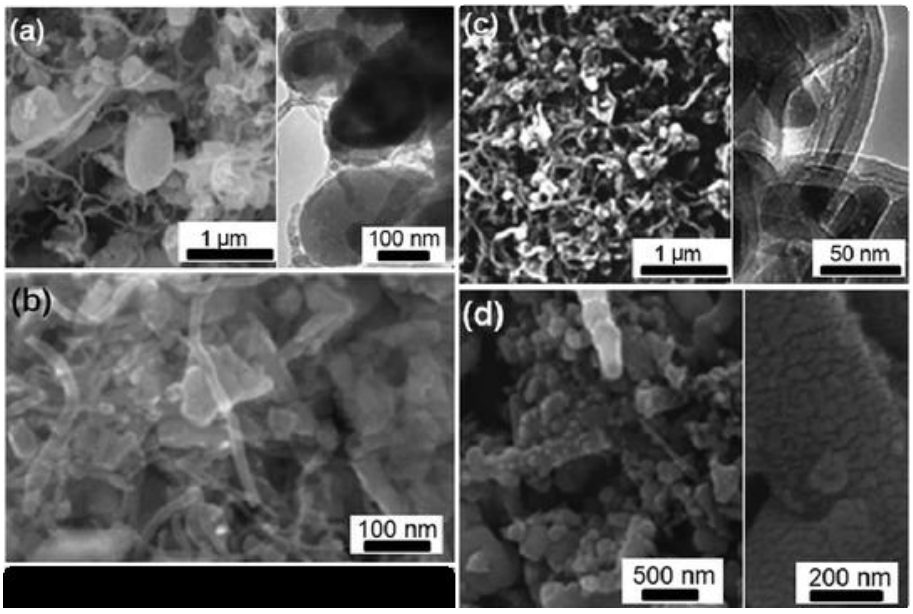

Figure 1.5. Nanocomposites of $LiFePO_4$. (a-c) With MWCTs, and (d) coating with carbon nanofibers (Adapted from Reference [8] with permission of The Royal Society of Chemistry).

1.3. Template-Directed Growth of Materials

Synthesizing a material with controlled structure and desired function can be achieved by using a template [35-38]. For example, the electrode nanostructure materials with different morphologies (1-D nanostructures, 2-D films, and 3D interconnected porous architectures) can be synthesized by employing the template precursors. The template directed materials usually have small crystalline size, high surface area, large surface-to-volume ratio, and favorable structural stability that are favorable for electrode materials by providing fast ion/electron transfer, sufficient contact between active materials and electrolyte, and enhanced flexibility [4]. At the end, an improvement in electrode performances such as higher overall capacity, better high-rate capability, and longer cycling life can be expected from template-directed synthesized electrode materials.

The templates used in this synthesis can be divided into two types regarding the flexibility, which are hard template and soft template (Figure 1.6). The synthesis of template-directed materials contains three consecutive steps, which are: (1) impregnation or incorporation of precursors into the templates; (2) formation of solid species through reaction, nucleation, and growth; and (3) template removal to obtain the product [4].

1.3.1. Hard Templates

The structure of templated-directed material from hard templates is strongly affected by the connectivity of the pores or channels. For templates with isolated pores, such as AAO membranes and MCM-41 silica, the products are formed inside the isolated pores by filling the void space in templates [38]. After removing the template scaffold, aligned structures of 1-D nanotubes or nanowires are collected (Figure 1.6.a). On the other hand, the templates with continuous pores such as carbon or silica gels form product with interconnected 3D pores (Figure 1.6.b) [39]. Hard templates with isolated pores, especially AAO membranes are the most widely us hard templates due to facile preparation and controllable pore size [40, 41].

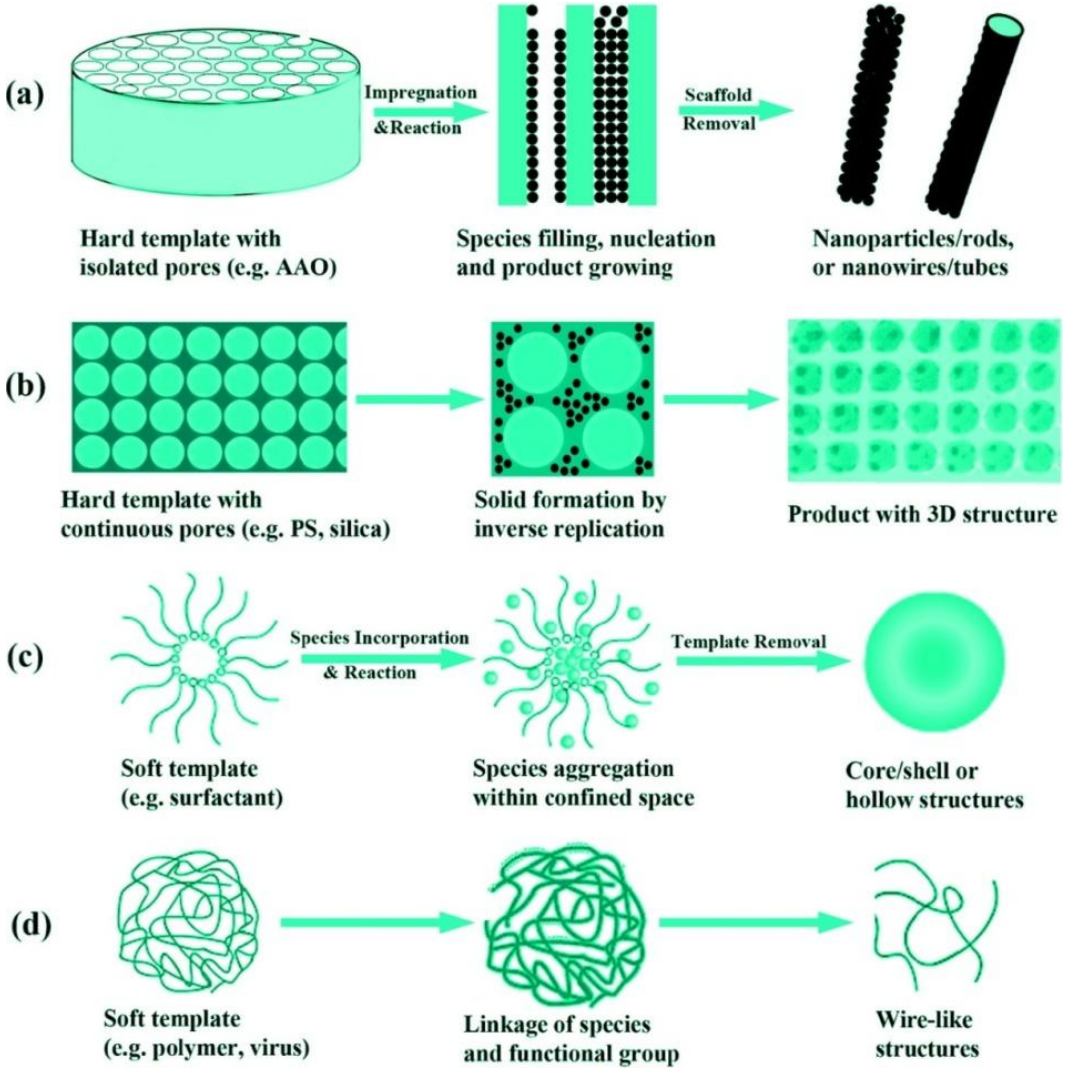

Figure 1.6. Schematic illustration of template synthesis for hard and soft templates (Reproduced with permission from [4]. Copyright 2008 American Chemical Society).

The V_2O_5 electrode material for lithium batteries was the first material successfully prepared through hard template method [42]. The pore sizes of the product are in the range of 10 – 30 nm. The product with small pores shows higher capacities at higher discharge rates due to improved charge transports. Following the successful preparation of porous V_2O_5 material, other electrode materials have been prepared by using hard template, such as SnO_2, $LiNiO_2$, TiO_2, $Li_4Ti_5O_{12}$, $LiMn_2O_4$, $LiFePO_4$, and porous carbon [43-48]. In order to improve the electrochemical properties of porous $LiFePO_4$, carbon coating is performed to form

$LiFePO_4$/C composites [49-52]. The preparation of porous $LiFePO_4$/C composites can be done by using various organic templates as sacrificial hard templates, such as porous polycarbonate, mixed-cellulose, and cellulose [53].

1.3.2. Soft Templates

Soft templates can be utilized as structure-directing agents that assist in the assembly of reacting species. Due to their unique anisotropic structures and the functional groups, controlled fabrication of nanomaterials can be achieved easily by using the soft templates, such as surfactants, long-chain polymers, viruses, and peptide. These soft template materials can be assembled into micelle/vesicle aggregates or liquid crystal phase under certain conditions. The assembled materials restrict and direct the growth of a guest structure [54]. The guest structures react inside the confined space of surfactant micelles; while for polymer, virus chains, and peptide nanofiber, the reaction happens on the surface. The reaction between soft templates and the guest materials is driven by self-assembly of the template and interaction between functional groups of templates and guests [55, 56]. After the template removal, sphere-like/wire-like/tube-like structures can be obtained regarding the basic shape of the template aggregates.

Different types of biological soft templates have been employed in the fabricating of iron phosphate. A genetically engineered M13 virus was used to produce amorphous iron phosphate nanowires for the cathode of lithium-ion batteries [57]. The diameters of the produced iron phosphate are in the range of 10 to 20 nm. Using this negatively charged virus, the fabrication of iron phosphate could be done without thermal treatment through low-temperature. The electrochemical properties of the result materials were comparable with the iron phosphate treated at high temperature.

DNA was also studied as the platform for the direct growth of iron phosphate nanoparticles on the sugar-phosphate backbone of the DNA [58]. Double-walled carbon nanotubes were also used in this system to increase the conductivity of the iron phosphate. DNA is attached onto the double-walled carbon nanotubes via its aromatic bases. The capacity of the product is found nearly same with the theoretical storage capacity of iron phosphate.

The nanostructured iron phosphate is also able to be formed via biomimetic mineralization of peptide nanofibers [59]. These self-assembled peptide nanofibers contain acidic and polar moieties on the surface that act as the nucleation sites for the growth of inorganic iron phosphate. The iron phosphate mineralized peptide nanofibers were heated until 350 °C to form nanotubes with a thin layer of conductive carbon. The result materials perform high reversible capacity and good capacity retention.

1.4. Peptide Amphiphile (PA) Nanofibers

Amino acids that are the building blocks of peptide sequences and proteins contain an alpha carbon in the center where a hydrogen atom, an amino group, a carboxyl group, and a side chain are attached to alpha carbon [60]. Every amino acid has different side chain group leading to different structures, physicochemical properties, and biological functions of each amino acid. By considering the side chain groups, amino acids can be classified into charged, polar, non-polar, and aliphatic amino acids.

Two amino acids are attached to each other by the peptide bond (amide bond). This peptide bond is a covalent chemical bond formed between the carboxyl group of the first amino acid and amino group of another amino acid through condensation reaction with side product of water molecule. The synthesis of peptide (longer sequence of amino acids) can be conducted by using solid phase peptide synthesis method, which is easy to prepare and purify the peptide sequence.

In the past, amino acids were not considered to be useful materials for materials engineering. However, after some recent developments in biotechnology, genetic engineering, and synthetic materials chemistry, the amino acids have been considered as promised building blocks for development of novel materials due to the ability of being a molecular self-assembly. Molecular self-assembly is the process of molecules to spontaneously organize into bigger and structured arrangements [61].

Peptide amphiphiles (PAs) are formed from the lipid chains attached to hydrophilic peptide sequences containing charged residues [62]. The peptide

amphiphile molecules tend to self-assemble forming β-sheet secondary structure allowing the formation of 1-D nanostructures through hydrogen bonding [63]. Not only 1-D nanostructure can be obtained, 3D networks are also formed from the self-assembled peptide amphiphile.

1.4.1. Design of Peptide Amphiphile Molecules

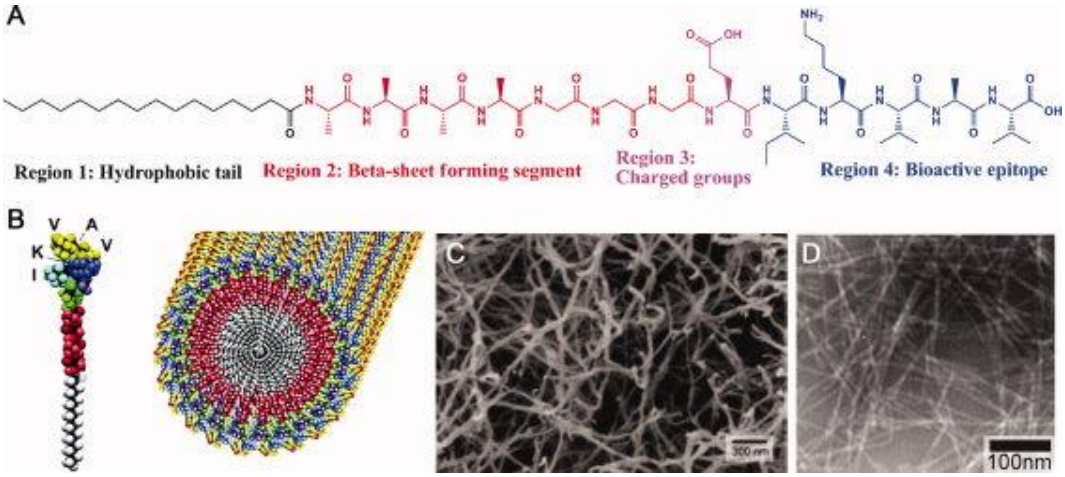

Figure 1.7. 3-D networks of PA nanofibers. (a) Chemical structure of representative PA, (b) schematic representative of PA nanofiber formation, (c) SEM of 3-D network PA nanofiber, and (d) TEM of PA nanofibers (Reproduced with permission from [64]. Copyright 2008 John Wiley and Sons).

The PA molecules usually consist of four regions, which are a hydrophobic tail, a short β-sheet forming peptide sequence region, a charged amino acid region, and a bioactive epitope region (Figure 1.7) [65, 66]. The presence of hydrophobic tail, such as palmitoyl or lauryl groups generates the strongly amphiphilic nature of the PA [67]. The second region next to the hydrophobic tail is the short peptide sequence composed of hydrophobic amino acid residues. These hydrophobic amino acid residues tend strongly to form intermolecular hydrogen bonding in the form of β-sheet secondary structure leading to the 1-D nature of the self-assembled nanostructures that later entangle into networks [64]. The third region which is the charged amino acid residues adjacent to the β-sheet forming peptide sequence can be used as the functional region for the various purposes without changing the

cylindrical geometry. The number of charged amino acids in the sequence of PA is very critical since too much of charged amino acids can interfere the self-assembly of PAs into 1-D nanostructures under physiological conditions. On the other hand, charged amino acids are important in order to increase the solubility of the system in water. Due to the condition of charged amino acids that is relatively weak acids or weak bases, the self-assembly of peptide amphiphile into 1-D nanostructures can be induced by changing pH of the solution or raising the concentration of screening ions in the solutions [64]. The last region that is composed of bioactive epitopes is not always provided in PA sequence since it is usually only used in biomedical applications, such as tissue engineering, regenerative medicine, and drug delivery.

1.4.2. Synthesis of Peptide Amphiphile Molecules

The history of peptide was started 100 years ago when Emil Fischer and Ernest Fourneau synthesized the first peptide that was glycylglycine from glycine dihydride [68]. Nowadays, the most used technique for synthesizing longer sequence of peptide is solid phase peptide synthesis (SPPS). This method is based on the solid insoluble bead (resin) modified with linkers where the coupling process is started [69]. The protecting group at N-terminus of the amino acid such as 9-Fluorenylmethyloxycarbonyl (Fmoc) or tert-Butoxycarbonyl (t-Boc) is utilized to prevent the undesired reactions that may occur during the coupling process. The free unprotected N-terminus amino acid on the resins is coupled to C-terminus amino acid with protected N-terminus. The N-terminus is deprotected prior to coupling process with the next amino acid residue in the sequence. The consecutive steps of coupling, washing, deprotecting, washing are repeated until the desired peptide sequence is achieved. At the last step, the linker between the resin and peptide is cleavaged by using trifluoroacetic acid (TFA) solution in order to separate between the solid phase resin and the synthesized peptide solution.

1.5. Applications of Self-Assembly Peptide Amphiphile Molecules

Self-assembly is the process of smaller molecules associating into ordered 3-D structures via noncovalent interactions including hydrogen bonds, hydrophobic,

electrostatic, metal-ligand, π-π, and van der Waals interactions without the guidance of an external source [70]. Although the noncovalent interactions are the main reason of the self-assembly in which has lower energy than covalent bonds, the highly organized, and robust structures can be formed from these noncovalent interactions. The self-assembly can be found naturally in living cells, such as: self-assembly of lipids during cell membrane formation, protein folding, DNA double helix formation, virus formation, microtubules involved in cell division, and flagella in bacteria [71]. These self-assembly processes in nature are used as the inspiration for developing new biocompatible, biodegradable, and biofunctional materials.

Peptide amphiphile molecules are capable to self-assemble forming various well-ordered nanostructure materials due to the amphiphilic nature. In recent years, self-assembled peptide amphiphile molecules have been utilized in some applications, such as: regenerative medicine, drug, and gene delivery, hybrid materials, and template in synthesis of inorganic materials. Most of them are bioinspired and biomimetic materials that are designed by imitating the models, the systems, and the elements in nature.

1.5.1. Regenerative Medicine

By providing appropriate platform in regenerative medicine, new tissues can be formed at wound area with better healing process. In order to obtain the proper support materials, the self-assembled peptide amphiphile molecules can be employed as synthetic extracellular matrix materials. These extracellular matrix materials provide biological, chemical, and physical cues mimicking the natural environment of the cells.

The self-assembled peptides were used as the building materials of synthetic neural scaffold [72]. Two peptide molecules (laminin mimetic peptide amphiphile and heparan sulfate mimetic peptide amphiphile) were designed by mimicking neural extracellular matrix. The self-assembled nanofibers constructed from these peptide amphiphile molecules show the ability to promote neurite outgrowth of PC-12 cells even if there are inhibitory components of the central nervous system. Another type of peptide amphiphile molecule, glycosaminoglycan mimetic peptide

amphiphile was employed as a platform for cartilage regeneration [73]. The cartilage tissue has low regeneration capacity that brings a significant health problem. According to the results, glycosaminoglycan mimetic peptide amphiphile scaffold gives a promising result for cartilage regeneration.

1.5.2. Drug and Gene Delivery

Specific targeting and cellular internalization strategies for therapeutic agents can be achieved by using self-assembled nanostructures. Peptide functionalized liposomes [74] and nanofibrous peptide networks [75] are some examples of the peptide amphiphile molecules that can be used in smart drug delivery systems. Using these peptide molecules, enhanced efficacy of the drugs can be exhibited.

Liposomes are well known as drug nanocarriers due to their biocompatibility, biodegradability, and their cell membrane mimicking abilities [76]. The positively charged peptide amphiphile molecule was integrated into a negatively charged liposome in the presence of cholesterol via noncovalent interaction [74]. The peptide integrated liposome can be used as the carrier agent for anti-cancer drugs, doxorubicin-HCl, and paclitaxel in which the enhancement in liposomal uptake and efficacy of the drugs are observed.

A self-assembled peptide nanofibrous network was studied as the carrier platform for controlled delivery of oligonucleotide [75]. Oligonucleotide has been used as therapeutic agent for several disorders including cancer [77]. The network of the platform was prepared from cationic peptide amphiphile and oligondeoxynucleotide (ODN) via electrostatic interactions. Oligonucleotide release was controlled by changing the peptide amphiphile and oligonucleotide concentration in the PA-ODN network. According to the results, peptide amphiphile does not only control the ODN release, but also enhances the cellular uptake.

1.5.3. Hybrid materials

The peptide amphiphile molecules have been integrated to various types of nanoparticles via noncovalent interactions aimed at enhancing the function of the

specific nanoparticles. For example, integrated iron oxide [78] and mesoporous silica [79] can be applied for bioimaging and controlled drug delivery, respectively. These hybrid materials are able to be used in vitro experiment due to water soluble and biocompatible.

Magnetic resonance imaging (MRI) is a non-invasive method used for taking images of organs and structures inside the body via magnetic field and radio wave pulse. Some contrast agents with low toxicity level are functionalized to enhance the MRI signal, such as superparamagnetic iron oxide nanoparticles (SPIONs) [78]. In order to suppress the toxicity level of the SPIONs, peptide amphiphile molecules are used to coat the contrast agents via noncovalent interaction. According to the in vitro cell culture experiments, the peptide amphiphile molecules do not only enhance the biocompatibility and the solubility of the contrast agent but also can be used to target specific tissues.

Peptide amphiphile molecules were also employed in development of mesoporous silica nanoparticles (MSNs) in order to improve the cellular uptake and decrease the toxicity level [79]. The amphiphile molecules cover the hydrophobic organosilane surfaces of mesoporous silica nanoparticles. According to the result, 100 μg/mL of the hybrid material is non-toxic to the A10 cells and HUVEC.

1.5.4. Template in Synthesis of Inorganic Materials

The noncovalent interactions during the self-assembly process are important for constructing various self-organized supramolecular nanostructures. The peptide can be used as soft templates for synthesizing inorganic materials by mimicking the biomineralization process. The controlled fabrication of inorganic nanostructures over the size and structure can be obtained easily by using these types of templates. In addition, the modification of the template regarding the chemical functionality, architecture diversity, and physical properties can be done relatively easy [80, 81]. However, there are still some major problems with these templates, such as unstable at high temperature, liable with organic solvents, and easily degradable [82].

TiO_2 and ZnO nanonetworks were prepared by bioinspired peptide nanofiber templates with high coating conformity, uniformity, and atomic scale size control [83]. The inorganic materials were deposited on the template surfaces using an atomic layer deposition technique. TiO_2 and ZnO nanonetworks exhibit better photoexcitation properties compared to the unstructured TiO_2 and ZnO materials due to the enhanced surface area with nanostructure morphology.

Due to versatile chemical and physical properties, the peptide amphiphile molecules were used in the synthesis of catalytic metal nanostructures [81]. The peptide nanofiber template Pd^0 hybrid nanocatalyst was prepared for mild and efficient Suzuki-Miyaura coupling reactions. The Palladium ions coordinate to the peptide via lone pair electrons of side-chain of the amino acid residues in the peptide. The hybrid nanocatalyst shows high catalytic activity in Suzuki-Miyaura coupling reactions. In addition, the nanocatalyst is still able to be isolated and reused after 5 times reactions without loss in activity and structural integrity.

1.6. Purpose of the Experiment

The synthesis of different morphology of iron phosphate nanostructures was done by using two different peptide amphiphile molecules as the templates. The self-assembly mechanism of these peptides can be induced either by tuning the pH or introducing the metal ions into the systems that later can be observed from the formation of a hydrogel. In this study, the peptide amphiphile molecules triggered by Fe^{3+} ions can self-assemble to form β-sheet secondary structure leading to formation of nanostructure that is essential for the formation of organic-inorganic core shell materials. In addition, the functional groups at the periphery of the peptides can be used to attach the Fe^{3+} ions providing the nucleation sites for the growth of the inorganic material on the surface of template nanostructures. The growth of the inorganic layer of $FePO_4$ should be kept by repeating the immersion cycles of the peptide hydrogel in the precursor solutions. Later, critical point dryer was used to change the physical form of the hydrogels into aerogels in order to remove the water content of the as-prepared materials. The aerogels should be calcinated in order to remove the peptide template and produce anhydrous product that is

preferred as the cathode materials. Analyses of the samples were performed by using some techniques, such as HPLC-MS, CD, TEM, STEM, E-SEM, FT-IR, TGA, XRD, XPS, and ICP. Finally, the electrochemical performances of each of different morphology of iron phosphate electrodes are analyzed and compared with each other.

CHAPTER 2

RESULTS AND DISCUSSION

2. RESULTS AND DISCUSSION

2.1. Materials and Method

2.1.1. Chemical and Reagents of Peptides Synthesis

9-Fluorenylmethoxycarbonyl (Fmoc) and tert-Butoxycarbonyl (tBoc) protected amino acids, MBHA Rink Amide resin, Fmoc-Glu(OtBu)-Wang resin, and 2-(1H-Benzotriazol-1-yl)-1,1,3,3-tetramethyluronium hexafluorophosphate (HBTU) were purchased from NovaBiochem and ABCR. Lauric acid, N,N-diisopropylethylamine (DIEA), piperidine, acetic anhydride, and trifluoroacetic acid (TFA) were purchased from Merck. N,N-dimethylformamide (DMF), dichloromethane (DCM), and diethyl ether were purchased from Sigma-Aldrich. Triisopropylsilane and phosphonoacetic acid were purchased from Alfa Aesar. The chemicals were used as received, without any purification.

2.1.2. Chemical and Reagents of Iron Phosphate Synthesis

Iron (III) chloride ($FeCl_3$) was purchased from Merck. Lithium phosphate monobasic (LiH_2PO_4) and sodium phosphate monobasic (NaH_2PO_4) were purchased from Sigma-Aldrich. Tris buffer with pH of 7.2 was prepared by mixing Trizma Base (Tris(hydroxymethyl)aminomethane) and Trizma HCl (Tris(hydroxymethyl)aminomethane hydrochloride) that were purchased from Sigma-Aldrich.

2.1.3. Chemical and Reagents of Lithium-Ion Battery

Multi-walled carbon nanotube (MWCT), lithium bis(trifluoromethanesulfonyl) imide (LiTFSI), ethylene carbonate (EC), and dimethyl carbonate (DMC) were purchased from Sigma-Aldrich. Isopropanol was purchased from Merck. Nafion DE 520 was purchased from Dupont. Celgard C480 membrane was purchased from Celgard. Glass microfiber filter (GF/C) was purchased from Whatman.

2.2. Instrumentation

2.2.1. Liquid Chromatography – Mass Spectroscopy (LC-MS)

1 mL of water was used to dissolve 1 mg of peptides. The solutions were sonicated for 15 min. LC-MS measurements were performed using Agilent Technologies 6530 Accurate-Mass Q-TOF LC-MS with electrospray ionization (ESI) source equipped with reverse-phase analytical high performance liquid chromatography (HPLC). Agilent Zorbox Extend-C18 column was used together with mixture of two different solutions of 0.1% (v/v) ammonium hydroxide – water (A) and 0.1% (v/v) ammonium hydroxide – acetonitrile (B). The flow of mobile phase was 0.65 mL/min with composition of 98% A – 2% B at first 2 min. From 2 to 20 min, the flow of B increased until 100% B and turned back again to 2% again for the next 5 min. LC chromatogram was obtained at wavelength of 220 nm.

2.2.2. Preparative – High Performance Liquid Chromatography (Prep-HPLC)

An Agilent 1200 preparative reverse-phase HPLC system equipped with a Gemini 5u C18 110A column with size of 100× 21.20 mm 5 micron for negatively charged samples was used to purify the peptides. 0.1% (v/v) ammonium hydroxide – water (A) solution and 0.1% (v/v) ammonium hydroxide – acetonitrile (B) solution were mixed and used for the mobile phase. 100 mg of peptides were dissolved in 10 mL of 0.1% (v/v) ammonium hydroxide – water and injected into the system.

2.2.3. Critical Point Dryer (CPD)

Ethanol exchange was done before transferring the peptide gels into CPD in order to exchange the water content of the hydrogels with ethanol. Because water was immiscible in CO_2, ethanol was used as the intermediate solvent to dehydrate the gels before being infiltrated by CO_2. Ethanol is miscible in both water and CO_2. The hydrogel samples were dehydrated in gradually increasing concentrations of 20%, 40%, 60%, and 80% (v/v) ethanol solutions for 10 min in each solution to

avoid the sample being shrunken and subsequently transferred to 100% ethanol for 2 h waiting period. The samples then were dried at the critical point of carbon dioxide (31 °C and 1072 psi) using the Tousimis Autosamdri-815 B, Series C critical point to obtain undamaged dry peptide network of the gel [84].

2.2.4. Circular Dichroism (CD)

The secondary structure of the peptide hydrogels was determined by using JASCO J815 CD spectrometer at room temperature. 1 mg of each peptide was diluted into 90 μL of double-distillated water and sonicated to achieve homogeneous solution. 10 μL of HCl and 10 μL of $FeCl_3$ solutions were introduced into different flasks of peptide solutions leading to the formation of self-assembled hydrogels. The final concentration of self-assembled peptide hydrogels was 1% (w/v). This value was equivalent to 15.27 mM for E-PA and 11.06 mM for Phos-PA hydrogel. The peptide hydrogels (E-PA/$FeCl_3$, E-PA at acidic pH, Phos-PA/$FeCl_3$, and Phos-PA at acidic pH) were diluted until the concentration fell to 0.025% (w/v) that was around 3.818×10^{-4} M for E-PA and 2.765×10^{-4} M for Phos-PA.

Other samples such as peptide solutions at physiological pH (pH 7.4), E-PA/$FePO_4$, and Phos-PA/$FePO_4$ were also measured. In order to prepare peptide solution at neutral pH, 1 mg of peptide amphiphile molecules were diluted, sonicated in 100 μL of double-distillated water and subsequently diluted 40 folds. The preparation for E-PA/$FePO_4$ and Phos-PA/$FePO_4$ were done by diluting 1 mg of each peptide into 80 μL of double-distillated water. 10 μL of $FeCl_3$ solution was dropped onto each peptide solution to form the hydrogel. Later, 10 μL of NaH_2PO_4 solution was introduced to each peptide hydrogel. Each of the hydrogels were then diluted 40 folds prior to measurement.

1 mm thick quartz was used to perform the measurements. Around 300 μL of diluted peptide mixture solutions were put into the quartz and measured from 300 to 190 nm, with data interval and data pitch of 0.1 nm, scanning speed of 100 nm/min, and three times of accumulations. Digital integration time (DIT) was selected as 1 s, bandwidth as 1 nm, and standard sensitivity.

Molar ellipticity [θ] with the unit of deg.cm^{-2}.dmol^{-1} was calculated using the following equation:

$$[\theta] = \frac{100 \text{ x } \theta}{C \text{ x } l}$$

Where, θ: measured ellipticity (mdeg),

C: peptide concentration (molar),

l : cell path length (cm).

2.2.5. Environmental – Scanning Electron Microscopy/Energy Dispersive X-Ray Analysis (E-SEM/EDX)

The morphology of the fabricated samples was visualized by using FEI Quanta 200 FEG environmental scanning electron microscope with an ETD detector. The samples were sputter coated with 8 nm of gold/palladium prior to imaging. The EDX spectra of the samples were collected from the area at 300x magnification of the non-coated samples to obtain the chemical composition. The quantification of the EDX spectra was taken to obtain the Fe/P ratio in the samples.

2.2.6. Transmission Electron Microscopy (TEM) and Scanning Transmission Electron Microscopy (STEM)

The diluted samples which were casted on a Lacey mesh ultrathin carbon coated copper grid were put into FEI Tecnai G2 F30 for taking the transmission electron and scanning transmission electron micrographs. The samples were prepared by diluting 1% (w/v) of peptide hydrogels with double-distillated water to reduce the concentration until 0.025% (w/v) without any sonication then casted on the grids. Negative staining was performed using 2% (w/v) uranyl acetate for samples that did not contain any inorganic metal residue in order to get better contrast images. On the other hand, calcined samples that did not contain any organic template anymore were diluted in ethanol.

2.2.7. X-Ray Photoelectron Spectroscopy (XPS)

The surface characterization of organic-inorganic core-shell samples was done by using a Thermo Scientific XPS spectrometer with Al-Kα monochromatic (100 – 400 eV range) X-ray source and ultra-high vacuum (~10 – 9 Torr). The sample powders were put on the cupper band to conduct the characterization.

2.2.8. X-Ray Diffractometer (XRD)

The crystal structure of the samples was studied by using PAN analytical X'Pert X-ray diffractometer with Cu Kα radiation. The sample powders were scanned in the range of $2\theta = 10 – 60°$ and step size of 0.026°.

2.2.9. Fourier Transform – Infrared Spectroscopy (FT-IR)

The qualitative analysis of the samples was done by analyzing the infrared absorption spectrum of each sample in order to learn the interaction inside the samples. KBr pellet was prepared prior to measurement. In order to prepare KBr pellet, 1 mg of each non-calcined and calcined sample powders was pounded together with 100 mg of KBr. Bruker Vertex 70 FT-IR spectrometer was used for FT-IR analysis with wavenumber range from 4000 to 400 cm^{-1}.

2.2.10. Thermal Gravimetric Analysis (TGA)

The percent composition of inorganic contents in templated $FePO_4$ samples was determined by using a thermogravimetric analyzer (TGA) (Q500, TA Instruments). The temperature was ramped from 25 °C to 500 °C with 10 °C min^{-1} heating rate in the presence N_2 gas. N_2 gas was switched to O_2 gas after the temperature reached 500 °C. The heating process was continued until 800 °C with the same heating rate of 10 °C min^{-1}.

2.2.11. Inductively Coupled Plasma – Mass Spectrometry (ICP-MS)

The amount of iron molecules in the samples was determined by using Thermo Scientific X Series 2 ICP-MS. The value of iron amount will be used to predict the percentage of iron phosphate in the sample. Five different concentration of iron reference solutions (50, 100, 250, 500 and 1000 ppb) were prepared from 1000 ppm iron standard solution. 1 mg of each calcined sample (E-PA/$FePO_4$, Phos-PA/$FePO_4$, and template-free $FePO_4$) was dissolved in 1 mL of conc. HCl and sonicated for 30 min. These solutions were then diluted by adding 2% (v/v) nitric acid until the content of iron in each solution reached 100 ppb by estimation. The exact amount of iron content for each sample was determined by interpolation on the calibration curve.

2.2.12. Multichannel Battery Testing System

Electrochemical testing of the cells was performed with a Landt CT2001A multichannel potentiostat/galvanostat. 5 discharge/charge cycles were applied to the cell with current rates of C/20, C/10, C/5, C, 2C, and C/20; where C represents the current rate at which the theoretical capacity was charged/discharged in 1 h. The voltage was limited in the range of 2.0-4.0 V.

2.3. Peptide Synthesis

Peptide amphiphile molecules were synthesized manually using the method of standard solid peptide synthesis. Two peptide amphiphile molecules, which were E-PA (C12-VVAGE-OH) and Phos-PA (C12-VVAGEK(Phosphonoacetyl)-NH_2) were synthesized on Fmoc-Glu(OtBu)-Wang resin and MBHA Rink Amide resin, respectively (Figures 2.1 and 2.2). First, the resin was swelled with dichloromethane (DCM) solution inside the vessel and agitated for 30 min. Then, vacuum was applied to the vessel to remove DCM. Before attaching the first amino acid residue to the resin, the Fmoc-protected group on the resin was removed by treating the resin with 10 mL of 20% (v/v) piperidine/dimethylformamide (piperidine/DMF) solution for 20 min. Then the resin was washed with DCM and

DMF sequentially in prior to coupling process. In addition, the washing steps were always done after every finished step in order to remove the excess materials from the vessel. First amino acid couplings were performed by pouring the first C-terminal amino acid residue solution that contained of 2 equivalents of N-protected amino acid activated with 1.95 equivalents of HBTU and 3 equivalents of DIEA for each 1 equivalent mol of resin and agitated for at least 2 h. Kaiser Test was performed after each coupling to examine the presence of free amino group on the resin. When the Kaiser Test result showed dark blue color on the resin, it meant there was still free primary amine. The coupling process was repeated when this problem occurred. On the other hand, when there was no any dark blue color on the resin during the test, acetylation was subsequently performed by pouring 10% (v/v) acetic anhydride/DMF solution to the vessel in order to cover the undetectable free primary amine with the acetyl group. To start the second coupling, Fmoc protected group of the first amino was removed by adding 10 mL of 20% (v/v) piperidine/DMF and agitating for 20 min. These sequential steps that were amino acid coupling, washing, Kaiser Test, acetylation, and Fmoc cleavage were repeated until the last sequence of amino acids. The last amino acid was coupled with lauric acid in similar way to amino acid coupling.

For Phos-PA, the protected group (Mtt) at the end of lysine side chain was removed by using 10 mL of 3.25% TFA, 0.125% water, 0.125% triisopropylsilane, and 96.5% DCM. The cleavage was repeated for 5 – 6 times with 5 min shaking for each period. The vessel was washed with DCM and DMF in between the cleavage. The washing solution was collected to observe the changing color of the washing solution from fluorescent color to transparent after each cycle. When the transparent of washing solution was observed, Mtt protected group was successfully remove and 10 mL of DMF solvent that contained 50 μL DIEA was poured to the vessel as the final washing solution to remove excess the TFA from the vessel. Phosphonoacetic acid that was diluted in DMF together with DIEA and HBTU was poured into the vessel and shaken for 1 day in order to bind to the side chain of the lysine.

At the end, each peptide sequence was separated from the resin using a solution that contained of 95% TFA, 2.5% water, and 2.5% triisopropylsilane for

2 h. The vessel was washed only with DCM and collected into the round bottom flask. The removal of excess TFA and DCM from the peptide solution was carried out by using rotary evaporation. The left portion of peptide solution inside of round bottom flask was dispersed in diethyl ether for overnight. The next day, the peptide amphiphile was extracted from diethyl ether by centrifugation and transferred to double-distillated water. The peptide solution was frozen at -80 °C and then lyophilized to get the solid form of peptide. The peptide was purified by using prep-HPLC before being used.

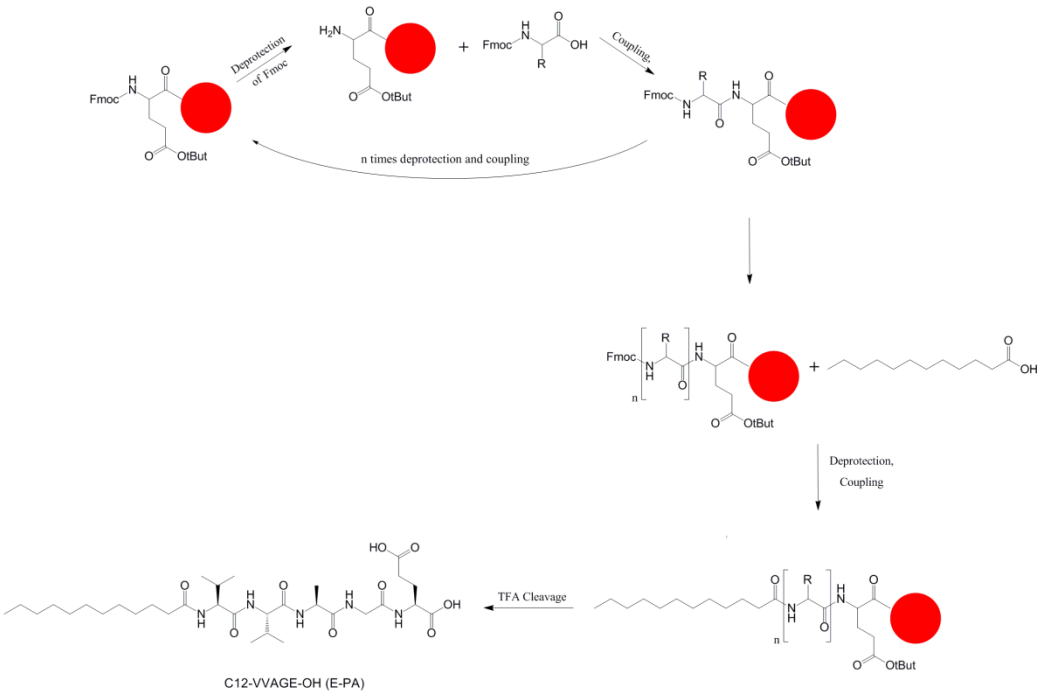

Figure 2.1. Synthetic pathway of E-PA.

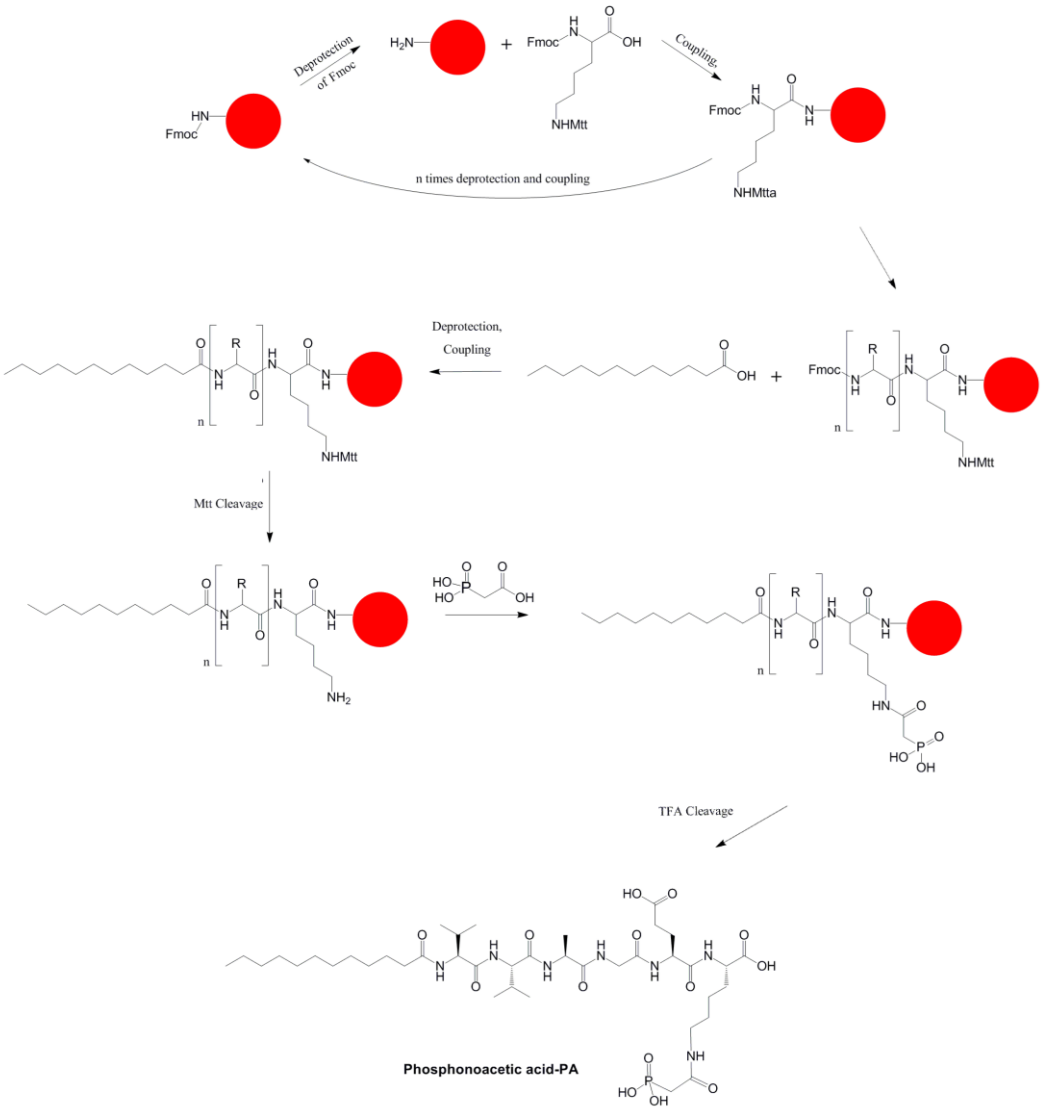

Figure 2.2. Synthetic pathway of Phos-PA.

2.4. Iron Phosphate Nanostructures Produced by Mineralization of Peptide Amphiphile Nanostructures

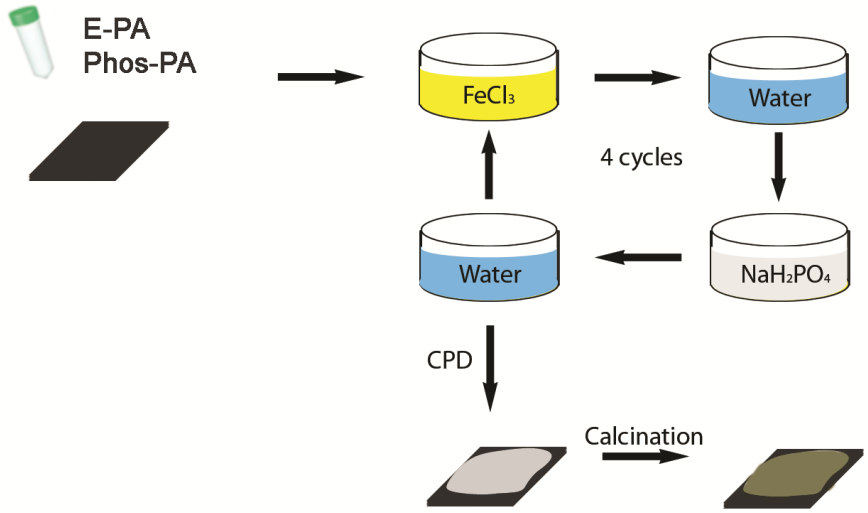

Figure 2.3. Schematic illustration of producing organic-inorganic core-shell of templated-$FePO_4$.

1 mg of each peptide amphiphile molecule was dissolved in different test tubes of 90 µL double-distilled water to form peptide solutions with concentration of 1.11% (w/v). The solutions then were poured on the silicon wafers that had been immersed in piranha solution. This piranha solution increases the content of hydroxyl group on the surface of the silicon wafers and also cleans the surface from the organic content. The peptide hydrogels were formed by dropping 10 µL of iron chloride solution ($FeCl_3$) onto the peptide solutions. The concentration of iron chloride solution for E-PA and Phos-PA was 305.78 mM and 246.91 mM, respectively. The final concentration of peptide in each hydrogel was 1% (w/v). The molar concentrations of these 1% (w/v) peptide hydrogel were 15.27 mM and 11.06 mM for E-PA and Phos-PA, respectively. After waiting for 5 min at temperature of 4 °C, each hydrogel was immersed for 30 min in iron chloride solution which had the same concentration as the previous iron chloride. The hydrogels then were transferred to water batch to remove the excess iron solution on the hydrogel and waited for 15 min. Next, the hydrogels were immersed to

sodium phosphate (NaH_2PO_4) solution for 30 min. The molar concentrations of sodium phosphate for E-PA and Phos-PA hydrogel were 305.78 mM and 246.91 mM, respectively. The yellowish hydrogels started to form white precipitation directly after being treated with NaH_2PO_4 solutions. Then, the hydrogels were washed again with water by waiting in water solution for 15 min. These steps were repeated again until four cycles. All of the processes were done at low temperature (~4 °C) in order to suppress the hydrolysis of Fe^{3+} ions.

After finishing the fourth cycle, the hydrogels were dehydrated using ethanol solution before being transferred to CPD in order to form aerogels which were more stable than hydrogels. The thermal treatment (calcinations) was done step by step in normal air atmosphere. The temperature was increased with heating rate of 5 °C/min until 250 °C and then brought to 350 °C with heating rate of 1 °C/min. The samples were kept at 350 °C for 1 h.

In addition, template-free $FePO_4$ was also prepared by mixing the same concentration and volume of 246.91 mM of $FeCl_3$ and NaH_2PO_4 using a magnetic stirrer for 30 min. The solution was kept inside the oven at 80 °C for overnight to evaporate the water content. The left powder was washed with distilled water and filtered on filter paper. The wet powder was calcined under the same procedure as the templated iron phosphate.

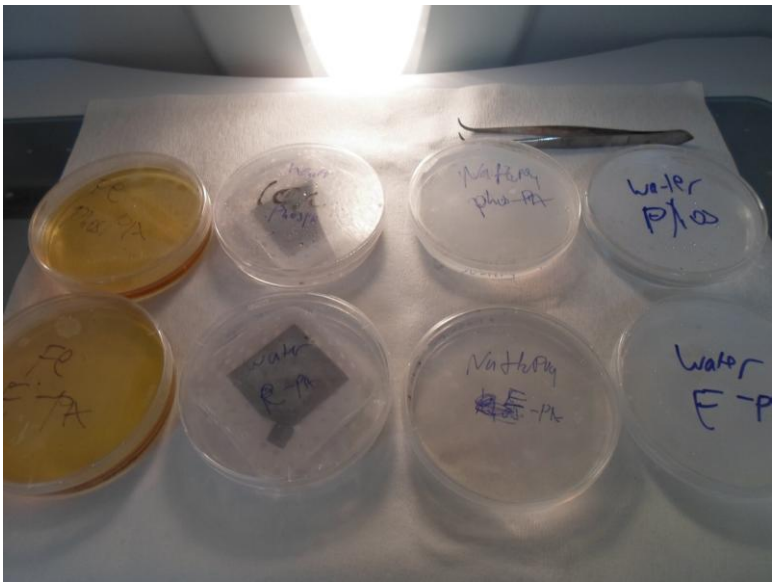

Figure 2.4. The preparation of template-directed $FePO_4$ materials.

2.5. Lithium-Ion Battery Preparation

Templated $FePO_4$ cathode films were produced with two different organic templates and tested against Li/Li^+ electrode in coin cells. The cells were assembled in argon environment within the glovebox to prevent air exposure. The film cathode material was obtained by slurry casting, in which the $FePO_4$ powder was ground together with multi-walled carbon nanotube (MWCT). Afterwards, Nafion binder was dropped to the mixture powder. The percent composition of the mixture according to the total mass of the mixture was 70%, 20%, and 10% of $FePO_4$, MWCT, and Nafion, respectively. The mixture was dispersed in isopropanol and stirred for a couple of days using magnetic stirrer. The mixture solution was casted on a separator (Celgard) film to yield a desired thickness. The casted film was exposed to open air for 1 h, and then the drying process was continued at elevated temperatures (60 °C) for 8 h. Finally, the cathode material was obtained by cutting the film to desired shape and diameter.

A stainless steel current collector having 11 mm diameter was used in the assembly of cell for lithium part. As the counterpart, another stainless steel current collector having 12 mm in diameter was used. Two different separators were used in the cell that were Celgard separator at the Li anode and Glassfiber/C separator at the cathode film. 280 µL of 0.5 M LiTFSI EC-DMC (1:1) was used as electrolyte. After the cell was assembled in the Ar atmosphere, it was sealed to prevent the interaction with the atmosphere.

The cells were rested for 8 h in prior to testing in order to let the electrolyte to diffuse through the cell. Electrochemical testing of the cells was performed with a Landt CT2001A multichannel potentiostat/galvanostat. 5 discharge/charge cycles are applied to the cell with current rates of C/20, C/10, C/5, C, 2C and C/20, while the voltage was limited into 2.0-4.0 V.

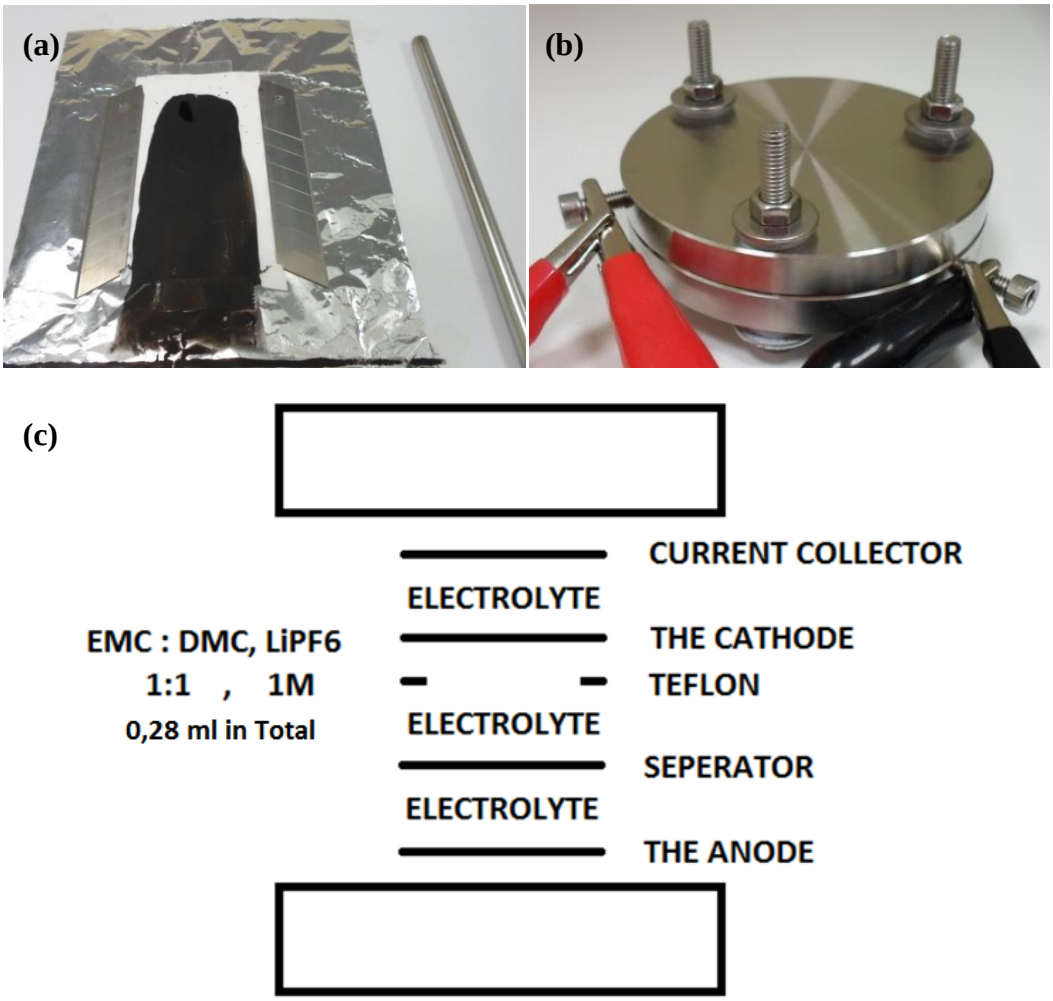

Figure 2.5. Lithium-ion battery preparation. (a) Iron phosphate cathode film, (b) electrochemical testing of the cells, and (c) schematic illustration of Li-ion battery.

2.6. Results and Discussion

The iron phosphate materials were obtained by using organic materials as the templates. These organic materials were synthesized from different types of protected amino acids and hydrophobic alkyl chain by using Solid Phase Peptide Synthesis (SPPS) method to form materials that were called as peptide amphiphile molecules.

In this thesis, peptide amphiphile molecules contain three regions: a hydrophobic alkyl tail, a short sequence of peptide forming β-sheet and a charged head. The hydrophobic alkyl tail which is the reason of the amphiphilicity of the materials can be adjusted by using different alkyl chain lengths and different hydrophobic compounds [67]. The second region which is composed of hydrophobic amino acids has the capability to form intermolecular hydrogen bonding, generally β-sheets. It leads to the formation of nanofibers that later being entangled to form networks [64]. The last region that contains negatively charged amino acid serves as a template for the nucleation of iron phosphate on the surface of nanostructure by forming conjugates with Fe^{3+}. This interaction between negatively charged amino acid and Fe^{3+} prevents the hydrolysis of iron ion [57].

Two different peptide amphiphile molecules that contained the alkyl chain, the short sequence of hydrophobic amino acids and the negatively charged amino acid were designed and synthesized. These peptide amphiphile molecules, lauryl-VVAGEK(Phosphonoacetyl)-Am [Phos-PA] and lauryl-VVAGE-OH [E-PA], were used as a template for $FePO_4$ formation (Figures 2.6a, and b). The main difference between both of the peptide amphiphile molecules was the presence of phosphate group in Phos-PA that could directly conjugate with iron ion.

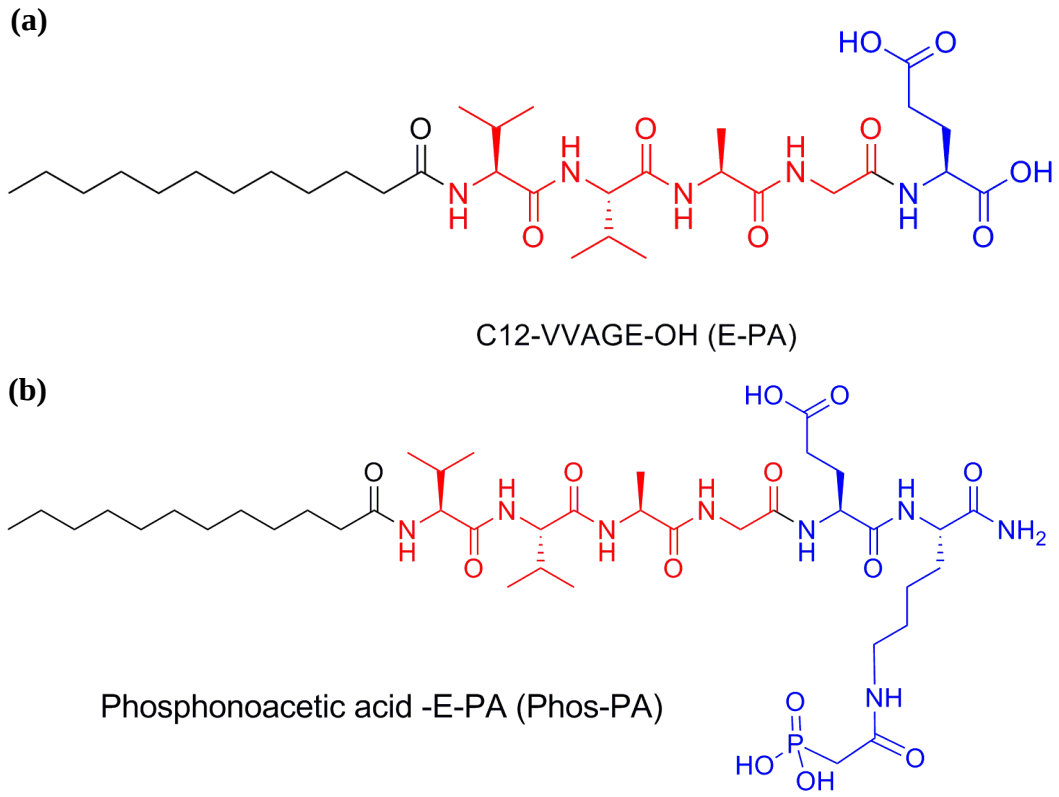

Figure 2.6. Chemical structures of peptide amphiphile molecules. (a) E-PA, and (b) Phos-PA. Black color indicates hydrophobic alkyl tails, red color indicates β-sheet forming short peptide sequence, and blue color indicates charged head.

After the synthesis, the peptide amphiphile molecules were purified using Prep-HPLC after the synthesis aimed at separating the unintended materials from the mentioned peptides. The purified peptide amphiphiles were dissolved in double-distilled water with concentration of 1 mg/mL and then analyzed by using Q-TOF LC-MS to determine the final purity and molecular weight of the peptides. The chromatograms show that the purity of both peptides are more than 95% (Figures 2.7a and 2.8a). According to the mass spectra results of E-PA and Phos-PA, the molecular weights of E-PA and Phos-PA are found as 655 g/mol and 904 g/mol, respectively which are nearly the same with the calculated mass (Figures 2.7b and 2.8b).

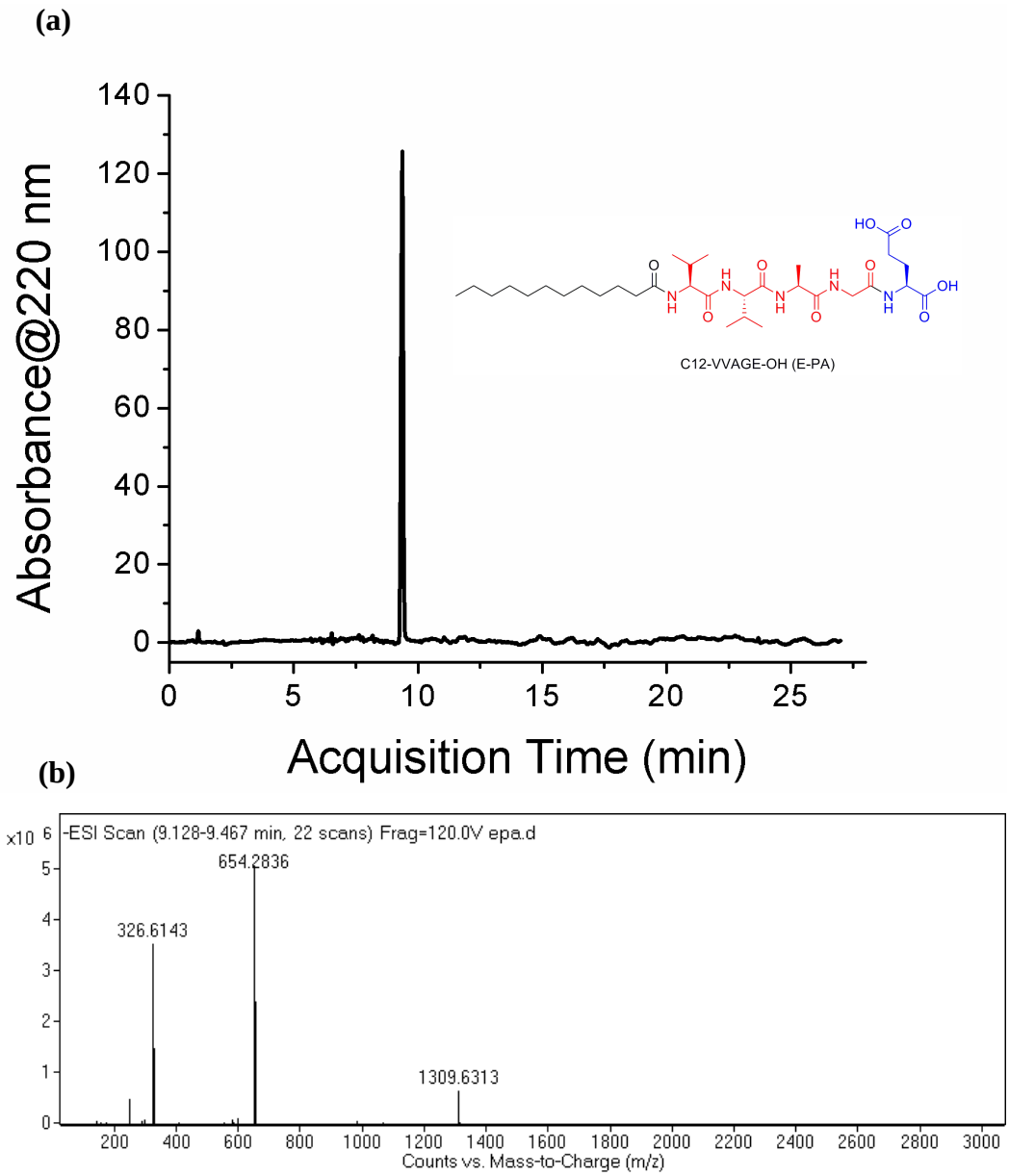

Figure 2.7. Characterization of E-PA by using LC-MS. (a) Liquid chromatogram of E-PA by the absorbance at 220 nm, and (b) mass spectrum of E-PA. MS: (m/z) calculated 655.42, $[M-H]^-$ found 654.2836, $[M-2H]^{2-}$ found 326.6143. $[2M-H]^-$ found 1309.6313.

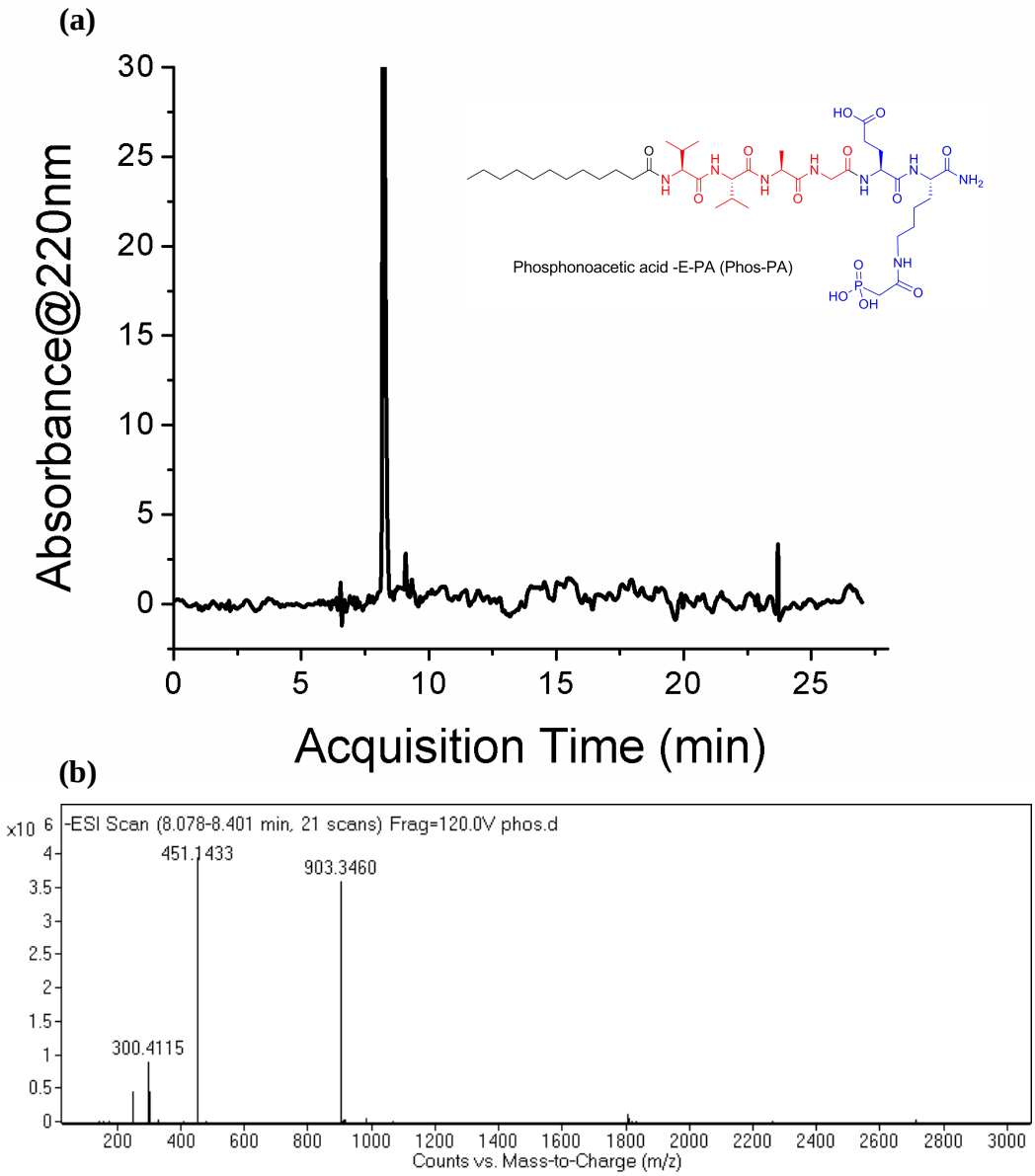

Figure 2.8. Characterization of Phos-PA by using LC-MS. (a) Liquid chromatogram of Phos-PA by the absorbance at 220 nm, and (b) mass spectrum of Phos-PA. MS: (m/z) calculated 904.50, $[M-H]^-$ found 903.3460, $[M-2H]^{2-}$ found 451.1433. $[M-3H]^{3-}$ found 300.4115.

1% (w/v) peptide amphiphile solutions were prepared by dissolving 1 mg of each of E-PA and Phos-PA in 100 μL of double-distilled water. Both of these peptide solutions start to self-assemble after the addition of HCl or metal ions that screen the negative charge of the peptides. Glutamic acid at both of E-PA and Phos-PA bears negative charges at physiological pH and shifts to uncharged state at acidic pH. Together with the other driving forces that are a hydrophobic interaction of alkyl chains and a hydrogen bonding, the peptide amphiphiles start to form aggregates. The self-assembly process of E-PA and Phos-PA at acidic pH is evaluated from the formation of hydrogels (Figure 2.9b, and f). By dropping 5 μL of 1M HCl into the peptide solutions, the hydrogel formation was able to be observed with naked eye. Phos-PA itself has a tendency to form a hydrogel in a couple of minutes even at physiological pH (pH 7.4) after sonication due to weaker electrostatic repulsion.

The hydrogels of E-PA and Phos-PA were also formed by introducing $FeCl_3$ to induce the self-assembly of peptide amphiphile molecules (Figures 2.9c, and g). These 1% (w/v) E-PA/$FeCl_3$ and Phos-PA/$FeCl_3$ hydrogels were later mixed with NaH_2PO_4 to induce the formation of E-PA/$FePO_4$ and Phos-PA/$FePO_4$ (Figures 2.9d, and h). The latter hydrogels have paler yellow color due to precipitation of $FePO_4$.

The secondary structures of self-assembled peptides were probed using circular dichroism (CD). The CD spectra give information about the absorption bands of optically active chiral molecules. In here, the results obtained from CD analysis show the formation of β-sheet structure for all of the self-assembled samples (Figure 2.10). The signals of β-sheet usually consist of minimum peak at 216 nm and maximum peak at 200 nm [85, 86]. The different type of peak is only observed for E-PA solution at physiological pH that shows the formation of a random coil with minimum peak signal at 195 nm. This random coil structure of E-PA disappears and transforms to β-sheet structure either by lowering the pH or introducing the iron ions indicating the self-assembly process. The CD result also explains the self-assembly process of Phos-PA at physiological pH due to the presence of β-sheet structural motif. This result supports the fact that Phos-PA forms hydrogel in a couple of minutes after dissolution.

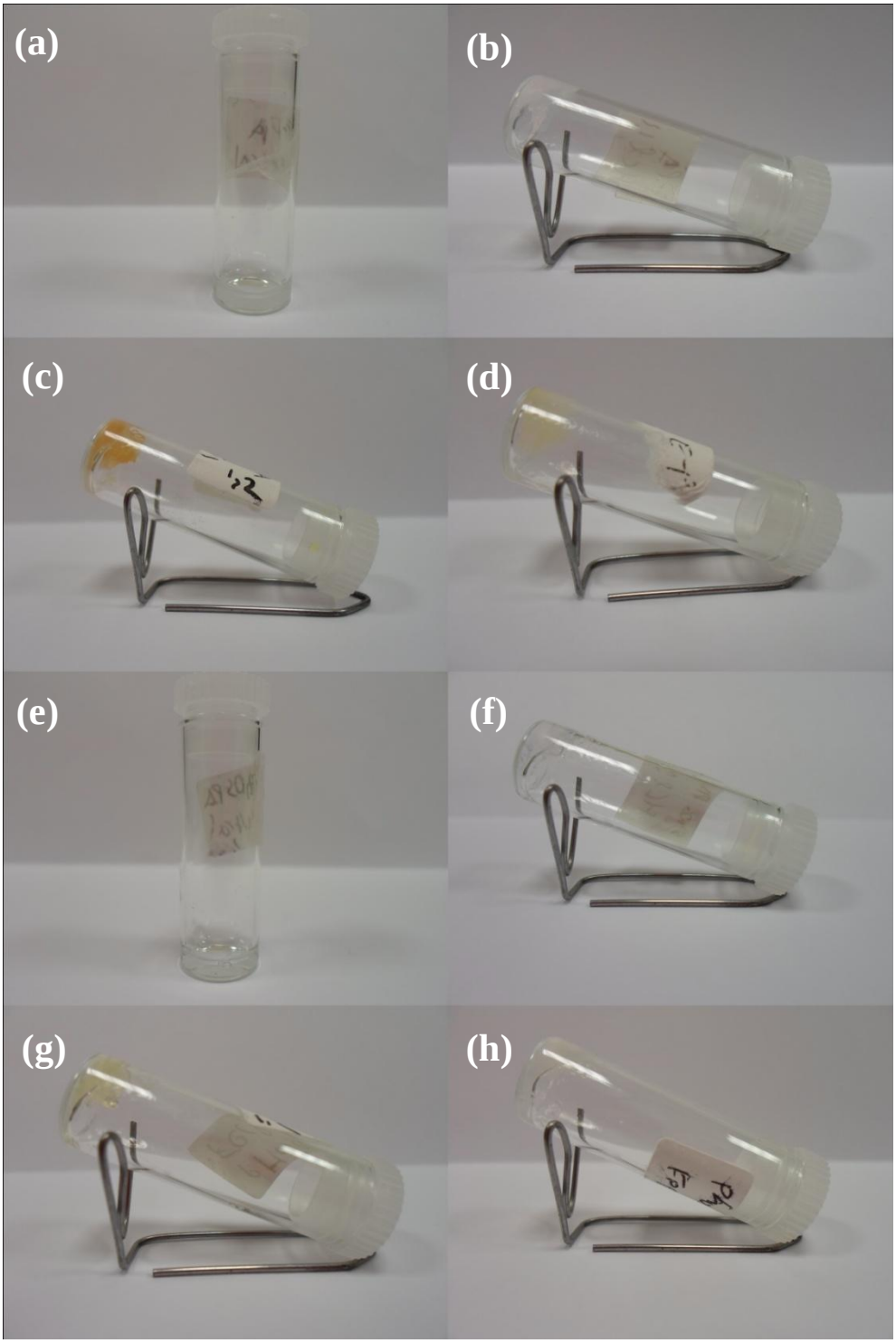

Figure 2.9. The hydrogels formation of peptide amphiphile molecules. (a) 1% (w/v) E-PA was dissolved in double-distilled water, (b) E-PA hydrogel at acidic pH, (c) E-PA/$FeCl_3$ hydrogel, (d) E-PA/$FePO_4$ hydrogel, (e) 1% (w/v) Phos-PA was dissolved in double-distilled water, (f) Phos-PA hydrogel at acidic pH, (g) Phos-PA/$FeCl_3$ hydrogel, and (h) Phos-PA/$FePO_4$ hydrogel.

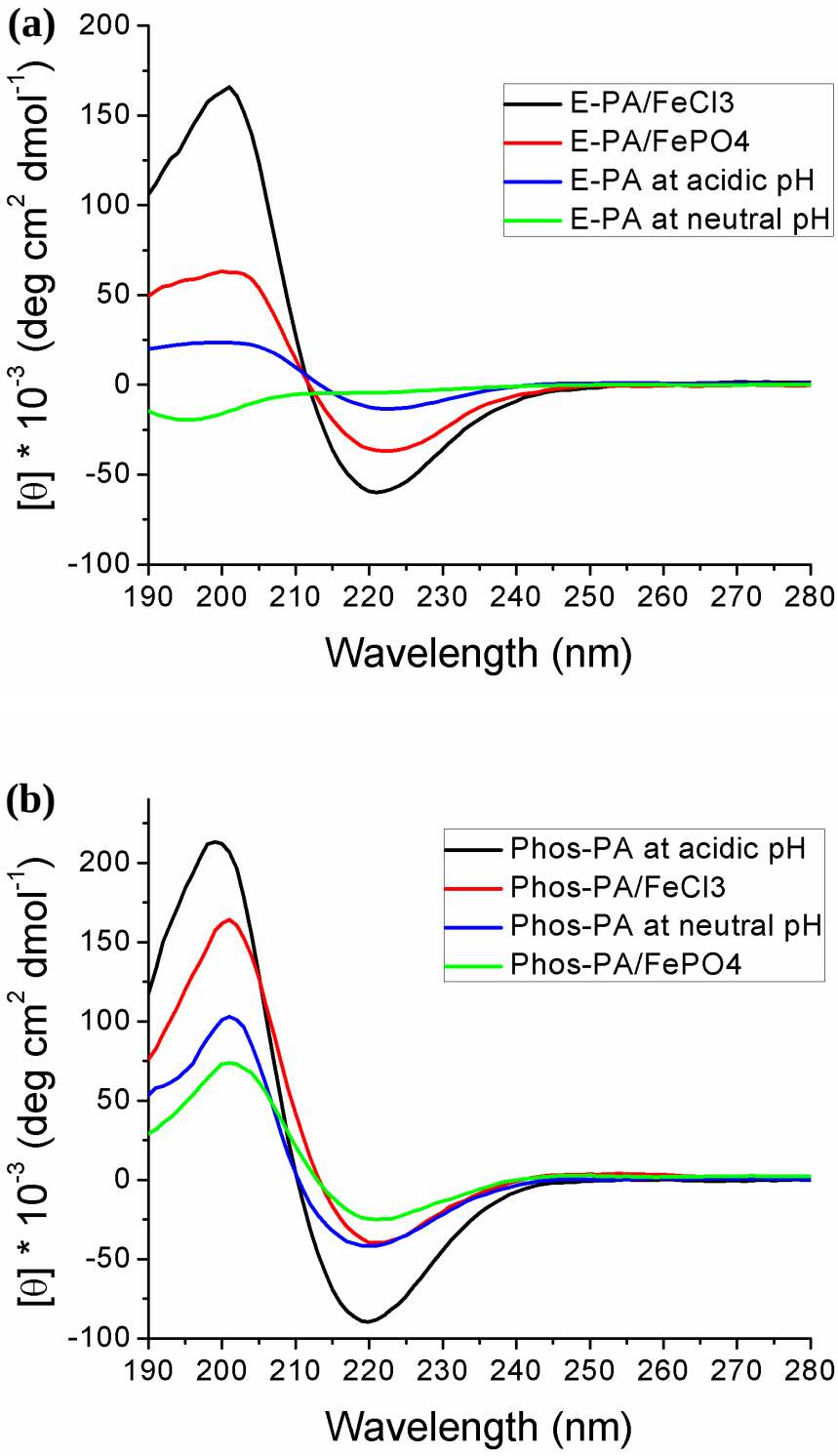

Figure 2.10. Circular dichroism spectra of the secondary structure of peptide amphiphile interactions. (a) E-PA, and (b) Phos-PA.

The negatively charged functional groups of the peptide amphiphile molecules are able to attract the Fe^{3+} ions electrostatically. This interaction decreases the repulsion between each neighboring peptide amphiphile molecule. The iron (III) ions on the surface of the self-assembled peptide nanostructure also act as the nucleation site for the iron phosphate growth. This insoluble $FePO_4$ is the reason behind the decrease in the molar ellipticity of E-PA/$FePO_4$ and Phos-PA/$FePO_4$ (Figure 2.10).

The morphology of self-assembled peptides that were triggered by acidic solution and metal inorganic solutions were provided from TEM and STEM images (Figure 2.11). The negative charge of glutamic acid at physiological pH inhibits the self-assembly by denying each peptide amphiphile molecule to come closer. The repulsive effect of negative charges of PA can be neutralized by acidifying solution or introducing metal ions into the peptide amphiphile solutions. As a result, each peptide amphiphile molecule can interact with each other to form self-assembled nanostructures. The negative-stained transmission electron micrographs of both self-assembled E-PA and Phos-PA at acidic pH show the presence of 1-D nanofibers with average of 10 nm diameters (Figures 2.11a, and b).

$FeCl_3$ can also be employed to induce the self-assembly of E-PA and Phos-PA since the Fe^{3+} ions electrostatically interact with the carboxyl and phosphate group of the peptide. When $FeCl_3$ solution was dropped onto the peptide solution, the self-assembled E-PA and Phos-PA formed different types of nanostructures. Mixture of E-PA and $FeCl_3$ tends to form 1-D nanobelts with the width of 60 nm (Figure 2.11c). The STEM image of E-PA/$FeCl_3$ showed the presence of iron aggregates. On the other hand, the mixture of Phos-PA and $FeCl_3$ forms 1-D nanofibers with diameter of 10 nm that is same with the self-assembled Phos-PA at acidic pH (Figure 2.11d).

The β-sheet structural motif in both self-assembled Phos-PA and E-PA contributes to the nanofiber and nanobelt formation. Glutamic acid side chain may play the major role in the formation of nanobelts for E-PA. In the case of E-PA/$FeCl_3$, the iron ions are not distributed well on the periphery of peptide amphiphile as the morphology of showed the random attachment of iron on the surface of nanobelts. In addition, the nanobelts are related with highly effective

packing between β-sheets with peptide segments leading to the loss of curvature in the aggregates [87]. Even the CD results supported this condition, as the β-sheet intensity of E-PA/$FeCl_3$ is higher than that of acidic E-PA. On the other hand, the longer peptide sequence in Phos-PA may be the reason why only nanofiber formation took place in self-assembled Phos-PA.

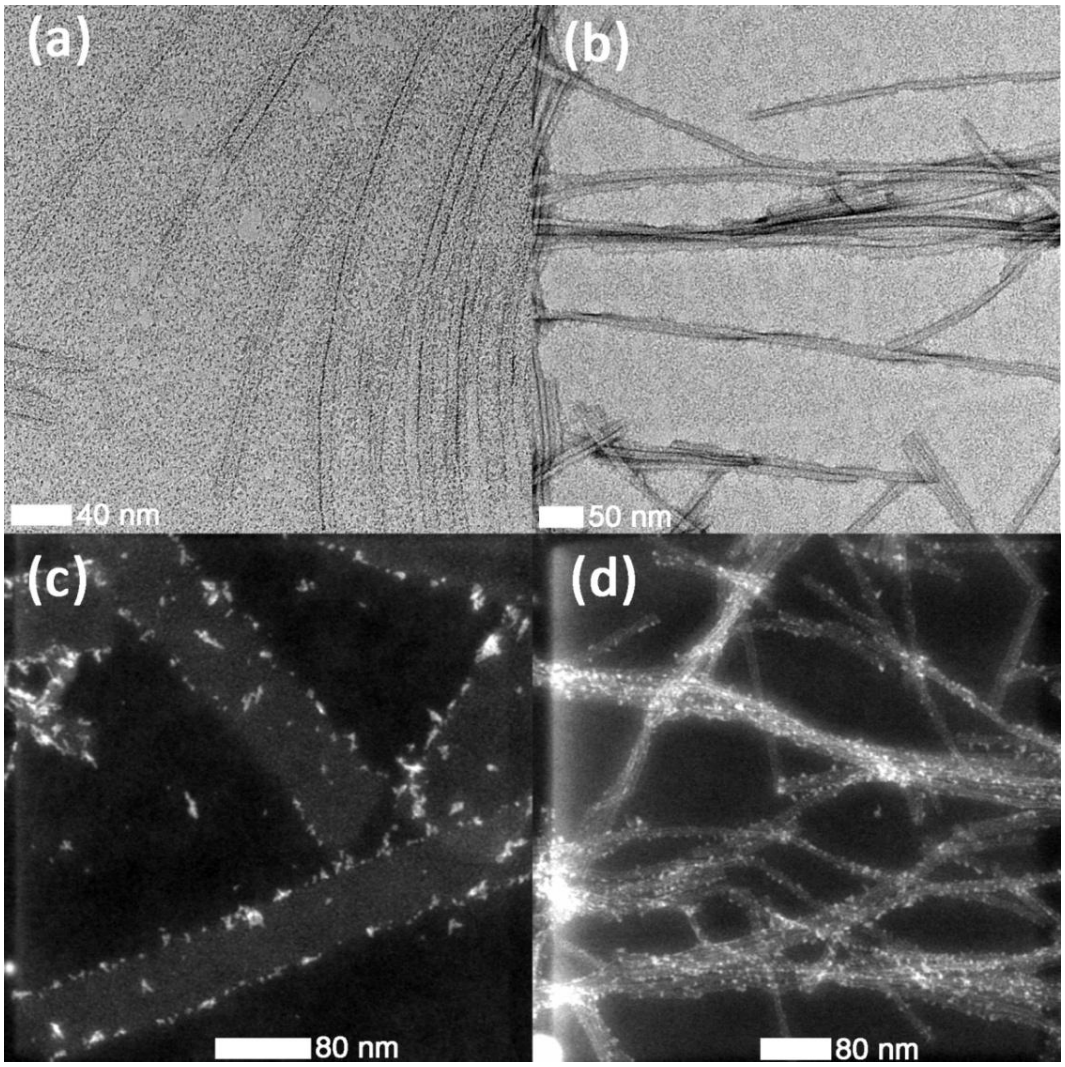

Figure 2.11. STEM and TEM images of self-assembly of peptide amphiphile molecules induced by acidic pH and inorganic materials. (a) TEM image of E-PA at acidic pH stained with uranyl acetate, (b) TEM image of Phos-PA at acidic pH, stained with uranyl acetate, (c) STEM image of E-PA/$FeCl_3$, (d) STEM image of Phos-PA/$FeCl_3$.

Noncovalent interactions including hydrogen bonding, hydrophobic, electrostatic, metal-ligand, and van der Waals interactions are the main reason causing the self-assembly of the peptide allowing the peptide to form nanofiber and nanobelt that later being entangled to form a network. These nanostructures of self-assembled peptide amphiphile molecules can be applied as a template for the formation of $FePO_4$ that is inspired from the biomineralization in nature. The fabrication of inorganic $FePO_4$ materials are achieved in the solution by introduction of iron ions solution that induce the self-assembly process by attaching to the periphery of the peptide electrostatically. The iron ions on the surface of peptide nanostructures also acted as the nucleation sites for the growth of $FePO_4$.

In this experiment, self-assembly of both E-PA and Phos-PA solutions were induced to self-assembly by dropping $FeCl_3$ solution on the surface. A gentle mixing was done to ensure all of the whole peptide solution turned into the hydrogels. The hydrogels were subsequently immersed into a batch that contained cold $FeCl_3$ solution followed by transferring it to NaH_2PO_4 and repeated for some cycles. The color of hydrogels turned yellow after treatment with $FeCl_3$ and then white after forming $FePO_4$. These hydrogels were not stable since they started to collapse after they were exposed to air due to water evaporation.

Critical point drying is the best known method to change the physical form of a hydrogel into a dry peptide network of the gel [84]. In order to to get this aerogel form, it is necessary to replace the water content inside the hydrogels with liquid CO_2 in which the critical point is 31 °C at 1072 psi [88]. These aerogels that contained $FePO_4$ on the surface of self-assembled peptide amphiphile nanonetworks are heated to moderately high temperature in order to obtain inorganic $FePO_4$ materials by removing the organic peptide template. The calcination temperature is brought to 350 °C to obtain amorphous forms of anhydrous $FePO_4$ that has better capacity and cyclability than trigonal, hexagonal and hydrated $FePO_4$ [5, 58, 89, 90].

The morphology of both calcined and non-calcined $FePO_4$ coated peptide amphiphile molecules were taken by using E-SEM (Figures 2.12a-d). For each sample, the peptide network is observed with no significant difference. Even after

calcination, the network structure is thoroughly preserved as it can be seen from the SEM micrographs.

Previously, a templated $LiFePO_4$ was synthesized by using Phos-PA as the soft template (Figures 2.10e, and f). $LiFePO_4$ with olivine structure is well known electrode material as it exhibits various advantages such as high safety, low cost, environmental friendliness, good electrochemical performance, high theoretical specific capacity (170 mAh/g), flat charge-discharge profile at intermediate voltage (3.45 V vs Li/Li^+), and reasonable cycle life [7, 91-99]. However, $LiFePO_4$ itself has poor ionic and electronic conductivity that makes it become less impressive at high rate due to the poor kinetics of lithium intercalation/deintercalation process [100, 101]. The templated $LiFePO_4$ was synthesized by using Phos-PA as a template and LiH_2PO_4 was used instead of NaH_2PO_4 that was used for $FePO_4$. Calcination was being performed until the temperature reached 600 °C for 8 h in order to form crystal structure of olivine. As a result of this high temperature treatment, the network structure of the template collapsed (Figure 2.12f). Due to this result, templated $FePO_4$ is preferred to templated $LiFePO_4$ because $FePO_4$ can be prepared at lower calcination temperature without harming the nanostructure network of organic-inorganic core shell materials although its conductivity still low [102].

The material composition of the iron phosphate-coated peptide amphiphile molecules was determined by using energy dispersive energy X-ray spectroscopy (EDX). The EDX spectra of the calcined inorganic-coated peptide samples confirm the deposition of iron phosphate on the peptide networks as the Fe, P and O peaks are observed in EDX spectrum of both samples (Figures 2.13a, and b). For calcined E-PA/$FePO_4$ powder, the atomic percentages of Fe and P in the sample are found to be 12.21% and 13.50%, respectively (Appendix 2). It means that Fe/P ratio is found to be 0.92 in calcined E-PA/$FePO_4$ sample. The excess amount of phosphorus to iron might indicate the presence of unintended materials although the value was still low. On the other hand, the atomic percentages of Fe and P in the calcined Phos-PA/$FePO_4$ are 12.09% and 12.25%, respectively, with the Fe/P ratio of 0.99 which is close to one. Thus, the obtained Fe/P ratios from EDX results of both of the samples can be used to confirm the formation of $FePO_4$.

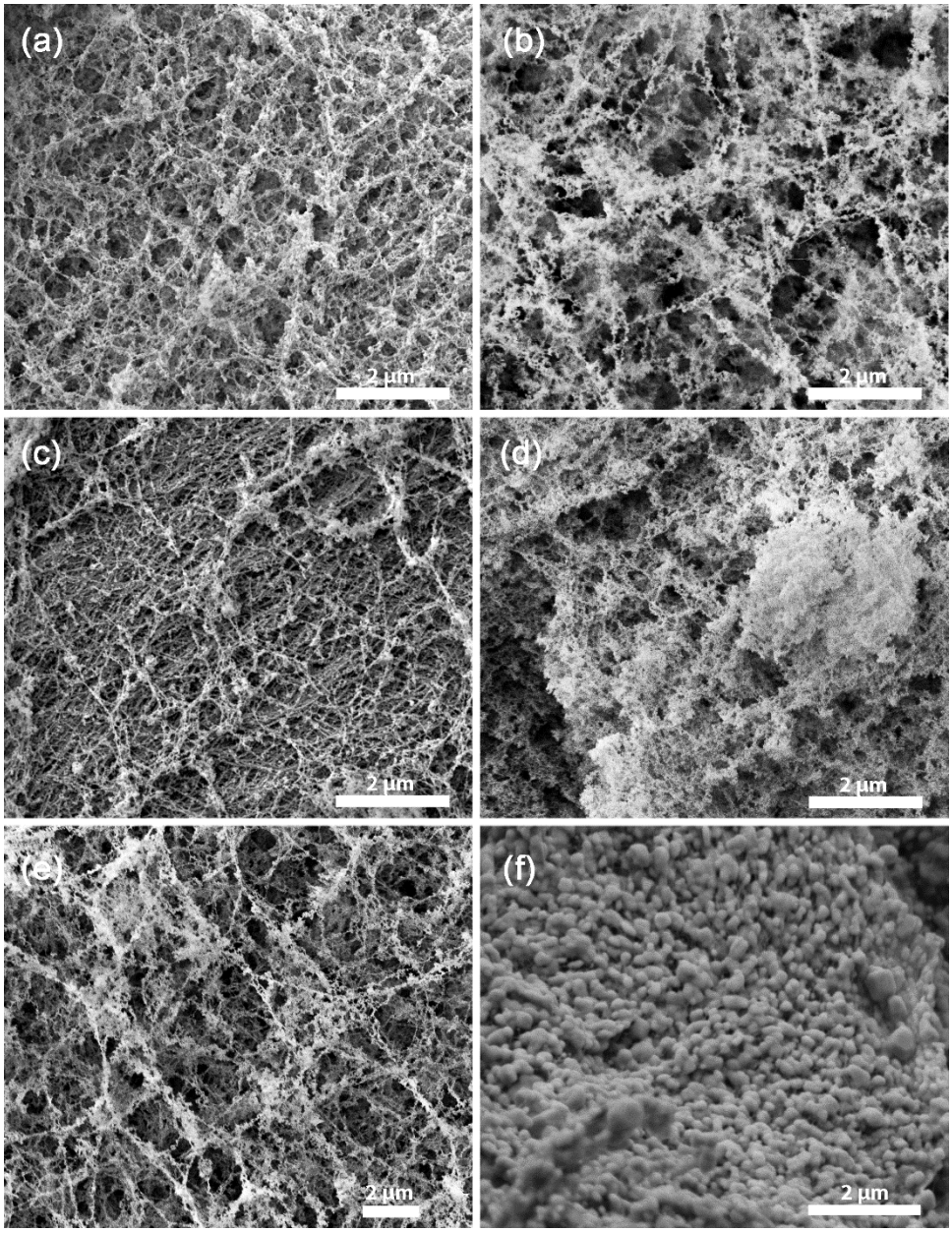

Figure 2.12. SEM images of peptide amphiphile molecules coated with inorganic materials. (a) Non-calcined E-PA/$FePO_4$, (b) Calcined E-PA/$FePO_4$ at 350 °C for 1 h, (c) non-calcined Phos-PA/$FePO_4$, (d) Calcined Phos-PA/$FePO_4$ at 350 °C for 1 h, (e) non-calcined Phos-PA/$LiFePO_4$, (f) Calcined Phos-PA/$LiFePO_4$ at 600 °C for 8 h.

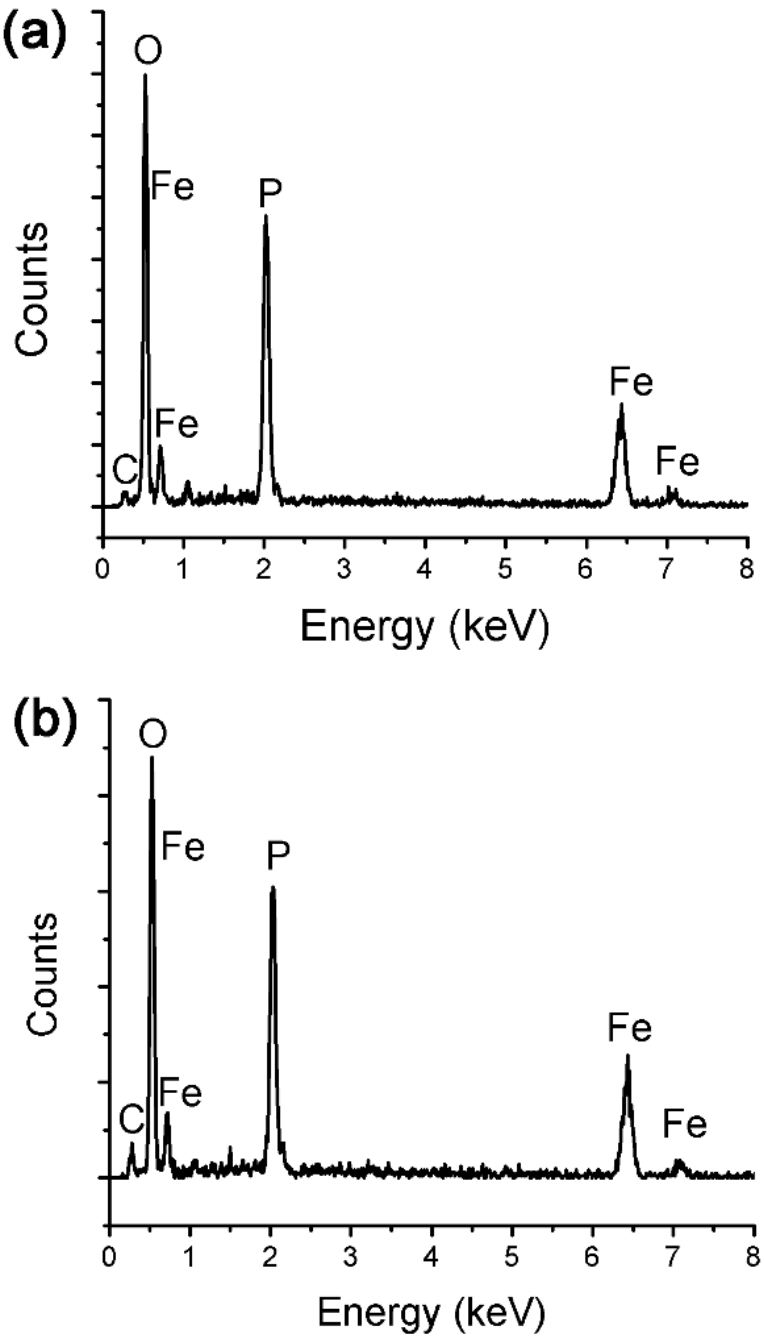

Figure 2.13. EDX spectra of $FePO_4$-coated peptide amphiphile molecules. (a) calcined E-PA/$FePO_4$, (b) calcined Phos-PA/$FePO_4$.

TEM was also used to visualize the morphology of templated $FePO_4$ at nanoscale dimensions. The non-calcined and calcined $FePO_4$ from two different peptide templates have significant difference (Figure 2.14). Non-calcined Phos-PA/$FePO_4$ forms double layer nanofiber with inorganic $FePO_4$ on the surface of peptide nanofiber core. The formation of nanofibers is expected since self-assembled Phos-PA forms nanofiber under the effect of either acidic or inorganic metal solution. The attached iron ions on the surface of nanofiber provide the nucleation sites for the growth of inorganic materials. In addition, the repeated nucleation process increases the thickness of the growth $FePO_4$. After the calcination, the organic-inorganic core-shell nanofibers are transformed into nanotubes due to the removal of organic core template. The average of the wall thickness of $FePO_4$ nanotubes after calcination is around 8 nm (Figures 2.14b, d, and e).

On the other hand, E-PA/$FePO_4$ shows the condition in which the inorganic material covers the 1-D peptide nanobelts. The peptide nanobelts are formed after the addition of $FeCl_3$ to E-PA. Immersing the self-assembled E-PA/$FeCl_3$ into phosphate solution makes the nucleation process occurred on the site where Fe^{3+} cations interact with the peptide. The surface of peptide nanobelts is covered by $FePO_4$ after some repeated procedure. There is some small amount of nanotubes observed within the nanobelts. It may come since E-PA also forms nanofibers when it self-assembles under acidic pH condition. In addition, the pH of $FeCl_3$ is also quietly acidic. After calcination of E-PA/$FePO_4$, the regular form of nanobelt starts to sinter (Figures 2.14a, and c). The template-free $FePO_4$ was also visualized by using TEM and a bulk structure of inorganic material was observed (Figure 2.14e).

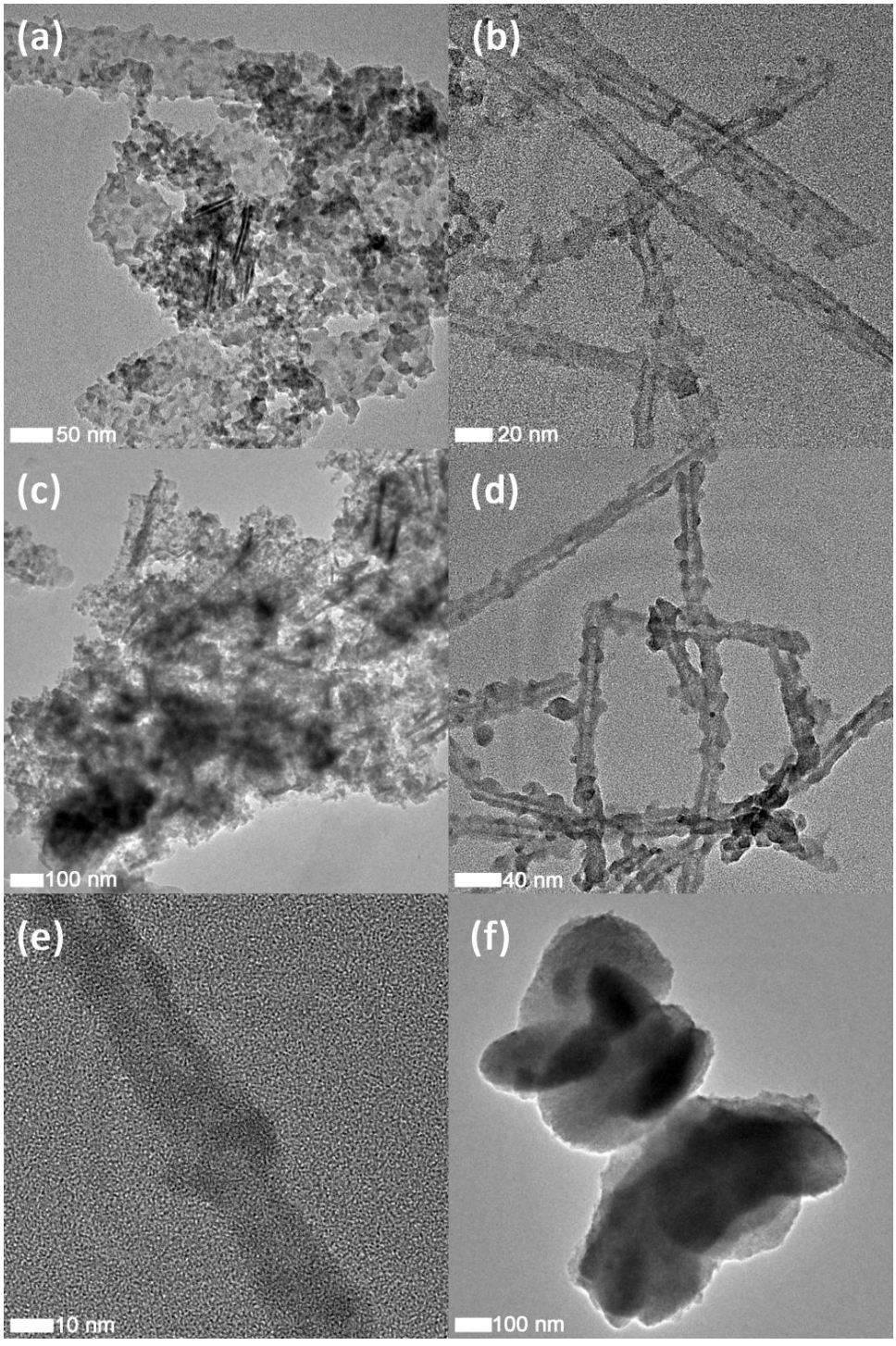

Figure 2.14. STEM images of non-calcined and calcined $FePO_4$ hybrid materials. (a) TEM image of non-calcined E-PA/$FePO_4$, (b) TEM images of non-calcined Phos-PA/$FePO_4$, (c) TEM image of calcined E-PA/$FePO_4$ at 350 °C for 1 h, (d) TEM images of calcined Phos-PA/$FePO_4$, (e) higher magnification of calcined Phos-PA/$FePO_4$, and (f) template-free $FePO_4$.

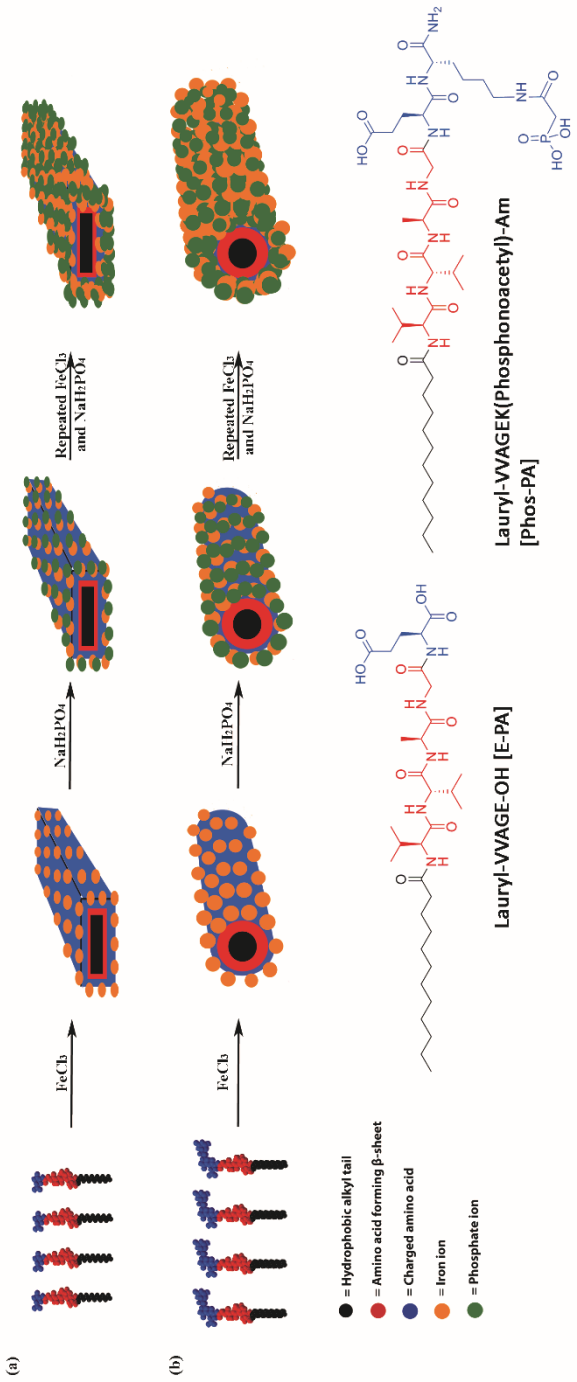

Figure 2.15. Schematic illustration of organic-inorganic core-shell templated $FePO_4$ formation. (a) Phos-PA, and (b) E-PA. Black color indicates hydrophobic alkyl tails, red color indicates β-sheet forming short peptide sequence, blue color indicates charged head, orange dot indicates iron ion, green dot indicates phosphate ion.

Qualitative analysis was performed by using FTIR to determine the interactions present in the organic-inorganic core-shell materials (Figure 2.16). Five samples that are non-calcined E-PA/$FePO_4$, non-calcined Phos-PA/$FePO_4$, calcined E-PA/$FePO_4$, calcined Phos-PA/$FePO_4$, and template-free $FePO_4$ show some peaks which belong to peptide and iron phosphate. A wide region of peak at 3400 cm^{-1} is observed in each sample that indicated to the vibration of hydroxyl group of water [103].

For non-calcined samples of E-PA/$FePO_4$ and Phos-PA/$FePO_4$, the FT-IR spectra display amide A at 3284 cm^{-1} that is associated with the –NH stretching frequency [80]. The amide I peak of both non-calcined samples is shown also at 1628 cm^{-1}, which indicates the presence of secondary structure of β-sheet [104-106]. All of this information support the result data from CD analysis that secondary structure of β-sheet is found in the templated materials. Other peaks which belong to peptide, such as asymmetric stretching of methylene hydrocarbon (2925 cm^{-1}), symmetric stretching of methylene hydrocarbon (2853 cm^{-1}), and amide II (1546 cm^{-1}) are easily detected from non-calcined E-PA/$FePO_4$ and Phos-PA/$FePO_4$ [107].

However, all of the peaks that belong to the organic core are difficult to be observed in calcined samples due to the absence of organic materials after being treated at moderately high temperature (350 °C). The electrostatic interaction between the functional group of the peptide and inorganic material can be analyzed from the spectral bands that are mainly distributed over two wavenumber ranges from 460-650 cm^{-1} and 940-1120 cm^{-1} which are ascribed to the internal stretching, internal bending and external oscillation modes of O-P-O and Fe-O-P band, respectively [108-111]. The peak that is observed around 2350 cm^{-1} also corresponds to the P-O stretching mode [112]. By comparing the Fe-O-P peaks of non-calcined and calcined samples, the Fe-O-P peak of calcined samples shifted to higher wavenumber compared to the non-calcined samples indicating the shorter Fe-O-P chemical bond length of calcined samples than non-calcined samples due to sintering process.

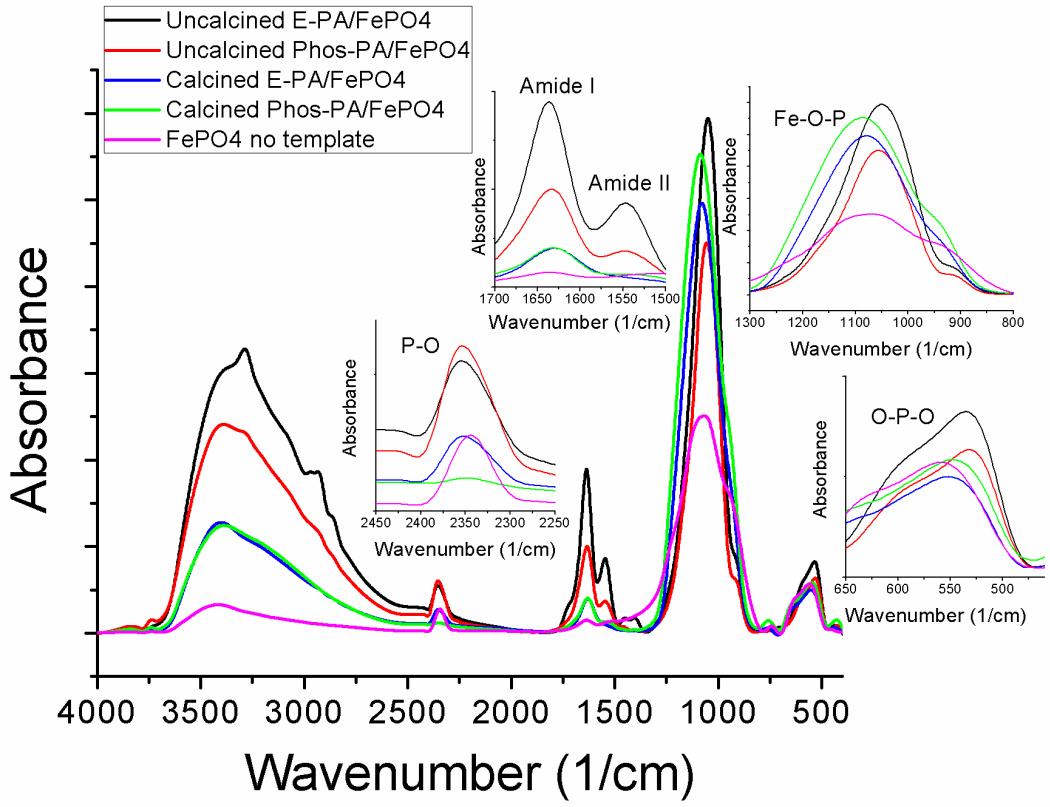

Figure 2.16. FT-IR spectra of the $FePO_4$ samples. Black color is assigned to non-calcined Phos-PA/$FePO_4$, red color for calcined Phos-PA/$FePO_4$, blue color for non-calcined E-PA/$FePO_4$, green color for calcined E-PA/$FePO_4$, and pink color for template-free $FePO_4$.

A thermogravimetric analysis was performed to determine the quantity of organic and inorganic composition of non-calcined E-PA/$FePO_4$ and Phos-PA/$FePO_4$ (Figure 2.17). Below 150 °C, these as-synthesized $FePO_4$ samples loss their first weight about 15.4% E-PA/$FePO_4$ and 17.6% for Phos-PA/$FePO_4$ due to the release of adsorbed water from the surface of samples. In between 150 °C to 350 °C, the samples loss again their weight due to the elimination of crystal water [113]. After 500 °C, N_2 gas was switched with O_2 gas aimed at degrading the organic residues. The results reveal that both of the template-directed $FePO_4$ materials before calcinations consist of nearly 65% of inorganic contents for both of the materials. There is also slightly increment in weight for both of the materials after 650 °C that might come from the instrumental performance.

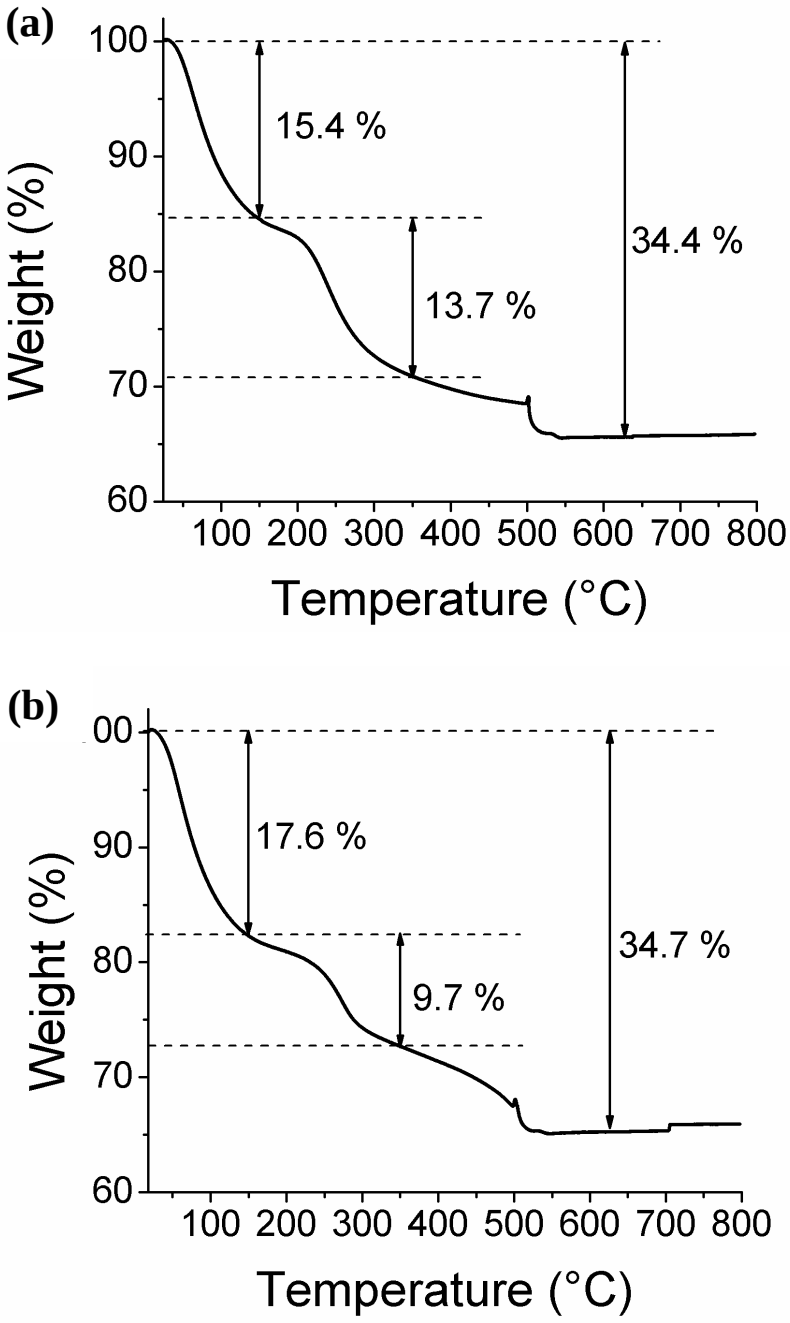

Figure 2.17. TGA of organic inorganic core-shell composite structure. (a) Non-calcined E-PA/$FePO_4$, and (b) non-calcined Phos-PA/$FePO_4$.

Crystallinity of the organic-inorganic core-shell materials were analyzed using X-ray diffractometer (XRD). A broad peak was observed for each sample: non-calcined E-PA/$FePO_4$, non-calcined Phos-PA/$FePO_4$, calcined E-PA/$FePO_4$, and calcined Phos-PA/ $FePO_4$ (Figure 2.18a). These results explain that the

templated samples are completely in amorphous phase. On the other hand, amorphous structure is not observed for template-free $FePO_4$, instead crystal structure is observed in this sample that may come from the hydrolysis of Fe^{3+} ions leading to undesired products (Figure 2.18b). The peptide templates are useful to suppress the hydrolysis of Fe^{3+} ions into oxide/hydroxide by electrostatically attracting the Fe^{3+} cations to form well arranged $FePO_4$ nucleation sites [58]. Heating the samples until 350 °C still preserved the amorphous structure of $FePO_4$ that is better in electrochemical activity than in the crystalline specimen [9].

The purity of the crystalline $FePO_4$ was proved by heating both as-synthesized E-PA/$FePO_4$ and Phos-PA/FePO4 until 600 °C for 2 h to form crystaline $FePO_4$. The peaks of crystalline structure of $FePO_4$ according to the reference from ICSD hexagonal $FePO_4$ code 01-084-0875 are observed from the samples (Figure 2.19) [114]. The asterisked peaks in both of the templated samples show an additional unidentified phase(s) co-existing along with the hexagonal $FePO_4$ type phase [115].

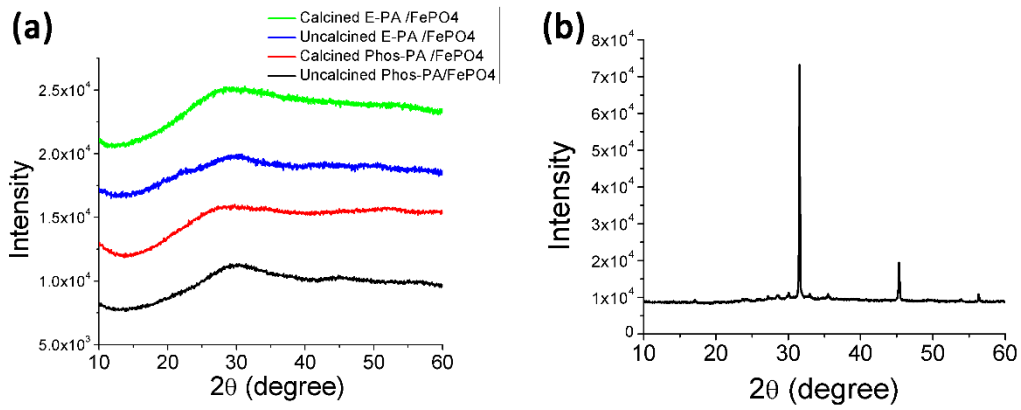

Figure 2.18. XRD patterns of organic-inorganic core-shell composite structures and template-free $FePO_4$. (a) Templated $FePO_4$ (Green shows calcined E-PA/$FePO_4$, blue shows non-calcined E-PA/$FePO_4$, red shows calcined Phos-PA/$FePO_4$, and black shows non-calcined Phos-PA/$FePO_4$), and (b) template-free $FePO_4$.

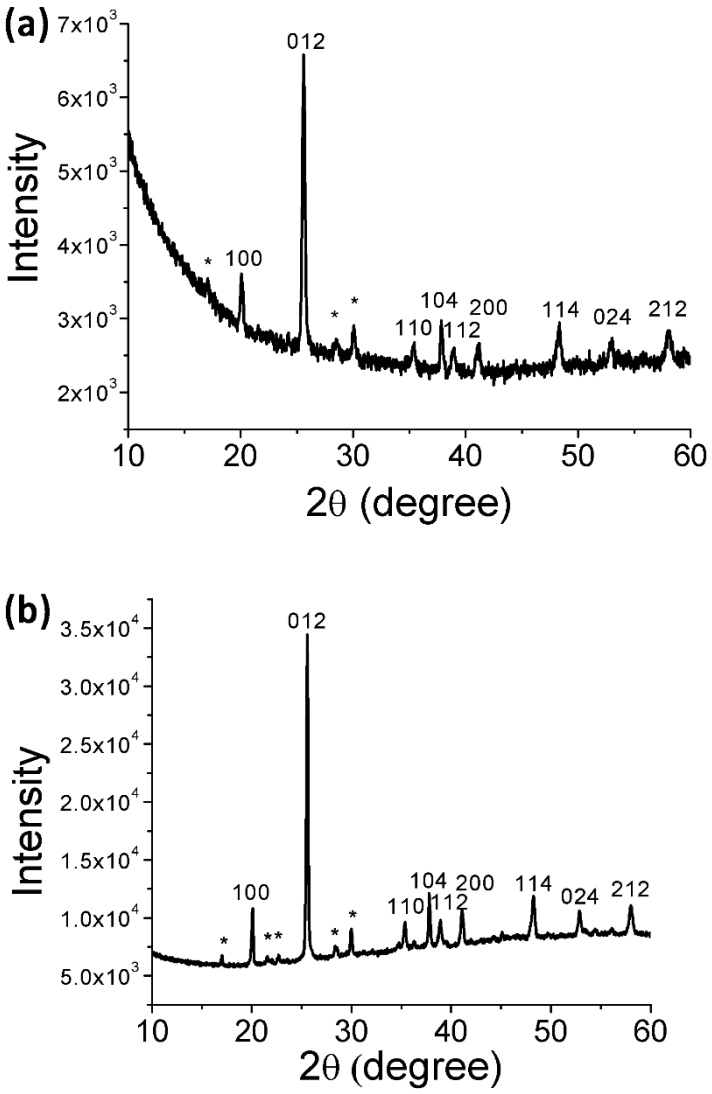

Figure 2.19. XRD pattern of calcined organic-inorganic core-shell composite structure at 600 °C for 2 h. (a) E-PA/$FePO_4$, and (b) Phos-PA/$FePO_4$.

X-ray photoelectron spectroscopy was used to determine the valence and electronic state of organic/inorganic molecules and also characterize organic-inorganic core-shell materials of templated $FePO_4$. XPS survey spectra from non-calcined and calcined $FePO_4$ samples show peaks corresponding to Fe 2p, Fe 3p, O 1s, N 1s, C 1s, P 2s, and P 2p (Figure 2.20). Here the N peaks that are easily observed for the non-calcined samples belong to the peptide. Altough calcination is carried out to remove the peptide, minor N peaks still can be observed around 400 eV for calcined samples due to the adsorption of nitrogen gas on the sample surface.

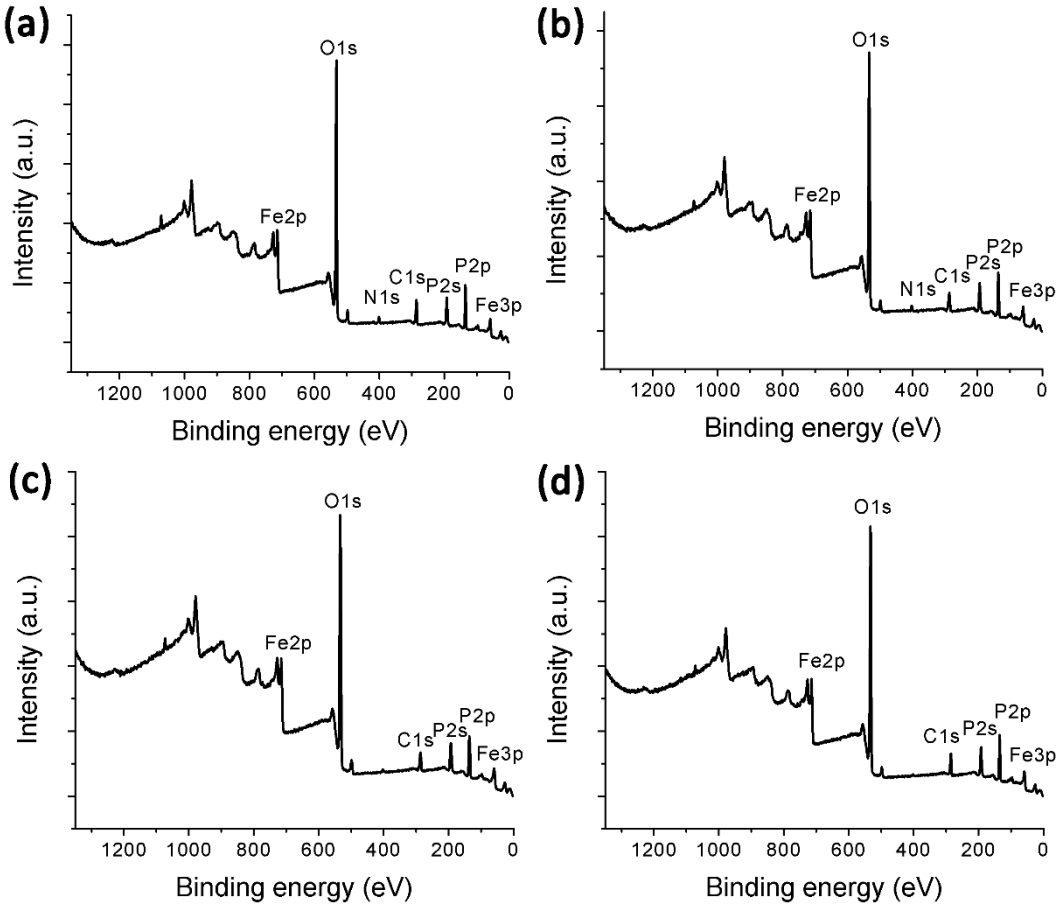

Figure 2.20. XPS spectra survey profile of organic-inorganic core-shell materials. (a) Non-calcined E-PA/$FePO_4$, (b) non-calcined Phos-PA/$FePO_4$, (c) calcined E-PA/$FePO_4$, and (d) calcined Phos-PA/$FePO_4$.

The core-scan spectra of Fe 2p, C 1s, P 2p, and O 1s profiles of calcined E-PA/$FePO_4$ and Phos-PA/$FePO_4$ are shown in the Figures 2.21 and 2.22, respectively. In the Figure 2.21, the Fe 2p spectrum splits into main peak ($2p_{3/2}$) and corresponding satellite peak ($2p_{1/2}$) at 716.4 eV and 730.1 eV, respectively due to partially filled d-orbits of the transition metal ions [116]. The binding energy of Fe $2p_{3/2}$ at 716.4 eV is the characteristic peak of Fe(III) [117]. The binding energy of Fe(III) is shifted to higher value than reported one (711.4 eV) due to neighboring atoms [102]. These interatomic effects are provided by the attachment of carbonyl ligand. It forms the highly antiscreened iron with higher binding energy [118]. There is not any presence of Fe(II) in the sample since the peak corresponding to Fe(II) at 708.2 eV is not observed [119]. The C1s peak can be deconvoluted into

three different components at 284.8 eV, 286.1 eV, and 288.8 eV that are attributed to C-C, C-N, and N-C=O/O-C=O, respectively [120]. These peaks belong to the left peptide. The P 2p spectrum can also be deconvoluted into two components of $2p_{3/2}$at 133.9 eV and $2p_{1/2}$ at 134.9 eV due to spin-orbit coupling. This information revealed the existence of PO_4^{3-} tetrahedral group in the samples and also the absence of impurity phases such as Fe_2P or Fe_2O_3 with binding energy of 129.5 eV [116]. Meanwhile, the O 1s spectrum has three components. O1 at 531.8 eV are assigned to the oxide ions of PO_4^{3-} group together with peak of P $2p_{3/2}$ at 133.9 eV [121-123]. The O2 and O3 peaks at 533.7 eV and 535.0 eV result from the chemisorbed –OH groups of the $FePO_4$ with the organic oxygen of the peptide and physisorbed H_2O, respectively [120].

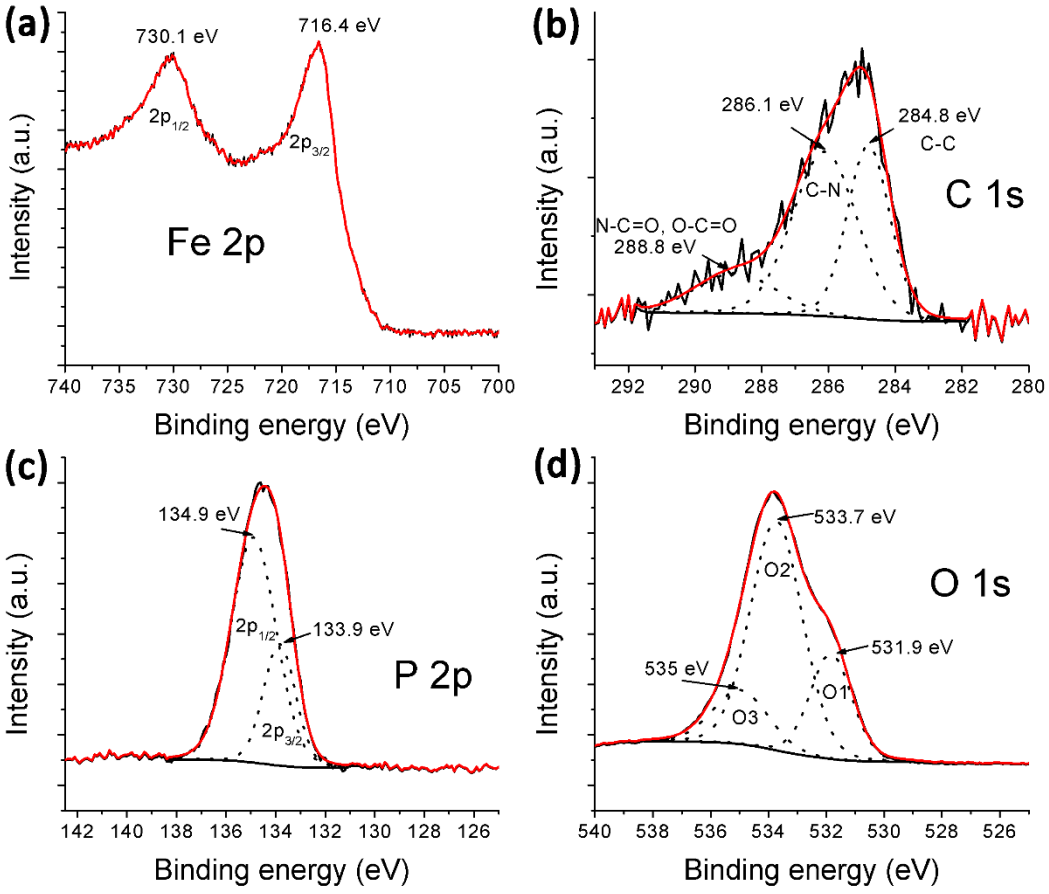

Figure 2.21. XPS spectra core scan of calcined E-PA/$FePO_4$. (a) Fe 2p, (b) C 1s, (c) P 2p, and (d) O 1s.

Calcined Phos-PA/$FePO_4$ has also core-scan spectra similar to that of the calcined E-PA/$FePO_4$ (Figure 2.22). The splitted Fe 2p consists of the main peak ($2p_{3/2}$) at 715.2 eV and corresponding satellite peak ($2p_{1/2}$) at 728.5 eV. The C 1s peak is constructed from C-C, C-N, and N-C=O/O-C=O at 284.8 eV, 286.4 eV, and 288.5 eV, respectively. The phosphate group (PO_4^{3-}) can be analyzed based on the P 2p spectrum that consisted of $2p_{3/2}$ peak at 134.0 eV and $2p_{1/2}$ peak at 135.2 eV. Lastly, the O1, O2, and O3 peaks from O 1s spectrum indicate the presence of oxide oxygen of PO_4^{3-}, chemisorbed hydroxyl group of the $FePO_4$ with the organic oxygen of the peptide, and physisorbed H_2O at 531.8 eV, 533.9 eV, and 536.3 eV, respectively.

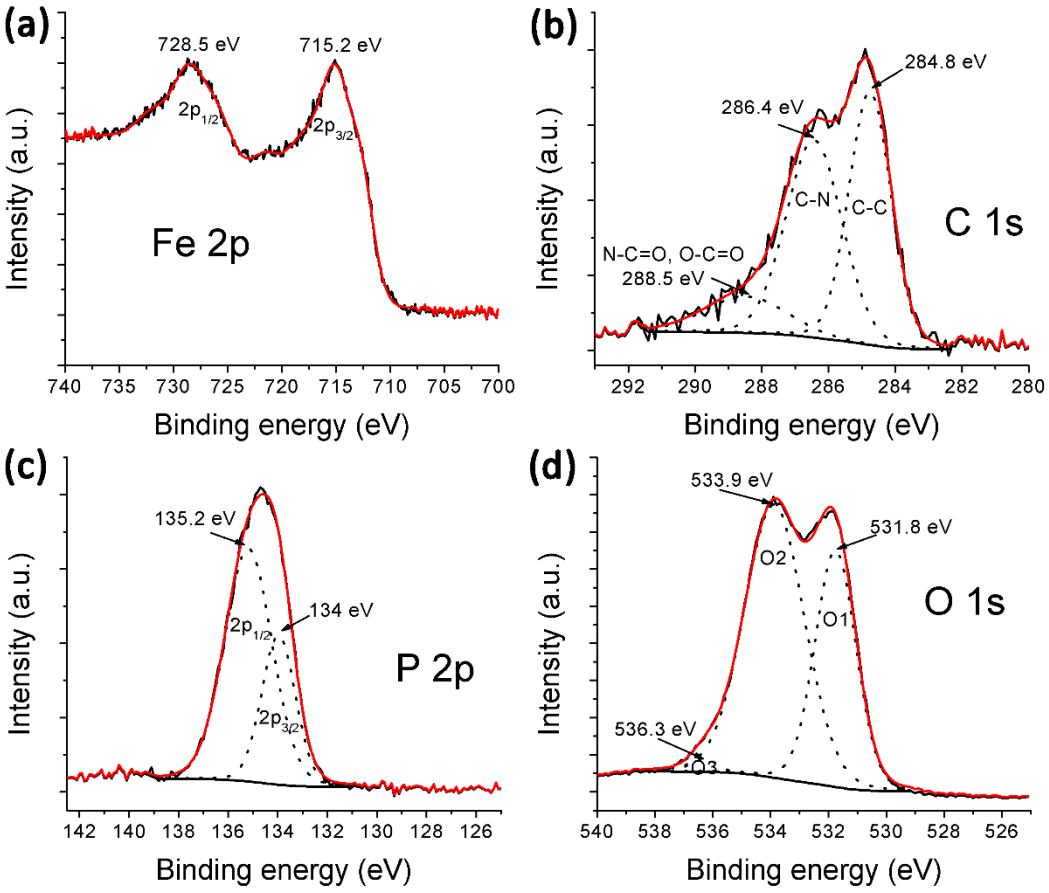

Figure 2.22. XPS spectra core scan of calcined Phos-PA/$FePO_4$. (a) Fe 2p, (b) C 1s, (c) P 2p, and (d) O 1s.

ICP-MS analyses were also conducted to determine the amount of $FePO_4$ in each calcined sample (Appendix 3). Five gradually increasing concentrations of iron standard solutions were used to construct the calibration line that was important to predict the amount of iron in the samples. According to the ICP-MS results, 1 mg of calcined E-PA/$FePO_4$, Phos-PA/$FePO_4$, and template-free $FePO_4$ contains 0.2984 mg, 0.2496 mg, and 0.2647 mg of iron, respectively. The one to one ratio between iron and phosphor simplifies the calculations to obtain the percentage of $FePO_4$ in the sample powders. The weight percentages of iron phosphate in 1 mg of each of of the calcined E-PA/$FePO_4$, Phos-PA/$FePO_4$, and template-free $FePO_4$ are found to be 80.65%, 67.46%, and 71.54%. These percentages of $FePO_4$ in each calcined powder are used as the information for calculating the weight of active material in the cathode material in order to obtain the exact value of the capacity.

Calcined E-PA/$FePO_4$, calcined Phos-PA/$FePO_4$, and template-free $FePO_4$ were chosen as the cathode materials for lithium-ion batteries. The physical property of the nanostructured materials change because of the quantum mechanical effects due to the decreasing diameter of the material structure after passing some certain characteristic length [124, 125]. Calcined Phos-PA/$FePO_4$ is expected to have good electrochemical performance due to the amorphous structure and ultra-fine 1-D nanostructure (nanotube) with the inner diameter of 10 nm and wall thickness of 8 nm. Due to large surface-to-volume ratio and two-dimensional confinement, 1-D nanostructure shows greater chemical reactivity that is different from its corresponding bulk counterpart [126]. In addition, the nanotube also enhances the diffusion of lithium ion due to shorter path length leading to better rate capability [8].

Although the iron phosphate nanostructure can enhance the electrochemical performances lithium-ion batteries compared to the bulk iron phosphate, the electronic conductivity of the nanostructured material is still poor [8]. Addition of multi-walled carbon nanotube (MWCT) as an additive material to iron phosphate offers more facile electronic transport channels. It also made the electrode materials to be stable during charge/discharge cycling (Figure 2.23) [33, 34].

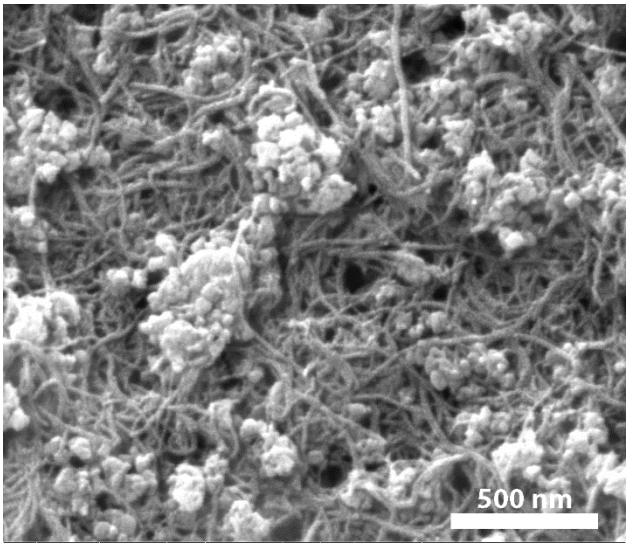

Figure 2.23. The morphology of electrode film of Phos-PA/$FePO_4$ and MWCT.

In this study, lithium-ion battery cells in which the cathode materials were prepared by the mixing of the templated iron phosphate materials with MWCT were tested using multichannel battery testing system. Template-free $FePO_4$ was also employed as a control sample. The charge-discharge profiles of the $FePO_4$ were provided with the current rates of C/20, C/10, C/5, C, 2C, and C/20, where C represented the current rate at which the theoretical capacity (~178 mAh/g) was charged/discharged in 1 h. The voltage limits for this system was 2.0-4.0 V. Although the material could not yield a capacity close to its theoretical value at the lowest current rate (C/20), the capacity of the material was rather stable. The high charge capacity obtained in first cycle could be related to the SEI (solid-electrolyte interface) formation and water electrolysis.

The cathode material of E-PA/$FePO_4$ nanobelt shows the discharge capacity of 125 mAh/g at C/20 current rate (Figure 2.24). The capacity decreases to 110 mAh/g and 80 mAh/g when the current rate is increased to C/10 and C/5, respectively. Increasing the current rate to C makes the capacity of the battery dropping to 17 mAh/g. The capacity value at 2C is negligible as the material characteristically has a poor rate capability. The capacity of the E-PA/$FePO_4$ nanobelt is recovered to 140 mAh/g when the current rate is brought back to C/20. It explains the electrochemical reversibility of the E-PA/$FePO_4$ nanobelt [127].

This latter capacity value was higher than the capacity at first C/20 cycles that might be affected from the lately activated region of $FePO_4$ electrode.

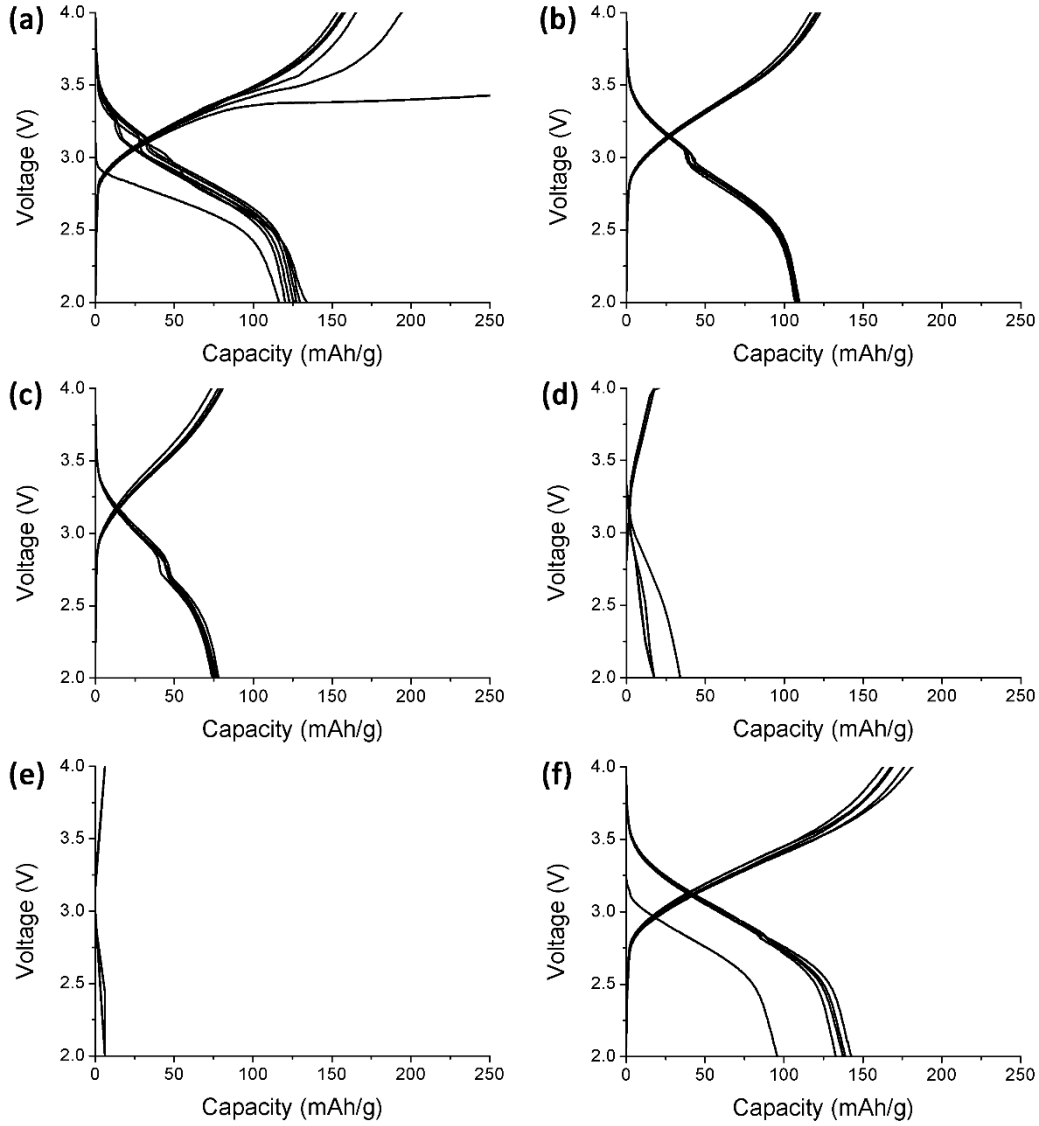

Figure 2.24. Charge and discharge curves (5-7 cycles) of E-PA/$FePO_4$ nanobelt as a cathode of Li-ion batteries at different current rate. (a) First C/20, (b) C/10, (c) C/5, (d) C, (e) 2C, (f) last C/20.

The discharge capacity of Phos-PA/$FePO_4$ nanotube was not significantly different from E-PA/$FePO_4$ nanobelt (Figure 2.25). At the lowest current rate, C/20, the discharge capacity of Phos-PA/$FePO_4$ nanotube is lower than that of E-PA/$FePO_4$ nanobelt that is around 110 mAh/g. However, the capacity increase to

120 mAh/g when the current rate is increased to C/10. By continuing to increase the current rate to C/5 and C, the dicharge capacity decrease to 90 mAh/g and 25 mAh/g, respectively. The capacity at higher current rate of 2C is negligible due to poor rate capability insulator. The capacity of the Phos-PA/$FePO_4$ nanotube is recovered to 130 mAh/g when the current rate is brought back to C/20 active.

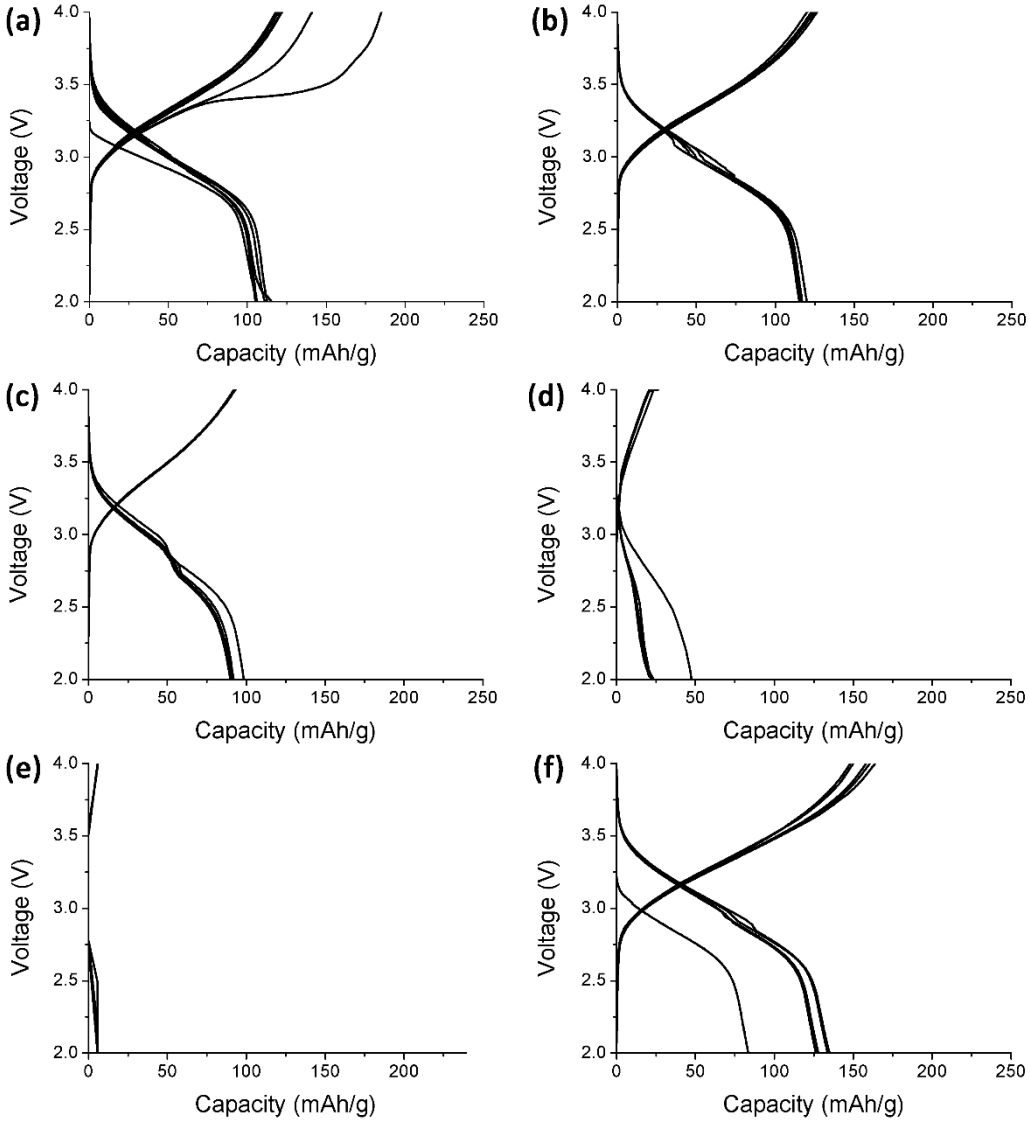

Figure 2.25. Charge and discharge curves (5-7 cycles) of Phos-PA/$FePO_4$ nanotube as a cathode of Li-ion batteries at different current rate. (a) First C/20, (b) C/10, (c) C/5, (d) C, (e) 2C, (f) last C/20.

According to these results, E-PA/$FePO_4$ nanobelt provides higher discharge capacity than Phos-PA/$FePO_4$ nanotube at C/20 (Figure 2.26a). By increasing the number of cycles at C/20, the discharge capacity of Phos-PA/$FePO_4$ nanotube gradually increases but still behind the nanobelt result (Figure 2.26b). However, Phos-PA/$FePO_4$ nanotube gives higher discharge capacity than Phos-PA/$FePO_4$ nanobelt at higher current rate. Inconsistent results of $FePO_4$ discharge capacities at lower current rate for both of the nanostructures indicates the amorphous structure of the electrode materials. Figure 2.26c shows the cycling performance of E-PA/$FePO_4$ nanobelt and Phos-PA/$FePO_4$ nanotube at current rate of C/2 for 12 cycles. The discharge capacity of $FePO_4$ nanotube is unstable during the first five cycles that later become stable at 95 mAh/g. On the other hand, $FePO_4$ nanobelt showed lower discharge capacity values of 80 mAh/g.

Although the initial discharge capacity of the Phos-PA/$FePO_4$ nanotube is lower than that of the E-PA/$FePO_4$ nanobelt, Phos-PA/$FePO_4$ nanotube gives comparable capacity at the end of the capacity stability test and shows better capacity at higher current rates. Better performance of the Phos-PA/$FePO_4$ nanotube compared to the E-PA/$FePO_4$ nanobelt is caused by the higher surface to volume ratio of nanotube structure. The nanotube structure enhances the diffusion of lithium ion due to shorter path length leading to better rate capability. In addition, the phosphate group at the periphery of Phos-PA plays important role as the nucleation site for the formation of $FePO_4$.

Peptide amphiphile molecules also play the role as the template for fabrication of $FePO_4$ although the final product capacity does not reach theoretical capacity value of $FePO_4$. On the other hand, the template-free $FePO_4$ exhibits poor discharge capacity around 25 mAh/g at current rate of C/10.

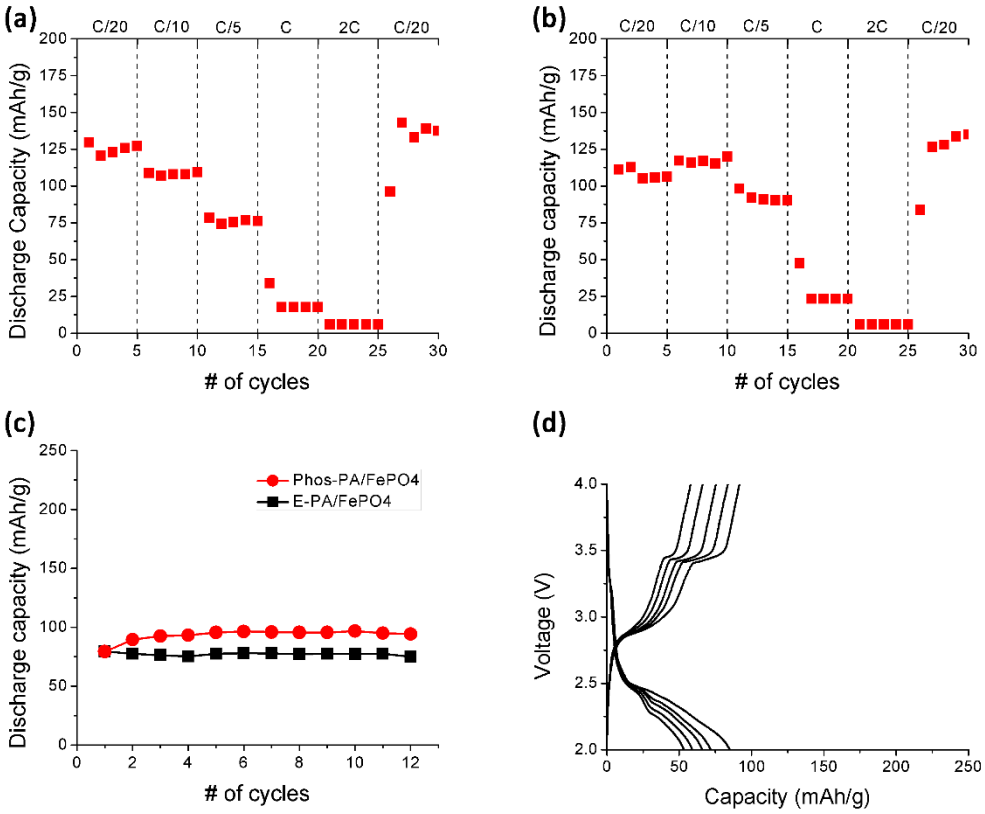

Figure 2.26. Discharge capacities of E-PA/$FePO_4$ nanobelt, Phos-PA/$FePO_4$ nanotube, and template-free $FePO_4$. (a) Rate capability of E-PA/$FePO_4$ nanobelt, (b) rate capability of Phos-PA/$FePO_4$ nanotube, (c) cycling performance at current rate of C/2, and (d) charge-discharge curve of template-free $FePO_4$ at C/10.

CHAPTER 3

CONCLUSION

3. CONCLUSION

The iron phosphate materials can be constructed by employing peptide amphiphile molecules as the templates. Two different peptide amphiphile molecules, which were E-PA (C12-VVAGE-OH) and Phos-PA (C12-VVAGEK(Phosphonoacetyl)-NH_2) were synthesized by using solid phase peptide synthesis (SPPS) method. Both of the peptide amphiphile molecules triggered by Fe^{3+} ions self-assemble to form β-sheet structural motif contributing to the nanofiber and nanobelt formation. In addition, iron ions that induce the self-assembly process by attaching to the periphery of the peptide electrostatically also act as the nucleation sites for the growth of $FePO_4$.

The preparation of templated $FePO_4$ was started by dropping the $FeCl_3$ solution into the peptide solution in order to induce the self-assembly of the peptide. The peptides self-assemble to form nanostructures that later being entangled to form a network due to the noncovalent interactions. A hydrogel was observed as the result of the self-assembly process. The hydrogels were subsequently immersed into a batch that contained cold $FeCl_3$ solution followed by transferring it to NaH_2PO_4 in order to start the nucleation of inorganic iron phosphate on the organic peptide template. The growth of the inorganic layer was maintained by repeating for some cycles. The hydrogel that was easily evaporated outside of the solution was then treated using CPD aimed at changing the physical form of a hydrogel into a dry peptide network of the gel. Later, the heat treatment (calcination) was performed in order to obtain inorganic $FePO_4$ materials by removing the organic peptide template. The calcination temperature is brought to 350 °C to obtain amorphous forms of anhydrous $FePO_4$ that has better capacity and cyclability than trigonal, hexagonal and hydrated $FePO_4$

Some analyses were performed to support the identification of the fabricated materials, such as LC-MS, CD, E-SEM/EDX, TEM, FT-IR, TGA, XRD, XPS, and ICP-MS. The LC-MS results informed the purity and the molecular weight of the peptide amphiphile molecules. Both of the peptide amphiphile molecules have the purity greater than 95% with the molar weight of 655 g/mol for E-PA and 904 g/mol for Phos-PA.

The CD results show the formation of β-sheet structure for all of the self-assembled samples. The presence of β-sheet structural motif indicates the self-assembly process in the solution. In addition, the presence of β-sheet signal for Phos-PA supports the fact that Phos-PA forms hydrogel after a few minutes of waiting. The different type of signal is only observed for E-PA solution at physiological pH that shows the formation of a random coil structural motif. This random coil structure of E-PA disappears and transforms to β-sheet structure either by lowering the pH or introducing the iron ions indicating the self-assembly of the peptide. The negatively charged functional groups of the peptide amphiphile molecules were able to attract the Fe^{3+} ions and protons that screen the negative charge of the peptides.

The scanning electron micrographs of the calcined and non-calcined $FePO_4$ coated peptide amphiphile samples show the network structure that are thoroughly preserved even after calcination at moderately high temperature. The EDX spectra of the calcined $FePO_4$ coated peptide amphiphile samples confirm the deposition of iron phosphate on the peptide networks as the Fe, P and O peaks are observed in EDX spectrum of both samples. The atomic ratios of Fe/P for calcined E-PA/$FePO_4$ and calcined Phos-PA/$FePO_4$ are found to be 0.92 and 0.99, respectively, that were close to one.

The negative-stained transmission electron micrographs of both self-assembled E-PA and Phos-PA at acidic pH show the presence of 1-D nanofibers with average of 10 nm diameters. However, when $FeCl_3$ was used to induce the self-assembly of the peptide solution, the self-assembled E-PA and Phos-PA formed different types of nanostructures. STEM image of E-PA/$FeCl_3$ shows the formation of 1-D nanobelts with the width of 60 nm. On the other hand, nanofibers with diameter of 10 nm are observed in the STEM image of Phos-PA/$FeCl_3$. The morphology of the samples after the formation of $FePO_4$ layer on the peptide cores resembles the structure of iron-induced peptide self-assembly. Non-calcined Phos-PA/$FePO_4$ forms double layer 1-D nanofibers with inorganic $FePO_4$ on the surface of peptide nanofiber core. After the calcination, the organic-inorganic core-shell nanofibers are transformed into nanotubes due to the removal of organic core template with the average of the wall thickness of 8 nm. E-PA/$FePO_4$ shows the

inorganic material covered the 1-D peptide nanobelts. After calcination of E-PA/$FePO_4$, the regular form of nanobelt starts to sinter.

The FT-IR spectra show some peptide peaks that are only observed in non-calcined samples, such as –NH stretching, amide I, asymmetric stretching of methylene hydrocarbon, and amide II. The amide I peak indicates the presence of secondary structure of β-sheet supporting the resulted data from CD analysis. In general, the Fe-O-P, O-P, and O-P-O peaks are observed in all analyzed samples.

The quantities of inorganic content of the non-calcined (as-synthesized) samples were determined by using TGA. The results revealed that both of the as-synthesized samples consist of nearly 65% of inorganic materials.

The XRD spectra of calcinated $FePO_4$ coated peptide amphiphile samples exhibit a wide peak indicating the amorphous phase in the samples. On the other hand, template-free $FePO_4$ shows some narrow peaks explaining the presence of crystal structure that may come from the hydrolysis of Fe^{3+} leading to undesirable products. The amorphous $FePO_4$ exhibits better electrochemical activity than the crystalline $FePO_4$ materials. XRD was also used to determine the purity of the templated $FePO_4$ materials that had been heated until 600 °C for 2 h to form crystalline structure. The peaks of hexagonal $FePO_4$ are observed from the templated samples.

XPS was used to determine the valence and electronic state of organic/inorganic molecules and also the characterization of organic-inorganic core-shell materials of templated $FePO_4$. The wide-scan spectra of templated-$FePO_4$ samples show peaks that correspond to Fe 2p, Fe 3p, O 1s, N 1s, C 1s, P 2s, and P 2p. In addition, the high-resolution spectra of Fe 2p, C 1s, P 2p, and O 1s profiles from calcined E-PA/$FePO_4$ and Phos-PA/$FePO_4$ samples also support the information about the presence of $FePO_4$ and peptide in the samples.

The amount of the active material ($FePO_4$) in the calcined samples were calculated from the ICP-MS results. The exact amount of $FePO_4$ inside the calcined powders is important in order to calculate the capacity of the calcined samples. According to the results, the weight percentages of iron phosphate in 1 mg of each of the calcined E-PA/$FePO_4$, Phos-PA/$FePO_4$, and template-free $FePO_4$ are found to be 80.65%, 67.46%, and 71.54%.

The charge-discharge profiles of the $FePO_4$ samples are provided with the current rates of C/20, C/10, C/5, C, 2C, and C/20. The voltage limits for this system was 2.0-4.0 V. The high charge capacity obtained in first cycle could be related to the SEI (solid-electrolyte interface) formation and water electrolysis. As the current rate is increased, the discharge capacity of Phos-PA/$FePO_4$ nanotube become higher than the discharge capacity of E-PA/$FePO_4$. The Phos-PA/$FePO_4$ nanotube and E-PA/$FePO_4$ nanobelt materials exhibit discharge capacity of 120 and 110 mAh/g, respectively, at current rate of C/10. Although these values are still far from theoretical capacity value of 178 mAh/g, the capacities of the materials are rather stable. In here, the peptide amphiphile molecules play the role as the template for fabricating $FePO_4$ as the template-free $FePO_4$ exhibits poor discharge capacity around 25 mAh/g at current rate of C/10.

The cycling performance of Phos-PA/$FePO_4$ nanotubes and E-PA/$FePO_4$ nanobelts at current rate of C/2 for 12 cycles shows the discharge capacity of 95 and 80 mAh/g, respectively. Although the initial discharge capacity of the Phos-PA/$FePO_4$ nanotube is lower than that of the E-PA/$FePO_4$ nanobelt, Phos-PA/$FePO_4$ nanotube gives higher capacity at the end of the capacity stability test.

Thus, regarding all of the aspect, the $FePO_4$ nanotubes have better electrochemical performance than $FePO_4$ nanobelts. Better performance of the Phos-PA/$FePO_4$ nanotubes compared to E-PA/$FePO_4$ nanobelts is caused by the higher surface to volume ratio of the structure and the presence of phosphate group at the periphery of Phos-PA. In addition, the nanotubes also enhance the diffusion of lithium ion due to shorter path length leading to better rate capability.

BIBLIOGRAPHY

1. M. S. Whittingham, "Lithium batteries and cathode materials," *Chemical Reviews*, vol. 104, no. 10, pp. 4271-4302, 2004. doi: 10.1021/cr020731c.
2. J. M. Tarascon and M. Armand, "Issues and challenges facing rechargeable lithium batteries," *Nature*, vol. 414, no. 6861, pp. 359-367, 2001.
3. D. Linden and T. B. Reddy, *Handbook of batteries*. McGraw-Hill, 2002
4. F. Cheng, Z. Tao, J. Liang, and J. Chen, "Template-directed materials for rechargeable lithium-ion batteries," *Chemistry of Materials*, vol. 20, no. 3, pp. 667-681, 2008. doi: 10.1021/cm702091q.
5. M. Winter, J. O. Besenhard, M. E. Spahr, and P. Novák, "Insertion electrode materials for rechargeable lithium batteries," *Advanced Materials*, vol. 10, no. 10, pp. 725-763, 1998. doi: 10.1002/(sici)1521-4095(199807)10:10<725::aid-adma725>3.0.co;2-z.
6. A. K. Padhi, K. S. Nanjundaswamy, and J. B. Goodenough, "Phospho-olivines as positive-electrode materials for rechargeable lithium batteries," *Journal of The Electrochemical Society*, vol. 144, no. 4, pp. 1188-1194, 1997. doi: 10.1149/1.1837571.
7. S.-Y. Chung, J. T. Bloking, and Y.-M. Chiang, "Electronically conductive phospho-olivines as lithium storage electrodes," *Nat Mater*, vol. 1, no. 2, pp. 123-128, 2002.
8. V. S. Saji, Y.-S. Kim, T.-H. Kim, J. Cho, and H.-K. Song, "One-dimensional (1D) nanostructured and nanocomposited $LiFePO_4$: Its perspective advantages for cathode materials of lithium ion batteries," *Physical Chemistry Chemical Physics*, vol. 13, no. 43, pp. 19226-19237, 2011. doi: 10.1039/c1cp22818h.
9. Y. Song, S. Yang, P. Y. Zavalij, and M. S. Whittingham, "Temperature-dependent properties of $FePO_4$ cathode materials," *Materials Research Bulletin*, vol. 37, no. 7, pp. 1249-1257, 2002. doi: 10.1016/S0025-5408(02)00771-7.
10. C. Wang and J. Hong, "Ionic/electronic conducting characteristics of $LiFePO_4$ cathode materials: The determining factors for high rate performance,"

Electrochemical and Solid-State Letters, vol. 10, no. 3, pp. A65-A69, 2007. doi: 10.1149/1.2409768.

11. S. Yang, Y. Song, P. Y. Zavalij, and M. Stanley Whittingham, "Reactivity, stability and electrochemical behavior of lithium iron phosphates," *Electrochemistry Communications*, vol. 4, no. 3, pp. 239-244, 2002. doi: 10.1016/S1388-2481(01)00298-3.
12. G. Kobayashi, S.-i. Nishimura, M.-S. Park, R. Kanno, M. Yashima, T. Ida, and A. Yamada, "Isolation of solid solution phases in size-controlled Li_xFePO_4 at room temperature," *Advanced Functional Materials*, vol. 19, no. 3, pp. 395-403, 2009. doi: 10.1002/adfm.200801522.
13. Y. Wang, Y. Wang, E. Hosono, K. Wang, and H. Zhou, "The design of a $LiFePO_4$/carbon nanocomposite with a core–shell structure and its synthesis by an in situ polymerization restriction method," *Angewandte Chemie International Edition*, vol. 47, no. 39, pp. 7461-7465, 2008. doi: 10.1002/anie.200802539.
14. P. S. Herle, B. Ellis, N. Coombs, and L. F. Nazar, "Nano-network electronic conduction in iron and nickel olivine phosphates," *Nat Mater*, vol. 3, no. 3, pp. 147-152, 2004.
15. N. Ravet, Y. Chouinard, J. F. Magnan, S. Besner, M. Gauthier, and M. Armand, "Electroactivity of natural and synthetic triphylite," *Journal of Power Sources*, vol. 97–98, no., pp. 503-507, 2001. doi: 10.1016/S0378-7753(01)00727-3.
16. J. L. Allen, T. R. Jow, and J. Wolfenstine, "Analysis of the $FePO_4$ to $LiFePO_4$ phase transition," *Journal of Solid State Electrochemistry*, vol. 12, no. 7-8, pp. 1031-1033, 2008. doi: 10.1007/s10008-007-0459-1.
17. S. M. Zhang, J. X. Zhang, S. J. Xu, X. J. Yuan, and B. C. He, "Li ion diffusivity and electrochemical properties of $FePO_4$ nanoparticles acted directly as cathode materials in lithium ion rechargeable batteries," *Electrochimica Acta*, vol. 88, no., pp. 287-293, 2013. doi: 10.1016/j.electacta.2012.10.029.
18. Y. Liu, S. Xu, S. Zhang, J. Zhang, J. Fan, and Y. Zhou, "Direct growth of $FePO_4$/reduced graphene oxide nanosheet composites for the sodium-ion

battery," *Journal of Materials Chemistry A*, vol. 3, no. 10, pp. 5501-5508, 2015. doi: 10.1039/c5ta00199d.

19. P. P. Prosini, M. Lisi, S. Scaccia, M. Carewska, F. Cardellini, and M. Pasquali, "Synthesis and characterization of amorphous hydrated $FePO_4$ and its electrode performance in lithium batteries," *Journal of The Electrochemical Society*, vol. 149, no. 3, pp. A297-A301, 2002. doi: 10.1149/1.1435359.
20. C. M. Julien, "Lithium intercalated compounds: Charge transfer and related properties," *Materials Science and Engineering: R: Reports*, vol. 40, no. 2, pp. 47-102, 2003. doi: 10.1016/S0927-796X(02)00104-3.
21. N. Nitta, F. Wu, J. T. Lee, and G. Yushin, "Li-ion battery materials: Present and future," *Materials Today*, vol. 18, no. 5, pp. 252-264, 2015. doi: 10.1016/j.mattod.2014.10.040.
22. M. Park, X. Zhang, M. Chung, G. B. Less, and A. M. Sastry, "A review of conduction phenomena in Li-ion batteries," *Journal of Power Sources*, vol. 195, no. 24, pp. 7904-7929, 2010. doi: 10.1016/j.jpowsour.2010.06.060.
23. J. Ma, C. Wang, and S. Wroblewski, "Kinetic characteristics of mixed conductive electrodes for lithium ion batteries," *Journal of Power Sources*, vol. 164, no. 2, pp. 849-856, 2007. doi: 10.1016/j.jpowsour.2006.11.024.
24. Y. Wang, H. Li, P. He, E. Hosono, and H. Zhou, "Nano active materials for lithium-ion batteries," *Nanoscale*, vol. 2, no. 8, pp. 1294-1305, 2010. doi: 10.1039/c0nr00068j.
25. Y. Wang and G. Cao, "Developments in nanostructured cathode materials for high-performance lithium-ion batteries," *Advanced Materials*, vol. 20, no. 12, pp. 2251-2269, 2008. doi: 10.1002/adma.200702242.
26. A. S. Arico, P. Bruce, B. Scrosati, J.-M. Tarascon, and W. van Schalkwijk, "Nanostructured materials for advanced energy conversion and storage devices," *Nat Mater*, vol. 4, no. 5, pp. 366-377, 2005.
27. C. K. Chan, H. Peng, G. Liu, K. McIlwrath, X. F. Zhang, R. A. Huggins, and Y. Cui, "High-performance lithium battery anodes using silicon nanowires," *Nat Nano*, vol. 3, no. 1, pp. 31-35, 2008.
28. H. Uchiyama, E. Hosono, I. Honma, H. Zhou, and H. Imai, "A nanoscale meshed electrode of single-crystalline SnO for lithium-ion rechargeable

batteries," *Electrochemistry Communications*, vol. 10, no. 1, pp. 52-55, 2008. doi: 10.1016/j.elecom.2007.10.018.

29. M. Armand, S. Besner, J. F. Magnan, N. Ravet, M. Simoneau, and A. Vallée, *Matériaux d'électrode présentant une conductivité de surface élevée*, 2000, Google Patents.
30. E. Hosono, T. Kudo, I. Honma, H. Matsuda, and H. Zhou, "Synthesis of single crystalline spinel $LiMn_2O_4$ nanowires for a lithium ion battery with high power density," *Nano Letters*, vol. 9, no. 3, pp. 1045-1051, 2009. doi: 10.1021/nl803394v.
31. G. Centi and S. Perathoner, "The role of nanostructure in improving the performance of electrodes for energy storage and conversion," *European Journal of Inorganic Chemistry*, vol. 2009, no. 26, pp. 3851-3878, 2009. doi: 10.1002/ejic.200900275.
32. J. Chen and M. S. Whittingham, "Hydrothermal synthesis of lithium iron phosphate," *Electrochemistry Communications*, vol. 8, no. 5, pp. 855-858, 2006. doi: 10.1016/j.elecom.2006.03.021.
33. Y. Liu, X. Li, H. Guo, Z. Wang, W. Peng, Y. Yang, and R. Liang, "Effect of carbon nanotube on the electrochemical performance of C-$LiFePO_4$/graphite battery," *Journal of Power Sources*, vol. 184, no. 2, pp. 522-526, 2008. doi: 10.1016/j.jpowsour.2008.03.017.
34. A. Thess, R. Lee, P. Nikolaev, H. Dai, P. Petit, J. Robert, C. Xu, Y. H. Lee, S. G. Kim, A. G. Rinzler, D. T. Colbert, G. E. Scuseria, D. Tománek, J. E. Fischer, and R. E. Smalley, "Crystalline ropes of metallic carbon nanotubes," *Science*, vol. 273, no. 5274, pp. 483-487, 1996. doi: 10.1126/science.273.5274.483.
35. H.-P. Lin and C.-Y. Mou, "Structural and morphological control of cationic surfactant-templated mesoporous silica," *Accounts of Chemical Research*, vol. 35, no. 11, pp. 927-935, 2002. doi: 10.1021/ar000074f.
36. F. Schüth, "Endo- and exotemplating to create high-aurface-area inorganic materials," *Angewandte Chemie International Edition*, vol. 42, no. 31, pp. 3604-3622, 2003. doi: 10.1002/anie.200300593.

37. K. J. C. van Bommel, A. Friggeri, and S. Shinkai, "Organic templates for the generation of inorganic materials," *Angewandte Chemie International Edition*, vol. 42, no. 9, pp. 980-999, 2003. doi: 10.1002/anie.200390284.
38. T. Valdés-Solís and A. B. Fuertes, "High-surface area inorganic compounds prepared by nanocasting techniques," *Materials Research Bulletin*, vol. 41, no. 12, pp. 2187-2197, 2006. doi: 10.1016/j.materresbull.2006.04.018.
39. A. A. Zakhidov, R. H. Baughman, Z. Iqbal, C. Cui, I. Khayrullin, S. O. Dantas, J. Marti, and V. G. Ralchenko, "Carbon structures with three-dimensional periodicity at optical wavelengths," *Science*, vol. 282, no. 5390, pp. 897-901, 1998. doi: 10.1126/science.282.5390.897.
40. J. J. Schneider and J. Engstler, "Carbon and polymer filaments in nanoporous alumina," *European Journal of Inorganic Chemistry*, vol. 2006, no. 9, pp. 1723-1736, 2006. doi: 10.1002/ejic.200501145.
41. X. Li, F. Cheng, B. Guo, and J. Chen, "Template-synthesized $LiCoO_2$, $LiMn_2O_4$, and $LiNi_{0.8}Co_{0.2}O_2$ nanotubes as the cathode materials of lithium ion batteries," *The Journal of Physical Chemistry B*, vol. 109, no. 29, pp. 14017-14024, 2005. doi: 10.1021/jp051900a.
42. J. S. Sakamoto and B. Dunn, "Hierarchical battery electrodes based on inverted opal structures," *Journal of Materials Chemistry*, vol. 12, no. 10, pp. 2859-2861, 2002. doi: 10.1039/b205634h.
43. C. M. Doherty, R. A. Caruso, B. M. Smarsly, and C. J. Drummond, "Colloidal crystal templating to produce hierarchically porous $LiFePO_4$ electrode materials for high power lithium ion batteries," *Chemistry of Materials*, vol. 21, no. 13, pp. 2895-2903, 2009. doi: 10.1021/cm900698p.
44. C. M. Doherty, R. A. Caruso, B. M. Smarsly, P. Adelhelm, and C. J. Drummond, "Hierarchically porous monolithic $LiFePO_4$/carbon composite electrode materials for high power lithium ion batteries," *Chemistry of Materials*, vol. 21, no. 21, pp. 5300-5306, 2009. doi: 10.1021/cm9024167.
45. J. Cabana, T. Valdés-Solís, M. R. Palacín, J. Oró-Solé, A. Fuertes, G. Marbán, and A. B. Fuertes, "Enhanced high rate performance of $LiMn_2O_4$ spinel nanoparticles synthesized by a hard-template route," *Journal of Power*

Sources, vol. 166, no. 2, pp. 492-498, 2007. doi: 10.1016/j.jpowsour.2006.12.107.

46. S. Lim, C. S. Yoon, and J. Cho, "Synthesis of nanowire and hollow $LiFePO_4$ cathodes for high-performance lithium batteries," *Chemistry of Materials*, vol. 20, no. 14, pp. 4560-4564, 2008. doi: 10.1021/cm8006364.
47. J.-y. Luo, Y.-g. Wang, H.-m. Xiong, and Y.-y. Xia, "Ordered mesoporous spinel $LiMn_2O_4$ by a soft-chemical process as a cathode material for lithium-ion batteries," *Chemistry of Materials*, vol. 19, no. 19, pp. 4791-4795, 2007. doi: 10.1021/cm0714180.
48. D. Jugović, M. Mitrić, M. Milović, B. Jokić, M. Vukomanović, D. Suvorov, and D. Uskoković, "Properties of quenched $LiFePO_4$/C powder obtained via cellulose matrix-assisted method," *Powder Technology*, vol. 246, no., pp. 539-544, 2013. doi: 10.1016/j.powtec.2013.06.021.
49. J. W. Fergus, "Recent developments in cathode materials for lithium ion batteries," *Journal of Power Sources*, vol. 195, no. 4, pp. 939-954, 2010. doi: 10.1016/j.jpowsour.2009.08.089.
50. K. Yang, Z. Deng, and J. Suo, "Effects of carbon sources and carbon contents on the electrochemical properties of $LiFePO_4$/C cathode material," *Journal of Solid State Electrochemistry*, vol. 16, no. 8, pp. 2805-2813, 2012. doi: 10.1007/s10008-012-1705-8.
51. B. L. Ellis, K. T. Lee, and L. F. Nazar, "Positive Electrode Materials for Li-Ion and Li-Batteries," *Chemistry of Materials*, vol. 22, no. 3, pp. 691-714, 2010. doi: 10.1021/cm902696j.
52. G. Kucinskis, G. Bajars, and J. Kleperis, "Graphene in lithium ion battery cathode materials: A review," *Journal of Power Sources*, vol. 240, no., pp. 66-79, 2013. doi: 10.1016/j.jpowsour.2013.03.160.
53. J. T. Kuo, H. K. Yang, and J. S. Chen, "A simple and inexpensive filtration method for the preparation of $LiFePO_4$/C powders," *Int. J. Electrochem. Sci.*, vol. 10, no., pp. 8058 - 8071, 2015.
54. D. L. Gin, W. Gu, B. A. Pindzola, and W.-J. Zhou, "Polymerized lyotropic liquid crystal assemblies for materials applications," *Accounts of Chemical Research*, vol. 34, no. 12, pp. 973-980, 2001. doi: 10.1021/ar000140d.

55. X. Gou, F. Cheng, Y. Shi, L. Zhang, S. Peng, J. Chen, and P. Shen, "Shape-controlled synthesis of ternary chalcogenide $ZnIn_2S_4$ and $CuIn(S,Se)_2$ nano-/microstructures via facile solution route," *Journal of the American Chemical Society*, vol. 128, no. 22, pp. 7222-7229, 2006. doi: 10.1021/ja0580845.
56. K. T. Nam, D.-W. Kim, P. J. Yoo, C.-Y. Chiang, N. Meethong, P. T. Hammond, Y.-M. Chiang, and A. M. Belcher, "Virus-enabled synthesis and assembly of nanowires for lithium ion battery electrodes," *Science*, vol. 312, no. 5775, pp. 885-888, 2006. doi: 10.1126/science.1122716.
57. Y. J. Lee and A. M. Belcher, "Nanostructure design of amorphous $FePO_4$ facilitated by a virus for 3 V lithium ion battery cathodes," *Journal of Materials Chemistry*, vol. 21, no. 4, pp. 1033-1039, 2011. doi: 10.1039/c0jm02544e.
58. C. X. Guo, Y. Q. Shen, Z. L. Dong, X. D. Chen, X. W. Lou, and C. M. Li, "DNA-directed growth of $FePO_4$ nanostructures on carbon nanotubes to achieve nearly 100% theoretical capacity for lithium-ion batteries," *Energy & Environmental Science*, vol. 5, no. 5, pp. 6919-6922, 2012. doi: 10.1039/c2ee21320f.
59. J. Ryu, S.-W. Kim, K. Kang, and C. B. Park, "Mineralization of self-assembled peptide nanofibers for rechargeable lithium ion batteries," *Advanced Materials*, vol. 22, no. 48, pp. 5537-5541, 2010. doi: 10.1002/adma.201000669.
60. A. L. Lehninger, D. L. Nelson, and M. M. Cox, *Lehninger principles of biochemistry*. W. H. Freeman, 2005
61. X. Zhao, F. Pan, H. Xu, M. Yaseen, H. Shan, C. A. E. Hauser, S. Zhang, and J. R. Lu, "Molecular self-assembly and applications of designer peptide amphiphiles," *Chemical Society Reviews*, vol. 39, no. 9, pp. 3480-3498, 2010. doi: 10.1039/b915923c.
62. I. W. Hamley, "Self-assembly of amphiphilic peptides," *Soft Matter*, vol. 7, no. 9, pp. 4122-4138, 2011. doi: 10.1039/c0sm01218a.
63. J. D. Hartgerink, E. R. Zubarev, and S. I. Stupp, "Supramolecular one-dimensional objects," *Current Opinion in Solid State and Materials Science*, vol. 5, no. 4, pp. 355-361, 2001. doi: 10.1016/S1359-0286(01)00019-5.

64. H. Cui, M. J. Webber, and S. I. Stupp, "Self-assembly of peptide amphiphiles: From molecules to nanostructures to biomaterials," *Peptide Science*, vol. 94, no. 1, pp. 1-18, 2010. doi: 10.1002/bip.21328.
65. J. D. Hartgerink, E. Beniash, and S. I. Stupp, "Self-assembly and mineralization of peptide-amphiphile nanofibers," *Science*, vol. 294, no. 5547, pp. 1684-1688, 2001. doi: 10.1126/science.1063187.
66. G. A. Silva, C. Czeisler, K. L. Niece, E. Beniash, D. A. Harrington, J. A. Kessler, and S. I. Stupp, "Selective differentiation of neural progenitor cells by high-epitope density nanofibers," *Science*, vol. 303, no. 5662, pp. 1352-1355, 2004. doi: 10.1126/science.1093783.
67. J. D. Hartgerink, E. Beniash, and S. I. Stupp, "Peptide-amphiphile nanofibers: A versatile scaffold for the preparation of self-assembling materials," *Proceedings of the National Academy of Sciences*, vol. 99, no. 8, pp. 5133-5138, 2002. doi: 10.1073/pnas.072699999.
68. E. Fischer and E. Fourneau, "Ueber einige derivate des glykocolls," *Berichte der deutschen chemischen Gesellschaft*, vol. 34, no. 2, pp. 2868-2877, 1901. doi: 10.1002/cber.190103402249.
69. R. B. Merrifield, "Solid phase peptide synthesis. I. The synthesis of a tetrapeptide," *Journal of the American Chemical Society*, vol. 85, no. 14, pp. 2149-2154, 1963. doi: 10.1021/ja00897a025.
70. X. Zhao, F. Pan, and J. R. Lu, "Recent development of peptide self-assembly," *Progress in Natural Science*, vol. 18, no. 6, pp. 653-660, 2008. doi: 10.1016/j.pnsc.2008.01.012.
71. A. Dehsorkhi, V. Castelletto, and I. W. Hamley, "Self-assembling amphiphilic peptides," *Journal of Peptide Science*, vol. 20, no. 7, pp. 453-467, 2014. doi: 10.1002/psc.2633.
72. B. Mammadov, R. Mammadov, M. O. Guler, and A. B. Tekinay, "Cooperative effect of heparan sulfate and laminin mimetic peptide nanofibers on the promotion of neurite outgrowth," *Acta Biomaterialia*, vol. 8, no. 6, pp. 2077-2086, 2012. doi: 10.1016/j.actbio.2012.02.006.
73. S. Ustun, A. Tombuloglu, M. Kilinc, M. O. Guler, and A. B. Tekinay, "Growth and differentiation of prechondrogenic cells on bioactive self-

assembled peptide nanofibers," *Biomacromolecules*, vol. 14, no. 1, pp. 17-26, 2013. doi: 10.1021/bm301538k.

74. M. Sardan, M. Kilinc, R. Genc, A. B. Tekinay, and M. O. Guler, "Cell penetrating peptide amphiphile integrated liposomal systems for enhanced delivery of anticancer drugs to tumor cells," *Faraday Discussions*, vol. 166, no. 0, pp. 269-283, 2013. doi: 10.1039/c3fd00058c.
75. S. Bulut, T. S. Erkal, S. Toksoz, A. B. Tekinay, T. Tekinay, and M. O. Guler, "Slow release and delivery of antisense oligonucleotide drug by self-assembled peptide amphiphile nanofibers," *Biomacromolecules*, vol. 12, no. 8, pp. 3007-3014, 2011. doi: 10.1021/bm200641e.
76. R. J. Lee, "Liposomal delivery as a mechanism to enhance synergism between anticancer drugs," *Molecular Cancer Therapeutics*, vol. 5, no. 7, pp. 1639-1640, 2006. doi: 10.1158/1535-7163.mct-06-c02.
77. K. J. Myers and N. M. Dean, "Sensible use of antisense: How to use oligonucleotides as research tools," *Trends in Pharmacological Sciences*, vol. 21, no. 1, pp. 19-23, 2000. doi: 10.1016/S0165-6147(99)01420-0.
78. S. Sulek, B. Mammadov, D. I. Mahcicek, H. Sozeri, E. Atalar, A. B. Tekinay, and M. O. Guler, "Peptide functionalized superparamagnetic iron oxide nanoparticles as MRI contrast agents," *Journal of Materials Chemistry*, vol. 21, no. 39, pp. 15157-15162, 2011. doi: 10.1039/c1jm11387a.
79. M. Sardan, A. Yildirim, D. Mumcuoglu, A. B. Tekinay, and M. O. Guler, "Noncovalent functionalization of mesoporous silica nanoparticles with amphiphilic peptides," *Journal of Materials Chemistry B*, vol. 2, no. 15, pp. 2168-2174, 2014. doi: 10.1039/c4tb00037d.
80. H. Acar, R. Garifullin, and M. O. Guler, "Self-assembled template-directed synthesis of one-dimensional silica and titania nanostructures," *Langmuir*, vol. 27, no. 3, pp. 1079-1084, 2011. doi: 10.1021/la104518g.
81. M. A. Khalily, O. Ustahuseyin, R. Garifullin, R. Genc, and M. O. Guler, "A supramolecular peptide nanofiber templated Pd nanocatalyst for efficient Suzuki coupling reactions under aqueous conditions," *Chemical Communications*, vol. 48, no. 92, pp. 11358-11360, 2012. doi: 10.1039/c2cc36228g.

82. M. Müllner, T. Lunkenbein, N. Miyajima, J. Breu, and A. H. E. Müller, "A facile polymer templating route toward high-aspect-ratio crystalline titania nanostructures," *Small*, vol. 8, no. 17, pp. 2636-2640, 2012. doi: 10.1002/smll.201200738.
83. H. Ceylan, C. Ozgit-Akgun, T. S. Erkal, I. Donmez, R. Garifullin, A. B. Tekinay, H. Usta, N. Biyikli, and M. O. Guler, "Size-controlled conformal nanofabrication of biotemplated three-dimensional TiO_2 and ZnO nanonetworks," *Sci. Rep.*, vol. 3, no., 2013. doi: 10.1038/srep02306
84. S. Scanlon, A. Aggeli, N. Boden, R. Koopmans, R. Brydson, and C. M. Rayner, "Peptide aerogels comprising self-assembling nanofibrils," *Micro & Nano Letters, IET*, vol. 2, no. 2, pp. 24-29, 2007. doi: 10.1049/mnl:20070006.
85. X.-D. Xu, C.-S. Chen, B. Lu, S.-X. Cheng, X.-Z. Zhang, and R.-X. Zhuo, "Coassembly of oppositely charged short peptides into well-defined supramolecular hydrogels," *The Journal of Physical Chemistry B*, vol. 114, no. 7, pp. 2365-2372, 2010. doi: 10.1021/jp9102417.
86. J. Kubelka and T. A. Keiderling, "Differentiation of β-sheet-forming structures: Ab initio-based simulations of IR absorption and vibrational CD for model peptide and protein β-sheets," *Journal of the American Chemical Society*, vol. 123, no. 48, pp. 12048-12058, 2001. doi: 10.1021/ja0116627.
87. H. Cui, T. Muraoka, A. G. Cheetham, and S. I. Stupp, "Self-Assembly of Giant Peptide Nanobelts," *Nano Letters*, vol. 9, no. 3, pp. 945-951, 2009. doi: 10.1021/nl802813f.
88. C. A. Batt and R. K. Robinson, *Encyclopedia of food microbiology*. Elsevier Science, 2014
89. V. Pralong, J. B. Leriche, B. Beaudoin, E. Naudin, M. Morcrette, and J. M. Tarascon, "Electrochemical study of nanometer Co_3O_4, Co, $CoSb_3$ and Sb thin films toward lithium," *Solid State Ionics*, vol. 166, no. 3–4, pp. 295-305, 2004. doi: 10.1016/j.ssi.2003.11.018.
90. K. Kang, Y. S. Meng, J. Bréger, C. P. Grey, and G. Ceder, "Electrodes with high power and high capacity for rechargeable lithium batteries," *Science*, vol. 311, no. 5763, pp. 977-980, 2006. doi: 10.1126/science.1122152.

91. S.-i. Nishimura, G. Kobayashi, K. Ohoyama, R. Kanno, M. Yashima, and A. Yamada, "Experimental visualization of lithium diffusion in Li_xFePO_4," *Nat Mater*, vol. 7, no. 9, pp. 707-711, 2008. 92.M. S. Islam, D. J. Driscoll, C. A. J. Fisher, and P. R. Slater, "Atomic-scale investigation of defects, dopants, and lithium transport in the $LiFePO_4$ olivine-type battery material," *Chemistry of Materials*, vol. 17, no. 20, pp. 5085-5092, 2005. doi: 10.1021/cm050999v.
93. S.-Y. Chung, S.-Y. Choi, T. Yamamoto, and Y. Ikuhara, "Atomic-scale visualization of antisite defects in $LiFePO_4$," *Physical Review Letters*, vol. 100, no. 12, pp. 125502, 2008.
94. S.-Y. Chung, S.-Y. Choi, T. Yamamoto, and Y. Ikuhara, "Orientation-dependent arrangement of antisite defects in lithium iron(II) phosphate crystals," *Angewandte Chemie International Edition*, vol. 48, no. 3, pp. 543-546, 2009. doi: 10.1002/anie.200803520.
95. B. Kang and G. Ceder, "Battery materials for ultrafast charging and discharging," *Nature*, vol. 458, no. 7235, pp. 190-193, 2009.
96. C. Delacourt, P. Poizot, J.-M. Tarascon, and C. Masquelier, "The existence of a temperature-driven solid solution in Li_xFePO_4 for $0 \leq x \leq 1$," *Nat Mater*, vol. 4, no. 3, pp. 254-260, 2005.
97. M. Yonemura, A. Yamada, Y. Takei, N. Sonoyama, and R. Kanno, "Comparative kinetic study of olivine Li_xMPO_4 (M = Fe, Mn)," *Journal of The Electrochemical Society*, vol. 151, no. 9, pp. A1352-A1356, 2004. doi: 10.1149/1.1773731.
98. C. M. Julien, A. Mauger, A. Ait-Salah, M. Massot, F. Gendron, and K. Zaghib, "Nanoscopic scale studies of $LiFePO_4$ as cathode material in lithium-ion batteries for HEV application," *Ionics*, vol. 13, no. 6, pp. 395-411, 2007. doi: 10.1007/s11581-007-0149-0.
99. L.-X. Yuan, Z.-H. Wang, W.-X. Zhang, X.-L. Hu, J.-T. Chen, Y.-H. Huang, and J. B. Goodenough, "Development and challenges of $LiFePO_4$ cathode material for lithium-ion batteries," *Energy & Environmental Science*, vol. 4, no. 2, pp. 269-284, 2011. doi: 10.1039/c0ee00029a.

100. Y. Wang, P. He, and H. Zhou, "Olivine $LiFePO_4$: Development and future," *Energy & Environmental Science*, vol. 4, no. 3, pp. 805-817, 2011. doi: 10.1039/c0ee00176g.
101. K. T. Lee and J. Cho, "Roles of nanosize in lithium reactive nanomaterials for lithium ion batteries," *Nano Today*, vol. 6, no. 1, pp. 28-41, 2011. doi: 10.1016/j.nantod.2010.11.002.
102. Y. Yin, Y. Hu, P. Wu, H. Zhang, and C. Cai, "A graphene-amorphous $FePO_4$ hollow nanosphere hybrid as a cathode material for lithium ion batteries," *Chemical Communications*, vol. 48, no. 15, pp. 2137-2139, 2012. doi: 10.1039/c2cc17381f.
103. Y. Yajing, Z. Hui, W. Ping, Z. Bo, and C. Chenxin, "Iron phosphate nanostructures synthesized by microwave method and their applications in biosensing," *Nanotechnology*, vol. 21, no. 42, pp. 425504, 2010.
104. H. A. Behanna, J. J. J. M. Donners, A. C. Gordon, and S. I. Stupp, "Coassembly of amphiphiles with opposite peptide polarities into nanofibers," *Journal of the American Chemical Society*, vol. 127, no. 4, pp. 1193-1200, 2005. doi: 10.1021/ja044863u.
105. K. L. Niece, J. D. Hartgerink, J. J. J. M. Donners, and S. I. Stupp, "Self-assembly combining two bioactive peptide-amphiphile molecules into nanofibers by electrostatic attraction," *Journal of the American Chemical Society*, vol. 125, no. 24, pp. 7146-7147, 2003. doi: 10.1021/ja028215r.
106. M. O. Guler, L. Hsu, S. Soukasene, D. A. Harrington, J. F. Hulvat, and S. I. Stupp, "Presentation of RGDS epitopes on self-assembled nanofibers of branched peptide amphiphiles," *Biomacromolecules*, vol. 7, no. 6, pp. 1855-1863, 2006. doi: 10.1021/bm060161g.
107. H. Jiang, M. O. Guler, and S. I. Stupp, "The internal structure of self-assembled peptide amphiphiles nanofibers," *Soft Matter*, vol. 3, no. 4, pp. 454-462, 2007. doi: 10.1039/b614426h.
108. A. A. Salah, P. Jozwiak, J. Garbarczyk, K. Benkhouja, K. Zaghib, F. Gendron, and C. M. Julien, "Local structure and redox energies of lithium phosphates with olivine- and Nasicon-like structures," *Journal of Power Sources*, vol. 140, no. 2, pp. 370-375, 2005. doi: 10.1016/j.jpowsour.2004.08.029.

109. C. M. Burba and R. Frech, "Raman and FTIR spectroscopic study of Li_xFePO_4 $(0 \leq x \leq 1)$" *Journal of The Electrochemical Society*, vol. 151, no. 7, pp. A1032-A1038, 2004. doi: 10.1149/1.1756885.
110. P. Jozwiak, J. Garbarczyk, F. Gendron, A. Mauger, and C. M. Julien, "Disorder in Li_xFePO_4: From glasses to nanocrystallites," *Journal of Non-Crystalline Solids*, vol. 354, no. 17, pp. 1915-1925, 2008. doi: 10.1016/j.jnoncrysol.2007.10.032.
111. M. Singh and M. Willert-Porada, "Polyol process for the synthesis of $LiFePO_4$ rhombohedral particles," *Advanced Powder Technology*, vol. 22, no. 2, pp. 284-289, 2011. doi: 10.1016/j.apt.2011.02.006.
112. X. Zhang, X. Zhang, W. He, Y. Yue, H. Liu, and J. Ma, "Biocarbon-coated $LiFePO_4$ nucleus nanoparticles enhancing electrochemical performances," *Chemical Communications*, vol. 48, no. 81, pp. 10093-10095, 2012. doi: 10.1039/c2cc34207c.
113. S. Xu, S. Zhang, J. Zhang, T. Tan, and Y. Liu, "A maize-like $FePO_4$@MCNT nanowire composite for sodium-ion batteries via a microemulsion technique," *Journal of Materials Chemistry A*, vol. 2, no. 20, pp. 7221-7228, 2014. doi: 10.1039/c4ta00239c.
114. M. Moradi, Z. Li, J. Qi, W. Xing, K. Xiang, Y.-M. Chiang, and A. M. Belcher, "Improving the capacity of sodium ion battery using a virus-templated nanostructured composite cathode," *Nano Letters*, vol. 15, no. 5, pp. 2917-2921, 2015. doi: 10.1021/nl504676v.
115. A. M. Beale and G. Sankar, "Following the structural changes in iron phosphate catalysts by in situ combined XRD/QuEXAFS technique," *Journal of Materials Chemistry*, vol. 12, no. 10, pp. 3064-3072, 2002. doi: 10.1039/b204059j.
116. X. Sun, K. Sun, Y. Wang, X. Bai, C. Chen, and B. Cui, "Scale-up synthesis, structure characterization and electrochemical characteristics of C-$LiFePO_4$ nanocomposites for lithium ion rechargeable batteries," *International Journal of Electrochemical Science*, vol. 8, no. 12, pp. 12816-12836, 2013.
117. X. Wang, Y. Wang, Q. Tang, Q. Guo, Q. Zhang, and H. Wan, "MCM-41-supported iron phosphate catalyst for partial oxidation of methane to

oxygenates with oxygen and nitrous oxide," *Journal of Catalysis*, vol. 217, no. 2, pp. 457-467, 2003. doi: 10.1016/S0021-9517(03)00077-0.

118. X. T. Wu and R. G. Cavell, Controlled assembly and modification of inorganic systems. Springer, 2009
119. T. R. I. Cataldi, G. E. De Benedetto, and A. Bianchini, "X-ray photoelectron spectroscopic investigation and electrochemistry of polynuclear indium (III) hexacyanoferrate films," *Journal of Electroanalytical Chemistry*, vol. 448, no. 1, pp. 111-117, 1998. doi: 10.1016/S0022-0728(98)00030-8.
120. G. Polzonetti, C. Battocchio, M. Dettin, R. Gambaretto, C. Di Bello, V. Carravetta, S. Monti, and G. Iucci, "Self-assembling peptides: A combined XPS and NEXAFS investigation on the structure of two dipeptides Ala–Glu, Ala–Lys," *Materials Science and Engineering: C*, vol. 28, no. 2, pp. 309-315, 2008. doi: 10.1016/j.msec.2007.02.004.
121. N. N. Sinha, C. Shivakumara, and N. Munichandraiah, "High rate capability of a dual-porosity $LiFePO_4$/C composite," *ACS Applied Materials & Interfaces*, vol. 2, no. 7, pp. 2031-2038, 2010. doi: 10.1021/am100309w.
122. J. Zhang, L. Zhuo, L. Zhang, C. Wu, X. Zhang, and L. Wang, "Synthesis and electrochemical properties of $LiFePO_4$/C composite cathode material prepared by a new route using supercritical carbon dioxide as a solvent," *Journal of Materials Chemistry*, vol. 21, no. 19, pp. 6975-6980, 2011. doi: 10.1039/c1jm10168d.
123. M. Doeff, J. Wilcox, R. Yu, A. Aumentado, M. Marcinek, and R. Kostecki, "Impact of carbon structure and morphology on the electrochemical performance of LiFePO4/C composites," *Journal of Solid State Electrochemistry*, vol. 12, no. 7-8, pp. 995-1001, 2008. doi: 10.1007/s10008-007-0419-9.
124. M. Law, J. Goldberger, and P. Yang, "Semiconductor nanowires and nanotubes," *Annual Review of Materials Research*, vol. 34, no. 1, pp. 83-122, 2004. doi: doi:10.1146/annurev.matsci.34.040203.112300.
125. A. P. Alivisatos, "Semiconductor clusters, nanocrystals, and quantum dots," *Science*, vol. 271, no. 5251, pp. 933-937, 1996.

126. B. Weng, S. Liu, Z.-R. Tang, and Y.-J. Xu, "One-dimensional nanostructure based materials for versatile photocatalytic applications," *RSC Advances*, vol. 4, no. 25, pp. 12685-12700, 2014. doi: 10.1039/c3ra47910b.
127. Y. Fang, L. Xiao, J. Qian, X. Ai, H. Yang, and Y. Cao, "Mesoporous Amorphous FePO4 Nanospheres as High-Performance Cathode Material for Sodium-Ion Batteries," *Nano Letters*, vol. 14, no. 6, pp. 3539-3543, 2014. doi: 10.1021/nl501152f.

APPENDIX 1 Copyright Clearance Agreements

Reference Number	License Supplier	License Number
2	Nature Publishing Group	3697201271504
4	American Chemical Society	-
8	The Royal Society of Chemistry	3696981153575
21	Elsevier	3730670157387
61	John Wiley and Sons	3696990681776

All license agreements between Hepi Hari Susapto and the License Suppliers are made by means of Copyright Clearance Center (CCC).

APPENDIX 2 EDX Quantification

a) Calcined E-PA/$FePO_4$

Element	Wt%	At%
C K	6.16	11.51
O K	44.78	62.78
P K	18.65	13.50
Fe K	30.40	12.21
Total	100.00	100.00

b) Calcined Phos-PA/$FePO_4$

Element	Wt%	At%
C K	9.94	18.14
O K	41.47	57.52
P K	17.30	12.25
Fe K	30.79	12.09
Total	100.00	100.00

APPENDIX 3 ICP-MS

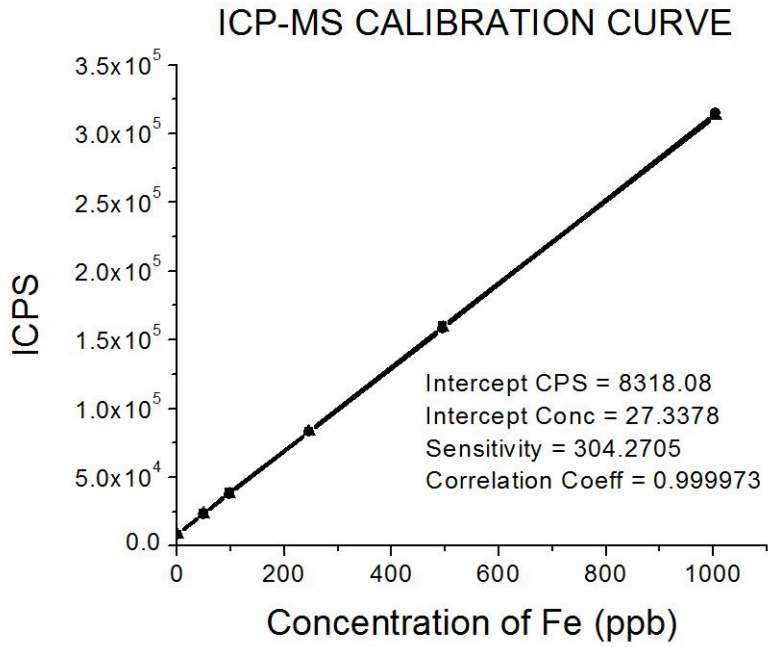

a) Calcined E-PA/$FePO_4$

1.1 mg of calcined E-PA/$FePO_4$ powder was dissolved in 1.1 mL of concentrated HCl and then diluted by adding 2% (v/v) HNO_3 until the volume reached 11 mL. 0.25 mL of this stock solution was taken and diluted in 50 mL of 2% HNO_3. The solution was then read using ICP-MS to determine the amount of iron in the solution. The result shows that the solution contains of 149.2 ppb of iron. In other words, there is 149.2 µg of iron in 1 L of the solution.

$$149.2\ \mu g/L \times 50\ mL = M \times 0.25\ mL$$

$$M = 29840\ \mu g/L = 29.84\ mg/L$$

Using the calculation steps above, the concentration of iron in the stock solution (M) is found to be 29.84 mg in 1 L of stock solution. Since the volume of stock solution and the weight of powder sample in the stock solution are 11 mL and 1.1 mg, respectively, the weight of iron in 1 mg can be found as 0.2984 mg. Finally, the percentage of $FePO_4$ amount in 1 mg of calcined E-PA/$FePO_4$ can be calculated as below:

$$\%\ FePO_4 = \frac{Mw_{FePO_4}}{Mw_{Fe}} \times 0.2984\ mg \times 100\% = 80.65\%$$

b) Calcined Phos-PA/$FePO_4$

Stock solution: 1.2 mg was dissolved in 1.2 mL of HCl and then completely diluted using 2% HNO_3 until the total volume was 12 mL.

Diluted solution: 0.25 mL of stock solution was diluted in 2% HNO_3 to 50 mL.

ICP-MS result: 124.8 ppb = 124.8 µg of iron in 1 L of diluted solution.

Iron content in stock solution:

$$124.8\ \mu g/L \times 50\ mL = M \times 0.25\ mL$$

$$M = 24960\ \mu g/L = 24.96\ mg/L$$

Iron content in 1 mg of sample:

$$\text{Fe weight} = 24.96\ mg/L \times \frac{12\ mL}{1.2\ mg} = 0.2496\ mg \text{ in 1 mg of sample}$$

% $FePO_4$ in 1 mg of sample:

$$\%\ FePO_4 = \frac{Mw_{FePO_4}}{Mw_{Fe}} \times 0.2496\ mg \times 100\% = 67.46\%$$

c) **Template-free $FePO_4$**

Stock solution: 1.5 mg was dissolved in 1.5 mL of HCl and then completely diluted using 2% HNO_3 until the total volume was 15 mL.

Diluted solution: 0.15 mL of stock solution was diluted with 2% HNO_3 to 50 mL.

ICP-MS result: 79.41 ppb = 79.41 µg of iron in 1 L of diluted solution.

Iron content in stock solution:

$$79.41\ \mu g/L \times 50\ mL = M \times 0.15\ mL$$

$$M = 26470\ \mu g/L = 26.47\ mg/L$$

Iron content in 1 mg of sample:

$$\text{Fe weight} = 26.47\ mg/L \times \frac{15\ mL}{1.5\ mg} = 0.2647\ mg \text{ in 1 mg of sample}$$

% $FePO_4$ in 1 mg of sample:

$$\%\ FePO_4 = \frac{Mw_{FePO_4}}{Mw_{Fe}} \times 0.2647\ mg \times 100\% = 71.54\%$$